Forcing and Responses of the Surface Energy Budget at Summit, Greenland

by

Nathaniel B. Miller

B.S., University of Colorado, 2001

M.S., University of Wisconsin, 2012

A thesis submitted to the

Faculty of the Graduate School of the

University of Colorado in partial fulfillment

of the requirements for the degree of

Doctor of Philosophy

Department of Atmospheric and Oceanic Sciences

2017

This thesis entitled:
Forcing and Responses of the Surface Energy Budget at Summit, Greenland
written by Nathaniel B. Miller
has been approved for the Department of Atmospheric and Oceanic Sciences

Dr. Matthew Shupe

Prof. John Cassano

Prof. Jennifer Kay

Dr. William Neff

Dr. Gijs de Boer

Date

The final copy of this thesis has been examined by the signatories, and we find that both the content and the form meet acceptable presentation standards of scholarly work in the above mentioned discipline.

Miller, Nathaniel B. (Ph.D., Atmospheric and Oceanic Sciences)

Forcing and Responses of the Surface Energy Budget at Summit, Greenland

Thesis directed by Dr. Matthew Shupe

Energy exchange at the Greenland Ice Sheet surface governs surface temperature variability, a factor critical for representing increasing surface melt extent, which portends a rise in global sea level. A comprehensive set of cloud, tropospheric, near-surface and sub-surface measurements at Summit Station is utilized to determine the driving forces and subsequent responses of the surface energy budget (SEB). This budget includes radiative, turbulent, and ground heat fluxes, and ultimately controls the evolution of surface temperature.

At Summit Station, clouds radiatively warm the surface in all months with an annual average cloud radiative forcing value of 33 $W\,m^{-2}$, largely driven by the occurrence of liquid-bearing clouds. The magnitude of the surface temperature response is dependent on how turbulent and ground heat fluxes modulate changes to radiative forcing. Relationships between forcing terms and responding surface fluxes show that changes in the upwelling longwave radiation compensate for 65–85% (50–60%) of the total change in radiative forcing in the winter (summer). The ground heat flux is the second largest response term (16% annually), especially during winter. Throughout the annual cycle, the sensible heat flux response is comparatively constant (9%) and latent heat flux response is only 1.5%, becoming more of a factor in modulating surface temperature responses during the summer. Combining annual cycles of these responses with cloud radiative forcing results, clouds warm the surface by an estimated 7.8°C annually.

A reanalysis product (ERA-I), operational model (CFSv2), and climate model (CESM) are evaluated utilizing the comprehensive set of SEB observations and process-based relationships. Annually, surface temperatures in each model are warmer than observed with overall poor representation of the coldest surface temperatures. Process-based relationships between different SEB flux terms offer insight into how well a modeling framework represents physical processes and the

ability to distinguish errors in forcing versus those in physical representation. Such relationships convey that all three models underestimate the response of surface temperatures to changes in radiative forcing. These results provide a method to expose model deficiencies and indicate the importance of representing surface, sub-surface and boundary-layer processes when portraying cloud impacts on surface temperature variability.

Dedication

To my amazing wife, Cathy, and our two wonderful, curious, and crazy children; Eleanor Summit and Henry Tate. May you grow in harmony with a changing world.

Acknowledgements

Thanks to the ICECAPS team who has guided me throughout my development of scientific independence; David Turner brought me into the scientific community by leveraging my engineering background to be an effective science technician at Summit Station, Von Walden literally introduced me to the Greenland Ice Sheet, Ralf Bennartz nourished my academic thirst for knowledge at the University of Wisconsin, and Matthew Shupe provided examples of excellence in research, always had time for science discussions, and allowed the right amount of independence to find my voice. Thanks to Christopher Cox for many valuable science discussions. Thanks to Claire Pettersen, who strives to unite and advance ICECAPS science with good-natured vigor. I appreciate Lance Roth for showing me how to live life on thick ice. Thanks to the ATOC professors at the University of Colorado for deepening my understanding of our physical world, especially Jennifer Kay who welcomed me into her group meetings and opened the door to the CESM modeling community. Thanks to David Noone, Konrad Steffen, and NOAA/GMD for providing quality measurements in a harsh environment. Thanks to Jan Lenaertz, Gijs de Boer, and Cathy Smith for providing model output. This research is supported by the National Science Foundation under grants PLR1303879, 1314156, and 1023574.

The support of my family has been a big reason why I was able to return to and succeed in academia. Thanks to my parents, Sally and Richard, who have always supported me and have helped me remain productive while pursuing my degree. My gratitude cannot be overstated for my wife, Cathy, who provides encouragement and support with a balance of honesty, loyalty, and love.

Contents

Chapter

Tables

Table

Figures

Figure

Chapter 1

Introduction

1.1 Greenland Ice Sheet

Consequential to the future of the Earth's hydrological processes and indicative of past climates, the Greenland Ice Sheet (GIS) is a predominant geological feature in the Northern Hemisphere. The GIS currently affects atmospheric and oceanic circulation patterns while serving as a massive reservoir of ice due to millennia of accumulation. It is estimated that the entire GIS contains enough liquid water equivalent to produce a sea level rise of 7.2 m with moderate to severe societal implications for coastal populations (IPCC, 2013; Hauer et al., 2016). Increases of melt water discharge will not only contribute to global sea level rise (Rignot et al., 2011) but could weaken the Atlantic meridional overturning circulation (Rahmstorf et al., 2015), which is a large uncertainty in future climate scenarios. Early 21st century attempts to model the fate of the GIS estimate that if the annual surface temperature increases by more than 3°C the majority of the GIS could melt within 1000 years (Gregory et al., 2004). Thus, it is imperative to understand atmospheric/ice sheet interactions that impact GIS surface temperatures, surface energy, and its resultant mass balance.

Over long-time scales the GIS mass balance responds to global changes in climate, which are driven by the variations of the intensity and distribution of solar radiation. Milankovitch cycles exist due to the eccentricity of earth's orbit (100 kyr), and changes to the axis tilt angle (41 kyr) and procession (23 kyr) (Serreze and Barry, 2014). During the late 20th century, Greenland Ice Sheet Project Two (GISP2) collected ice cores from Summit Station, which have been integral for

reconstructing climate information from tens to hundreds of thousand years ago via isotopic analysis of the slowly building ice. The location and elevation of Summit station (72.6 °N, 38.5 °W, 3211 m) was chosen to maximize the depth of the ice core record. These paleoclimate records, preserved by the GIS, indicate that regional temperature fluctuations throughout the Holocene are relatively stable compared to larger changes in the past, including previous dramatic climate shifts possibly occurring within just a few decades (Dansgaard et al., 1993). Generally, global cooling periods take much longer than relatively abrupt warming periods, yet in both cases surface temperature fluctuations are correlated with CO_2 content in the atmosphere (Alley, 2000).

Anthropogenic activities have lead to an increase in the concentration of CO_2 in the atmosphere, which impacts temperatures globally (Hansen et al., 1981) by increasing the atmospheric opacity to longwave radiation. Hanna et al. (2008) found a positive correlation in near-surface temperature trends between northern hemisphere and coastal stations in the GIS ablation zone since 1990, linking northern hemispheric warming trends to increases in surface melt. McGrath et al. (2013) reports a 0.09 °C yr^{-1} annual mean increase in near-surface temperature at Summit station from 1982–2011. Recent increases of central Greenland near-surface air temperature are related to a negative North Atlantic Oscillation (NAO) index and the associated high pressure anomalies to the southeast of Greenland, which favors northward transport of relatively warm air along the west cost and across central Greenland (Fettweis et al., 2013b). Although it is not clear if the more frequent, so-called blocking events (Overland et al., 2012) are the result of natural variability or anthropogenically forced (Francis and Vavrus, 2012), there is evidence that reductions of summer sea ice increases the occurrence of the positive geopotential height anomalies that enhance warm air advection over Greenland (Liu et al., 2016).

In July 2012, the atmospheric circulation pattern, favorable for southerly air advection (Hanna et al., 2014), delivered extremely warm, moist air via a phenomenon known as an atmospheric river, originating from anomalously warm temperatures in the United States (Neff et al., 2014). This produced an extremely extensive summertime melt event (Nghiem et al., 2012). This event concurs with an upward trend in the area of surface melt extent in recent decades (Mernild

et al., 2011). To exacerbate the situation, surface-melt also increases the GIS mass loss due to the acceleration of ice discharge from enhanced glacial sliding (Zwally et al., 2002). van den Broeke et al. (2009) estimate that from 2000-2008, half of GIS ice loss was due to net mass loss at the surface and the other half was due to ice discharge (total $\approx$167 $Gt\,yr^{-1}$). Due to advection of warm air masses over the ice sheet in the early 2010s (Fettweis et al., 2013b) the proportion of ice loss due to surface melt increased (Enderlin et al., 2014) resulting in an average mass loss of 269 $Gt\,yr^{-1}$ from 2011–2014 (McMillan et al., 2016).

Atmospheric circulation change is just one mechanism associated with Arctic amplification, which is the phenomenon of larger increases and variability of Arctic surface temperature compared to global temperatures. Positive feedbacks in the Arctic also include the effects of changes to surface albedo, sea-ice extent, ocean heat transport, cloud cover and water vapor (Holland and Bitz, 2003; Serreze and Barry, 2011). For example, more prevalent spring melt ponds on sea ice decrease albedo, enhancing the surface-melt of sea-ice, thus, leading to a decline of sea-ice extent (Schröder et al., 2014). The GIS ablation zone is subject to enhanced surface melting by similar surface albedo feedbacks (Box et al., 2012), including more absorption of insolation due to snow contaminants originating from earlier snow melt occurrence over land (Dumont et al., 2014).

In addition to surface albedo, cloud occurrence and phase modulate the amount of net radiative flux at the surface. In the past, observational evidence of the role of Arctic clouds in affecting surface temperatures has been difficult to characterize (Serreze et al., 2000) but advances in ground-based observations of cloud macrophysical and microphysical properties have elevated our foundational understanding of their radiative properties (Shupe et al., 2008; Turner et al., 2007b). Clouds act to increase the amount of downwelling thermal emission and decrease the amount of shortwave radiation, hence clouds act to warm the surface throughout winter. The presence of liquid water increases the cloud's optical depth (Curry and Herman, 1985), such that liquid-bearing clouds are more impactful on the radiative balance at the surface than ice-only clouds (Shupe and Intrieri, 2004). Across the Arctic the net effect of clouds on the surface radiation budget, which also includes the upwelling components, is dependent on surface albedo because this surface

property changes the amount of clear-sky net shortwave radiation that can be reduced by cloud presence. Thus, averaged over the Arctic Ocean the cooling effects of clouds in the summer (Kay and L'Ecuyer, 2013) is greater than that over sea ice containing seasonal melt ponds (Shupe and Intrieri, 2004) or snow-free land (Dong et al., 2010). The dry-snow zone in central Greenland, with its high year-round surface albedo, suggests that variations in optical properties of over-lying clouds are more impactful than changes in surface properties in determining the radiative balance at the surface. Heretofore there has not been a comprehensive set of atmospheric, near-surface and subsurface observations necessary to fully characterize and quantify the impact of clouds on the GIS surface radiation budget, the net response of the surface energy budget to this forcing, and the resultant temperature variability.

1.2 Motivational Background

In order to confidently model current, past and future GIS surface temperatures and the associated implications, detailed observations are necessary for understanding the physical processes occurring at the atmospheric/ice sheet interface. Various field campaigns have been conducted in the GIS ablation zone to investigate processes that determine the amount of surface melt (van de Wal et al., 2005; van den Broeke et al., 2008, 2011; Charalampidis et al., 2015). In contrast, the dry snow zone, which represents an area with positive mass balance, historically has had fewer observations making it an under-sampled area compared to coastal locations. Predicated upon infrastructure established by GISP2, Summit Station, a year-round operation, affords the opportunity to reliably record observations in environmentally harsh conditions. Shuman et al. (2001) compiled a record of direct near-surface (2 m) temperature measurements, spanning 1987–1999, reporting an average annual temperature of -29.4°C and bounds of daily maximum and minimum values ranging from -61°C in winter to -3°C in summer. These measurements, and those extended to the present, have become a part of a climatological record useful for discerning systematic changes and validating tools that have a much greater spatial representation (Shuman et al., 2014).

Synergy between ground-based observations at Summit Station and space-borne instruments enhance our understanding of surface temperatures and clouds above the GIS. While estimates of cloud influence on surface temperature trends have been attempted (Liu et al., 2008), it is unclear how GIS cloud retrieval biases affect the results. Downward-facing remote sensors at the top of the atmosphere are subject to signal attenuation and ground contamination, especially over highly reflective surfaces (Stubenrauch et al., 2013), potentially limiting detection of low-level clouds. Thus, upward-oriented ground-based measurements, which observe low background signal originating from space and maintain high sensitivity in the boundary-layer and lower troposphere are invaluable for evaluating satellite products with much greater spatial coverage (Liu et al., 2017).

Reanalysis products are also a useful tool for representing surface temperatures and cloud properties across the entirety of Greenland. Often used as truth to evaluate model performance or validate satellite retrievals, the validity of a reanalysis depends heavily on a proper blending of modeled parameters and observations. In central Greenland, long-term observations are sparse, thus ingested ground-based observations are heavily weighted toward coastal sites that may or may not be representative of the surface processes happening in the interior. In fact, Zhang et al. (2011) report seasonal discrepancies in European Reanalysis Interim's (ERA-I) near-surface temperature structure when compared to coastal radiosonde profiles, which does not bode well for ERA-I's ability to represent the boundary-layer structure in central Greenland. Observing the atmospheric temperature profile at Summit Station is not only useful for evaluation purposes but is a foundational necessity to investigate the atmospheric processes that determine surface temperature variability.

Surface-based inversions (SBI) are a well known phenomenon above ice-covered surfaces (Hudson and Brandt, 2005), observed as early as nearly a century ago (Sverdrup, 1926), and are characterized by increasing temperatures with altitude up to the top of the inversion layer. SBIs occur year-round over the GIS because in the dry-snow zone, the surface is highly reflective to shortwave radiation and is an efficient emitter of longwave radiation. In dry conditions, radiative cooling at the surface also cools elevated layers of the atmosphere, resulting in deep inversions (Bradley and

Keimig, 1992). SBIs can effectively decouple the surface from the overlying free troposphere by limiting turbulent mixing, consequently preventing the exchange of heat, water vapor (Berkelhammer et al., 2016) and other various chemical constituents (Cohen et al., 2007; Helmig et al., 2009). Thus, understanding environmental factors that influence the boundary-layer structure is critical to exposing the main drivers of turbulent heat exchange between the GIS and the atmosphere.

SBI occurrence and influences at Summit Station are characterized in detail by Miller et al. (2013), concluding:

> Surface-based inversions are a dominant feature above the Greenland ice sheet, creating a stable layer that limits vertical mixing and decouples the atmosphere from the surface. SBI presence and intensity are examined using complementary perspectives from MWR [microwave radiometer], radiosonde, and a meteorological tower. Nearly 72% of MWR profiles show surface-based inversions compared to 64% of radiosonde profiles and 80% as observed by meteorological tower data. Wintertime SBIs are very frequent and strong (intensity 20°C at times) because of the cold and dry atmosphere with relatively few clouds, which allows for strong radiative cooling at the surface. The transition from winter to summer sees a decrease in SBI occurrence and intensity as the surface is presumably warmed by enhanced insolation and the presence of more clouds, particularly those that are composed of liquid water. Investigation of the diurnal cycle supports the idea that these two factors play a role in the weakening of surface-based inversions. The influence of the clouds in July and August offsets the minimum SBI occurrence from the months with maximum insolation and possibly serves to dampen the diurnal cycle in September.

Bennartz et al. (2013) developed a surface energy balance model to represent how liquid-bearing clouds reduce the intensity or completely eliminate temperature inversions by radiatively warming the surface. In fact, the aforementioned July 2012 extreme melt event, which encompassed 98% of the GIS (Nghiem et al., 2012) would not have been as extensive without the presence of optically thin clouds, indicating how clouds can enhance the impact of warm air advection. Interestingly, optically thin (liquid water path from 10–40 $g\,m^{-2}$) liquid-bearing clouds were found to have the greatest warming effect in the presence of insolation. These clouds acted as an efficient emitter of longwave radiation and had an effective albedo less than that of the surface, thus increasing radiation at the surface compared to an equivalent clear-sky scene and allowing surface temperatures to surpass temperatures aloft.

The radiation budget is one component of the total surface energy budget (SEB), which also includes sensible, latent, and ground heat fluxes. Modeling studies are able to investigate process–based relationships between the various SEB terms and the stable boundary layer (Sterk et al., 2013) and the associated cloud–surface interactions (Morrison and Pinto, 2006). A detailed modeling perspective of the extensive July 2012 GIS melt event shows that turbulent and ground heat fluxes are significant modulators of changes to downwelling radiative fluxes and under the appropriate circumstances determine if the melting point of snow is achieved (Solomon et al., 2017). In order to have credibility, modeling studies (and more generally global climate models) must be based upon observed physical processes and compare well to observations, if available.

Inherently, models account for all surface energy flux, thus it is advantageous to have observationally based estimates of all SEB terms in conjunction with the atmospheric state and cloud properties to determine the cause of surface temperature variability and potiential surface temperature biases. The Surface Heat Budget of the Arctic Ocean (SHEBA) experiment (Uttal et al., 2002), from October 1997 to October 1998 in the Beaufort and Chukchi Seas, has enhanced our understanding of complex processes over sea ice, including cloud-surface interactions (Intrieri et al., 2002; Shupe and Intrieri, 2004), near-surface stability considerations (Persson et al., 2002; Grachev et al., 2005), and comprehensive SEB characterization (Persson et al., 2002; Persson, 2012). Many of the fundamental tools developed from this seminal Arctic field campaign can be applied to the snow covered surface of the central GIS. At Summit Station all components of the SEB have been reported for summer campaigns (Cullen and Steffen, 2001; Kuipers Munneke et al., 2009), but only during June 2000 to June 2002 has the full annual cycle been reported (Cullen, 2003; Hoch, 2005; Cullen et al., 2014). Combined with advances in cloud detection, techniques used in previous SEB studies are extremely useful in furthering our understanding of the processes that drive local variability of surface temperature. Currently, a coincidence of field campaigns at Summit Station have made it possible to investigate key atmospheric drivers and responses of the SEB.

1.3 A Collaboration of Observations

Summit Station (72.6 °N, 38.5 °W) is a unique location, situated in the accumulation zone of the GIS at an altitude of 3211 m and approximately 360 km from the nearest coast resulting in extremely dry, cold conditions, and an annual surface height increase of 0.63 $m\,yr^{-1}$ (Steffen and Box, 2001). Year-round instrument maintenance by science technicians provide the attention necessary to combat issues of instrument riming and failure. The homogeneous nature of the snow surface reduces sampling error from combining measurements from different station locations and increases the representative footprint of the observations. The breadth of available measurements for the years 2011–2014 is rare for any Arctic location, although other sites such as Barrow, Alaska (Stamnes et al., 1999) and Eureka, Canada record similar atmospheric properties. During the time period spanning July 2013 – June 2014, a number of on-going measurements overlapped with the occurrence of intensive field campaigns, providing redundancy of key observations, thus reducing data gaps and providing opportunities for comparison and cross-calibration.

A National Science Foundation funded field campaign entitled "An Integrated Characterization of Energy, Clouds, Atmospheric state, and Precipitation at Summit" (ICECAPS), in operation since May 2010 to the present, is designed to provide comprehensive observations of atmospheric, cloud and precipitation properties throughout the annual cycle. The project is a collaboration between the University of Colorado, University of Wisconsin, Washington State University, Vanderbilt University, and University of Oklahoma. The retrieved properties of the ICECAPS instrumentation are integrated to provide cross calibration and redundancy in case of individual instrument issues. A detailed overview of the project and all the instruments is given by Shupe et al. (2013b), and information pertinent to this thesis is discussed here (Table 1.1). Instruments are housed inside or on the roof of the Mobile Science Facility (MSF). The MSF is moved once a year to prevent the accumulation and heavy drifting of snow to engulf the enclosure. Data is transferred daily to the National Oceanic and Atmospheric Administration's (NOAA) Earth System Research Laboratory

in Boulder, Colorado and then quickly processed, displayed[1] , and made publicly available[2] .

Table 1.1: ICECAPS instrumentation used in this thesis.

Instrument	Direct or Indirect Measurement	Retrieved properties
MMCR	Cloud radar reflectivity at 35 GHz	Cloud vertical extent and occurence
MWRs	Spectral microwave radiances from 22–150 GHz	LWP, PWV, Temperature profile
Ceilometer	Attenuated backscatter	Cloud base height and occurrence
MPL	Attenuated backscatter	Cloud occurence
Radiosonde	Profiles of temperature and relative humidity	

Temperature and humidity profiles throughout the troposphere are recorded using twice daily Vaisala RS92 radiosondes (Miloshevich et al., 2009). In addition, more frequent (approximately every 40 minutes) temperature profiles in the lowest 1-2 km above ground level are retrieved from a Radiometer Physics GmbH (RPG) HATPRO microwave radiometer (MWR; Rose et al., 2005) using 8 different zenith angles and 6 V-band channels (Miller et al., 2013). The MWR V-band (52.3, 53.9, 54.9, 56.7, 57.3, and 58.0 GHz) brightness temperatures are calibrated with an internal calibration target every 3.5 minutes and twice a year using an external absolute calibration target filled with liquid nitrogen. Additioinal brightness temperatures in the K-band and higher frequencies (23.8, 31.4, 90.0 and 150.0 GHz) are calibrated using an automated tip curve technique (Han and Westwater, 2000). The MWR scanning strategy and details of the calibration of the brightness temperatures are detailed by Miller (2012). Moisture content, including liquid water path (LWP) and precipitable water vapor (PWV), are retrieved via an optical estimation technique (MWR-RET, Turner et al., 2007a). Use of the higher frequencies (90 and 150 GHz) enhances sensitivity to baseline water vapor (Crewell and Löhnert, 2003), effectively reducing retrieval uncertainty (LWP $\approx 5\ g\,m^{-2}$, PWV ≈ 3 mm) and allowing for the detection of optically thin liquid-bearing clouds.

Cloud macrophysics, including occurrence and vertical location, are measured by a millimeter

[1] https://www.esrl.noaa.gov/psd/arctic/observatories/summit/browser/
[2] ftp://ftp1.esrl.noaa.gov/psd3/arctic/summit/ and Arctic Data Center

cloud radar (MMCR; Moran et al., 1998), micro-pulse lidar (MPL; Campbell et al., 2002) and ceilometer. The Vaisala ceilometer is used to detect cloud occurrence and cloud base height within the lowest 7-8 km and may be unable to detect clouds composed of predominantly ice. The MPL has enhanced sensitivity to ice particles but can be attenuated by optically thick liquid-bearing clouds and prevent observations at higher elevations. The MMCR operates at a frequency of 35 GHz and is ideal for detecting Arctic clouds, with low signal attenuation and high vertical resolution ($\approx$ 0.05 km). A reflectivity threshold of -60 dBz is used for detecting cloud presence and vertical extent, although the radar is blind to the first $\approx$150 m above the surface. Combining these sensors to detect cloud presence, as was done at Summit Station by Shupe et al. (2013b), provides the best-estimate cloud detection product (Shupe et al., 2011) and is less susceptible to data gaps due to individual instrument downtime.

Combining atmospheric state information, cloud property information and radiation measurements at the surface facilitates an enhanced understanding of the impact of various types of clouds on the radiation balance. The Swiss Federal Institute of Technology (ETH) Zürich maintains broadband radiative flux measurements at Summit and data access was granted for the years spanning 2011–2014. Thermal emission from the surface and the overlying atmosphere is measured by a pair of pyrgeometers and the upwelling and downwelling solar irradiance by a pair of pyranometers. NOAA's Global Monitoring Division (NOAA/GMD) installed a similar suite of instruments in August 2013 such that co-located measurements are used for cross-calibration.

Near-surface meteorological measurements of temperature, humidity, pressure and windspeed are necessary to estimate turbulent heat exchange at the surface. NOAA/GMD provides reliable 1-minute resolution meteorological data at 10 m and 2 m above the surface and is located about 1 km northeast of the MSF. Within 100 m of the MSF was a University of Colorado experiment called Closing the Isotope Balance at Summit (CIBS), which included redundant meteorological measurements to NOAA/GMD at 10 m and 2 m. CIBS also included sonic anemometers (at 10 and 2 m) to measure high speed fluctuations in temperature and wind speed, useful for evaluating turbulent surface energy exchange processes. Hence, many meteorological variables have multiple

estimates at 10 and 2 m above the surface utilized for redundancy in the case of instrument downtime and uncertainty estimation. In addition, CIBS measured snow temperatures within 2 m of the surface using Campbell Scientific temperature probes, which are used to estimate the ground heat flux from 1 July 2013 – 30 June 2014. Table 1.1 and Table 3.2 contain a full list of instrumentation and measured parameters used in this thesis.

1.4 Research Goals

The primary goal of this thesis is to characterize the influence of clouds on surface temperature variability at Summit Station. Observational data is utilized to investigate how clouds affect the balance of surface energy fluxes at the ice sheet-atmosphere interface, providing a process-based perspective useful for model evaluation. The main objectives of this thesis are threefold:

(1) Quantify the radiative impact of clouds on the GIS surface throughout the annual cycle.

(2) Characterize the surface energy budget and discern how ice sheet-atmosphere coupling modulates the influence of downwelling radiation on surface temperature.

(3) Elucidate how a comprehensive observational dataset can be utilized to evaluate modeled surface temperatures and processes responsible for their variability.

To address these objectives a series of three related studies are conducted resulting in two distinct publications and a third that will be submitted in Spring 2017. These studies comprise the following three chapters of this dissertation.

Chapter 2, published in *Journal of Climate* (Miller et al., 2015), investigates the impact of clouds on surface radiation at Summit Station. The technique used to determine the cloud radiative forcing (CRF) at the surface is similar to Intrieri et al. (2002) and is considered to be the instantaneous effect of a cloud on the radiation budget (Ramanathan et al., 1989). The Summit Station CRF results quantify how much additional radiation is at the surface compared to an equivalent clear-sky scene, which likely differs from other Arctic locations due to differences in

cloud (de Boer et al., 2009; Shupe et al., 2011), humidity (Cox et al., 2015), and surface albedo properties. CRF estimates, in conjunction with the co-located ICECAPS instrumentation, are used to investigate the influence of condensed liquid-water in mixed-phase clouds and the integrated cloud depth of ice-only clouds on the surface radiation budget. Generally, CRF results provide seasonally and synoptically independent estimates of the effects of clouds on the radiation budget; thus they are useful for satellite validation, model comparisons and expanding the pan-Arctic ground-based perspective.

Chapter 3, published in *The Cryosphere* (Miller et al., 2017), relates radiative drivers of the SEB to its responses, which determines how surface temperatures adjust to CRF throughout the annual cycle. Adapted techniques from previous studies are utilized to estimate the latent (Cullen, 2003), sensible (Persson et al., 2002), and ground heat (Hoch, 2005) fluxes, which complement the quality controlled radiation measurements (Chapter 2), producing a complete SEB annual cycle (July 2013 – June 2014). Estimating or averaging surface energy fluxes to 30-minute temporal resolution quantifies the contribution of each SEB term for monthly diurnal cycles and allows for illustrative case studies to explore details of ice-sheet/atmosphere interactions on time scales of hours. The roles of clouds and insolation are investigated by separating the SEB terms into forcing terms (associated cloud effects on forcing terms are explored in chapter 2) and response terms. Calculating annual responses of the sensible, latent, and ground heat fluxes quantifies the percentage by which these terms modulate changes of downwelling longwave plus net shortwave radiation, in order to produce the resultant surface temperature. By distilling complex interactions into seasonally varying statistical relationships, a process-based understanding of ice sheet/atmosphere interactions is developed to evaluate model performance.

Chapter 4 utilizes SEB estimates and process-based relationships from previous chapters to provide detailed model evaluation. Summit observations are utilized to investigate not only the existence of surface temperature biases but also identify potential culprits stemming from underlying discrepancies of surface energy fluxes and their observed process-based relationships. The focus is on a reanalysis product, an operational forecast model, and one fully coupled climate

model; ERA-Interim, Climate Forecast System version 2 (CFSv2), and a version of the Community Earth System Model (CESM). Reanalyses are often used as "truth" so understanding reasons for seasonal biases in surface temperatures provide guidance on how best to use the modeled output for validation and historical trend analysis. Analyzing reforecasts of historical time periods allows for the evaluation of the CFSv2 forecast system. The CESM "beta-07" version described in this thesis, while not identical to what will be released as the next version of the model (CESM2), is illustrative of strengths and weaknesses of the fully coupled climate model. Results from Miller et al. (2015) were used by the CESM community to evaluate the effectiveness of various cloud microphysical schemes in reproducing liquid-bearing clouds, thus highlighting the advantages of involvement from the observational community during model development.

In order to discern historical trends and project future climate changes with realistic Earth system feedbacks the underlying model physics must be adequate to represent observed physical processes. The occurrence of Arctic liquid-bearing clouds during all seasons is not properly represented by prominent climate models (Cesana et al., 2012), especially above Greenland (Kay et al., 2016a). Although strides have been made in representing small-scale processes across large modeling domains (Gettelman and Morrison, 2015), it remains inherently difficult to represent complicated cloud microphysical processes that sustain mixed-phase clouds (Shupe et al., 2013a). The Coupled Model Intercomparison Project (CMIP) suggests that there exists a significant spread in the exact magnitude of Arctic amplification due to a changing climate (Holland and Bitz, 2003). The spread in the magnitude of surface warming is related to differences in the surface radiation budget and is due, in part, to unrealistic cloud radiative forcing, especially above Greenland (Boeke and Taylor, 2016). Thus, the over-arching goal of this dissertation is to provide benchmark observations in central Greenland that are useful for evaluating and improving tools with greater temporal and spatial capabilities.

Chapter 2

Cloud radiative forcing at Summit, Greenland

2.1 Introduction

The Greenland Ice Sheet (GIS) has experienced increased surface melt extent and duration over recent decades (Mernild et al., 2011). Increases of GIS surface melt and subsequent enhanced glacial flow (Zwally et al., 2002) contribute to rising sea levels and increased fresh water flux into regional oceans. The surface energy budget modulates surface melting, and thus also the mass balance of the GIS, by controlling the surface temperature. Clouds exert a significant influence on the net radiative flux at the surface (Walsh and Chapman, 1998), therefore impacting the surface energy budget.

The shortwave and longwave radiative effect of clouds, or cloud radiative forcing (CRF), can be quantified by comparing the actual surface radiative flux to the flux during an equivalent clear-sky scene. In general, Arctic clouds have a warming effect on the surface, except for a period in the summer when the sun is highest and surface albedo is lowest (Curry and Ebert, 1992; Intrieri et al., 2002; Kay and L'Ecuyer, 2013). However, unlike many other Arctic locations, the central Greenland surface is covered by snow throughout the year, maintaining a high surface albedo in all seasons. Snow surfaces limit the ability of clouds to reduce absorbed solar radiation because clouds cannot substantially raise the planetary albedo. Moreover, surface-based inversions are a common feature above ice-covered surfaces, thus low-level clouds often emit at temperatures much warmer than the surface. Under these conditions, longwave radiative forcing typically dominates and clouds increase the downwelling flux compared to clear skies by 45-95 $W\,m^{-2}$ (Shupe and Intrieri, 2004;

Sedlar et al., 2011; de Boer et al., 2011). Additionally, optically thin clouds can act to maximize the combined shortwave and longwave radiative effects to produce maximum warming at the surface. A notable case in central Greenland occurred when low-level liquid-bearing clouds forced the surface temperature above the melting point of snow in July 2012 (Bennartz et al., 2013).

Surface temperatures exceeding 0°C are rare at Summit Station (72.6 °N, 38.5 °W), which is situated atop the GIS, approximately 3255 meters above sea level; the most recent of these melt events occurred in 1889 and 2012 (Nghiem et al., 2012). McGrath et al. (2013) predicts the 0°C isotherm altitude will consistently reach Summit by the year 2025, as estimated by surface temperature trends, suggesting more frequent future melting events at that location. Melting snow has a lower albedo than fresh snow due to changes in snow morphology and the presence of liquid water in the snowpack, providing a positive feedback by which more solar radiation is absorbed, acting to increase melting of the surface. The albedo feedback is already occurring at lower elevations and thus accelerating melting of the GIS in the ablation area (Box et al., 2012).

Changes in clouds and their properties have the potential to impart even larger impacts on the surface energy budget than changes in surface albedo, although it is unknown how a 0.09 $^{\circ}C\,year^{-1}$ warming trend over the GIS (McGrath et al., 2013) may, in turn, modify regional clouds. Climate models are deficient in their ability to distinguish cloud phase and accurately represent cloud fraction in the Arctic, leading to large biases in the surface energy budget (Cesana et al., 2012). Consequently, CRF results are useful for discerning which improvements to modeled cloud attributes are likely to have the greatest impact for accurately representing near-surface air temperatures atop the GIS in order to accurately project future melt.

In this paper we investigate the role that clouds play in the surface energy budget over the central GIS by examining the radiative effects of clouds over Summit Station. The surface albedo is relatively stable, providing the opportunity to isolate the effect of cloud properties on the annual cycle of CRF. Surface radiative fluxes, atmospheric state profiles, and cloud property measurements are used to quantify the radiative impact of clouds from January 2011 – October 2013. In addition, time-independent relationships are developed, with applicability to other places with high year-

round albedo, such as glaciers, multi-year sea ice, and regions of Antarctica. The three primary cloud-property influences we explore in this study are cloud presence, liquid-water occurrence, and integrated ice-cloud thickness.

2.2 Instrumentation

A comprehensive and integrated suite of instruments, measuring the atmospheric state above Summit Station in conjunction with radiative fluxes at the surface, provides linkages between cloud properties and the surface radiation budget. For all data sets a time-averaging window of three hours is used to remove the effects of inhomogeneities in the atmospheric scene while still resolving the diurnal cycle.

2.2.1 ICECAPS measurements

The Integrated Characterization of Energy, Clouds, Atmospheric state, and Precipitation at Summit (ICECAPS) project is a field campaign, in operation since May 2010, designed to characterize atmospheric properties at Summit similar to observational activities at other Arctic sites such as Barrow, Alaska (Stamnes et al., 1999) and Eureka, Canada. The instrument suite is designed to provide complementary information on atmospheric, cloud and precipitation properties. A comprehensive description of the ICECAPS instrumentation and the retrieved atmospheric properties is outlined by Shupe et al. (2013b), while pertinent details for the present study are outlined here.

A multi-instrument estimate of cloud presence (e.g., Shupe et al., 2011) includes data from a Vaisala ceilometer, a 35-GHz Millimeter Cloud Radar (MMCR), and a MicroPulse Lidar (MPL). The ceilometer reports cloud base height and occurrence, but is insensitive to high-altitude clouds (above 7-8 km) and has reduced sensitivity to clouds that are predominately ice. MPL data, currently available for 2011, includes backscatter information to detect cloud presence with enhanced sensitivity to ice particles, but is significantly attenuated by thick liquid layers in clouds. The MMCR is sensitive to most hydrometeors and does not attenuate significantly. With the exception of the ceilometer, these instruments are insensitive to the lowest $\approx$ 150 m and therefore may miss

occurrences of fog, cloudless ice crystal precipitation (diamond dust), and blowing snow. After interpolating the available estimates of cloud presence to the same time interval ($\approx$ 1 minute), a cloud fraction is calculated by taking the ratio of the total number of cases where cloud presence is identified by at least one instrument to the total number of data points over the 3-hour window. A clear-sky scene is identified when the cloud fraction is below a 1% threshold. Thus, a clear scene requires persistence of clear conditions for at least three hours while intermittent conditions will be classified as cloudy. The MMCR also provides vertical estimates of total cloud thickness as the sum of all range gates that have reflectivity greater than -60 dBZ. The integrated cloud thickness does not assume a continuous cloud layer, so the thickness of a multilayer cloud is the sum of the individual cloud thicknesses.

Temperature and moisture profiles throughout the troposphere are measured twice daily (0 UTC and 12 UTC) using Vaisala RS-92 radiosondes. High-temporal-resolution temperature profiles, accurate in the lowest few kilometers of the atmosphere, are retrieved using brightness temperatures from a microwave radiometer (MWR) (Miller et al., 2013). A total of four channels, from the Humidity And Temperature PROfiler (HATPRO) MWR (23.84 and 31.40 GHz) and high-frequency MWR (90.0 and 150.0 GHz), are used to retrieve column liquid water path (LWP) and precipitable water vapor (PWV), similar to Turner et al. (2007a). The two high-frequency channels increase sensitivity to baseline LWP and PWV (Crewell and Löhnert, 2003) resulting in PWV and LWP uncertainties of approximately 0.3 mm and 3 $g\,m^{-2}$, respectively. A conservative LWP threshold of 5 $g\,m^{-2}$ is used to identify the presence of liquid.

Best-estimate temperature and moisture profiles, extending up to 60 km above the surface, are created by merging radiosonde, MWR, and the European Centre for Medium-Range Weather Forecasts (ECMWF) operational model data. Data between radiosonde profiles are linearly interpolated in time for the heights below the lowest observed altitudes. For data above this altitude and for times where the radiosonde profiles are more than 14 hours apart, ECMWF data is blended with the existing radiosonde data such that there is a linear increase and corresponding decrease in weight, respectively. The high-temporal-resolution (at least every 40 minutes) statistical tem-

perature retrievals from the MWR are blended at low altitudes, such that the daily boundary-layer evolution is captured below 2 km. The radiosonde-derived moisture profiles are scaled uniformly with height so that the PWV matches the PWV derived from the MWR (Turner et al., 2003). Since low PWV values that occur at Summit can be close to, or less than, the uncertainty in the retrieval ($\approx$ 0.3 mm), the profile is not scaled if the percent error of the retrieval is greater than 50%. Alternatively, if the percent error is between 20-50% then the scaling is weighted, and a profile with a percent error below 20% is fully scaled. Finally, the merged profiles are averaged over the 3-hour time window.

2.2.2 Additional measurements

The Global Monitoring Division (GMD) at the National Oceanic and Atmospheric Administration (NOAA) provides measurements of atmospheric constituents and near-surface meteorological data (available from http://www.esrl.noaa.gov/gmd/dv/ftpdata.html). Weekly ozonesondes, launched from Summit Station, report profiles of ozone mixing ratios throughout the troposphere, extending into the stratosphere. In addition, monthly surface values of CO_2 mixing ratios are provided (Dlugokencky et al., 2014). Near-surface (approximately 2 m and 10 m above the surface) meteorological data is available at one-minute resolution, including pressure, temperature and relative humidity.

2.2.3 Radiation measurements

The net radiation at the surface (Q) is a combination of four broadband radiation components:

$$Q = LW\downarrow - LW\uparrow + SW\downarrow - SW\uparrow \tag{2.1}$$

Broadband radiative flux measurements, at approximately 2 m above the surface, are maintained by the Swiss Federal Institute of Technology (ETH) Zürich and have been operational at Summit Station in the current configuration since 2004. The upwelling and downwelling thermal emission (LW$\uparrow$ and LW$\downarrow$) are measured by a pair of Kipp and Zonen CG4 pyrgeometers, sensitive

to the spectral range 4.5 – 40 μm. The upwelling and downwelling solar irradiance (SW↑ and SW↓) are measured by a pair of Kipp and Zonen CM22 pyranometers, sensitive to the spectral range 200 – 3600 nm. External ventilation is implemented, designed to limit riming and frosting (henceforth, referred to collectively as riming), which can occur frequently at Summit Station. In addition, daily checks of the radiometer domes are performed by an on-site field technician in order to remove any ice that may exist.

During August 2013, NOAA-GMD installed a pair of Kipp and Zonen CM22 pyranometers, with the same spectral sensitivity as the ETH pyranometers, and a pair of Eppley PIR pyrgeometers, sensitive to the spectral range 3.5 – 50 μm. The shortwave measurements are aspirated with heated air and the longwave measurements are aspirated with ambient air. Daily checks for ice on the radiometer dome are performed by an on-site science technician. A dome correction factor is implemented for the longwave measurements similar to the Albrecht and Cox method (Albrecht and Cox, 1977), which uses the difference between the radiometer dome and case temperatures.

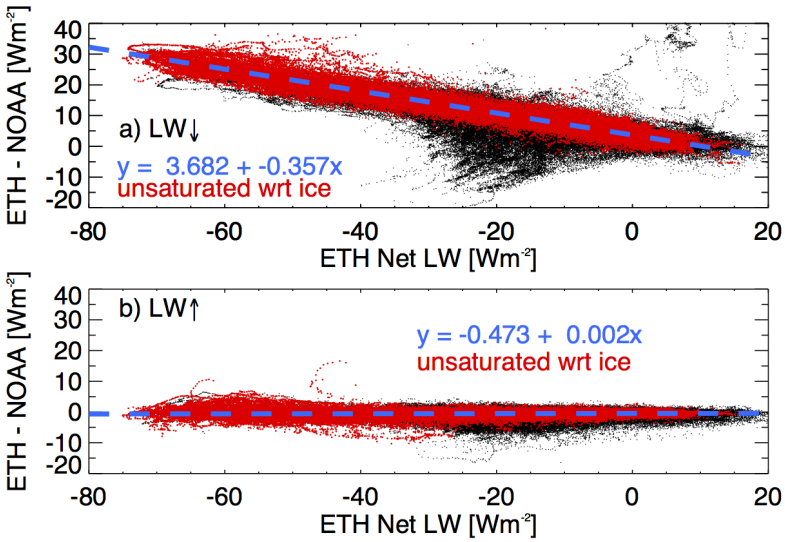

Figure 2.1: Differences between ETH and NOAA-GMD measurements from September 2013 to August 2014. a) LW↓ and b) LW↑ as a function of the ETH net LW (LW↓ - LW↑). Periods where the 2 m air is unsaturated with respect to ice are shown in red and represent values where riming and frosting are unlikely to occur. The linear equations (blue) represent the linear least squares fit to the residuals during periods where riming and frosting are unlikely (red).

Figure 2.1 shows comparisons between ETH and NOAA LW↑ and LW↓ measurements for one year of data (September 2013 – August 2014). Possible rimed cases are depicted in black during times where the air at 2 m is saturated with respect to ice. The uncertainty in the LW↓ is ±4 $W\,m^{-2}$ with a possible negative bias of 0-6 $W\,m^{-2}$ dependent on PWV (Gröbner et al., 2014). The comparison between the ETH and NOAA measurements indicates that there is an offset in the LW↓ measurement for clear sky scenes, when thermal cooling of the surface is greatest. Cox et al. (2014) reports a similar offset when comparing the ETH LW↓ measurements to estimates of LW↓ derived from the Polar Atmospheric Emitted Radiance Interferometer (P-AERI) at Summit. In addition, modeled clear-sky fluxes (see Section 2.3) are in basic agreement with the NOAA LW↓ measurements. Thus a linear fit of the LW↓ offset (ETH-NOAA) as a function of net LW is derived using measurements from periods that are likely not contaminated by rime (i.e., unsaturated with respect to ice) in order to adjust the ETH LW↓ data for the full January 2011 to October 2013 period. The differences in the ETH and NOAA LW↑ values are small (Figure 2.1b), hence, no adjustment is made to the LW↑ data.

Generally, the comparisons between the ETH and NOAA broadband SW measurements are in agreement. There is a 1.6 $W\,m^{-2}$ difference for the SW↑ component and -0.18 $W\,m^{-2}$ SW↓ difference during times when the sun is below the horizon. When the sun is above the horizon the difference of the SW↑ increases to 3.9 $W\,m^{-2}$. This difference is within the specified error of 5 $W\,m^{-2}$ for the CM22 pyranometers. Hence, the only adjustment to the ETH data is applied to the LW↓ component.

2.3 Calculating cloud radiative forcing

Cloud radiative forcing (CRF) is an estimation of a cloud's impact on the radiative flux at the surface. It is defined as the difference between the all-sky flux and clear-sky flux (Ramanathan et al., 1989) and is shown thusly,

$$CRF = Flux_{all-sky} - Flux_{clear-sky}\,. \tag{2.2}$$

CRF can be evaluated at the surface or at the top of the atmosphere. In this paper we present the surface CRF. Modeled broadband fluxes provide an estimate of the surface radiation budget under equivalent cloud-free conditions and are used to quantify the flux from atmospheric gases (i.e., the clear-sky state), which is ultimately modified by the optical and radiative properties of any hydrometers that may be present in an overlying cloud. Hence, a best-estimate thermodynamic profile (Section 2.2), which imparts its radiative signature on the ETH all-sky measurements, is utilized to calculate a corresponding clear-sky flux via a radiative transfer model.

While any such forcing can elicit a response of the surface-atmospheric system over time, the focus here is on the instantaneous effects of the clouds within a given, observed atmospheric profile. Alternative techniques have been used to derive CRF estimates at other Arctic sites (Dong et al., 2010), which involve an empirical curve-fitting technique to estimate longwave (Long and Turner, 2008) and shortwave (Long and Ackerman, 2000) clear-sky fluxes during cloudy scenes, using clear-sky scenes with similar environmental conditions. Due to the prevalence of surface-based inversions during clear-sky scenes (Miller et al., 2013), surface temperatures are colder during clear-sky scenes than during cloudy scenes. Hence, the cloudy-clear difference of the LW↑ component will usually be positive, manifesting as a smaller net LW CRF than calculated by the technique used in this paper. Thus, it is important to consider the technique used to calculate CRF when comparing results from different studies.

2.3.1 Radiative transfer model

The Rapid Radiative Transfer Model (RRTM, Clough et al., 2005) is used to estimate the clear-sky downwelling and upwelling broadband fluxes for both the SW and LW components. The water-vapor continuum absorption coefficients are obtained from MT-CKD, version 2.5 (Mlawer et al., 2012).

Contributions to RRTM input profiles are obtained from atmospheric measurements, described in Section 2.2. The inputs include: merged temperature and moisture profiles, a vertically constant CO_2 mixing ratio (estimated from a monthly surface measurement), and profiles of ozone

mixing ratios obtained from the most recent ozonesonde launch. Standard profiles for sub-Arctic winter conditions (McClatchey et al., 1972) are used for the following atmospheric constituents: N_2O, CO, CH_4, and O_2. Uncertainties in the concentrations of these four gases corresponds to tenths of $W\,m^{-2}$ uncertainty in calculated fluxes. A constant snow emissivity of 0.985 is used for the model input, estimated from the results of Warren (1982).

The RRTM SW albedo input is estimated from ETH measurements during clear-sky periods. Since albedo is dependent on solar zenith angle (SZA) (Warren, 1982), albedo in the radiative transfer model is parameterized using observations acquired during clear skies (Figure 2.2). Estimating the albedo from SZA results in a better comparison of SW fluxes to measurements in clear-sky conditions than an assumed, fixed value of the albedo. Clear-sky albedo is also dependent on other factors such as snow grain size and shape. Thus, not accounting for changes in snow morphology introduces uncertainty into the modeled SW values. Approximating clear-sky albedo using the linear fit in Figure 2.2 results in a root mean square (RMS) error of 0.076 for all clear-sky cases and a RMS error of 0.024 for cases with appreciable solar input (i.e., SZA $< 80°$). Despite the inherent uncertainty in representing clear-sky albedo using SZA, it is important to estimate the clear-sky albedo during a cloudy period in order to account for the cloud forcing of the broadband albedo. Bourgeois (2006) reports that for wavelengths less than 700 nm the albedo is greater than 0.9 and decreases with increasing wavelength. Optically thin clouds preferentially absorb shortwave radiation in the near infrared where the snow albedo is low, leading to an overall higher broadband albedo (Grenfell et al., 1981).

The surface (skin) temperature (T_{surf}) input into RRTM is estimated from the longwave measurements using the greybody approximation with the aforementioned surface emissivity of 0.985 (σ = Stefan-Boltzmann constant),

$$T_{surf} = [(LW\uparrow - (1-\epsilon)\,LW\downarrow)/(\epsilon\sigma)]^{0.25}. \tag{2.3}$$

This method for estimating T_{surf} is preferred in order to avoid difficulties associated with direct measurements or extrapolations from near-surface measurements. As a result, the modeled LW↑

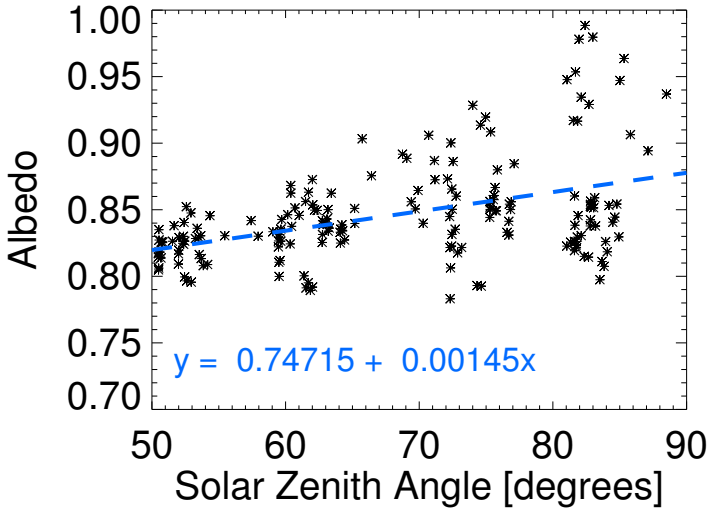

Figure 2.2: Albedo as a function of solar zenith angle, derived from ETH SW measurements, during clear-sky periods. The linear least squares fit is displayed in blue.

will be consistent with observations and is reconcilable with the definition of CRF used here because the instantaneous influence of a cloud will apply to the LW↓ component, in contrast to the LW↑ component, which will respond over time.

2.4 Evaluating CRF calculations

The difference between modeled clear-sky fluxes and measured fluxes during clear-sky conditions provides an estimate of possible uncertainties and biases implicit in the CRF calculations. Figure 2.3 shows the clear-sky residuals (ETH - RRTM) for the four broadband radiation components. The red lines include only observations that are likely rime-free radiometer observations as estimated from the daily science technician log book (i.e. the radiometer dome was reported as clear between consecutive checks). This criterion may filter out some periods when the domes are clear and might miss light riming events that sublimate before the subsequent daily check. Figure 2.3 indicates that riming has a small effect on the clear-sky estimates. This could be due to the fact that low-level fog accompanies the riming events and the multi-sensor cloud filter would identify periods when riming occurs as cloudy. Riming does occur frequently at Summit and filtering out data during times when the logbook suggests riming might have occurred omits 2759 of 7730 total data points. Removing 35.7% of the data is a significant data loss but ensures that the CRF results are not influenced by the presence of rime. Consequently, only unrimed data are used for the subsequent analysis.

The rime-free LW↑ residuals are close to zero (median difference of -0.4 $W\,m^{-2}$ and interquartile range of 0.9 $W\,m^{-2}$) because the longwave measurements are used to estimate the surface temperature input into RRTM. Hence, the primary difference between measured and modeled LW↑ is due to the reflected LW↓ component. The median rime-free LW↓ residual is 6.9 $W\,m^{-2}$ with an interquartile range (IQR) of 6.2 $W\,m^{-2}$. There are multiple potential sources of this bias. Aerosols were not included in the RRTM calculation and there could also be cases where hydrometeors overhead were not detected by the active cloud sensors; these would both contribute to the observed bias. Additionally, field-of-view considerations can contribute to the observed bias because the

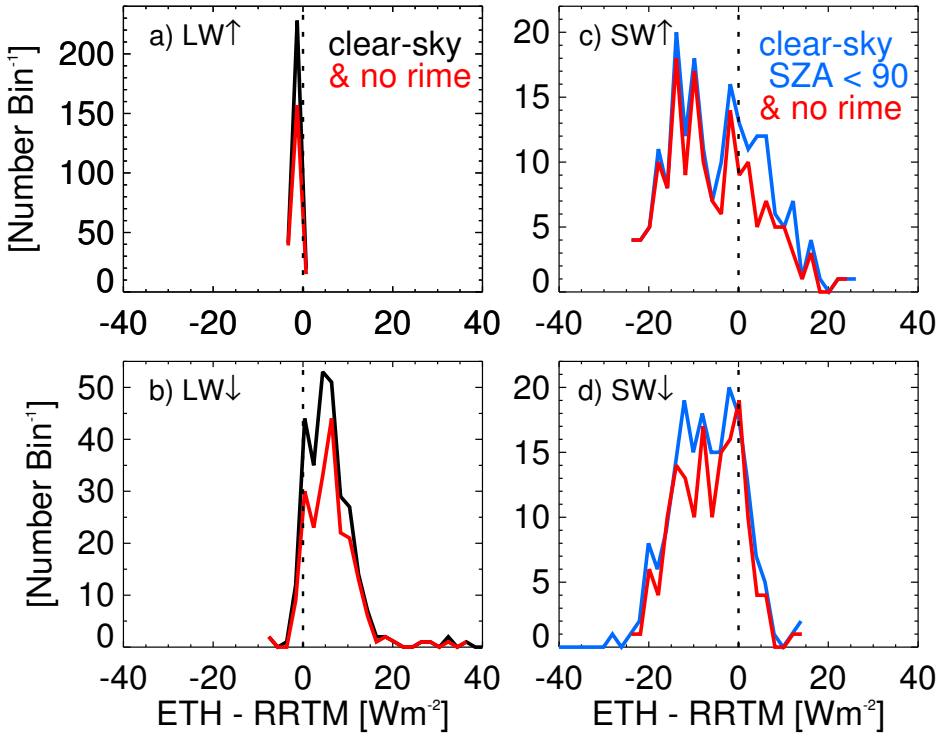

Figure 2.3: Clear-Sky distributions (number of occurrences per 2 $W\,m^{-2}$ bin) of a) LW↑ and b) LW↓ residuals (ETH - RRTM). Clear-sky distributions of c) SW↑ and d) SW↓ residuals when the solar zenith angle is less than 90°. Clear-sky distributions for cases when rime and frost are unlikely to be present according to the science technician logbook (for the same data in black or blue) are represented in red for all panels.

broadband radiometers have a hemispheric field of view as opposed to the much narrower perspective of the vertically pointing active cloud sensors. It is possible the hemispheric perspective is not completely cloud free, even though it is deemed clear overhead by the ICECAPS instrumentation during 99% of a 3-hour window (Henderson-Sellers and McGuffie, 1990). In addition, uncertainties in characterizing the atmospheric state resulting from measurement uncertainties, interpolation, or approximation can contribute to both bias and spread in the residuals. The uncertainty reported by Gröbner et al. (2014) of 4 $W\,m^{-2}$ for the LW↓ component likely increases at low temperatures and pressures (Su et al., 2008), which are common at Summit Station.

The SW↓ clear-sky rime-free irradiance residuals (Figure 2.3d) indicate a negative bias of -5.4 $W\,m^{-2}$ and an IQR of 11.7 $W\,m^{-2}$. The relatively large spread in the differences (ETH - RRTM) could be attributed to reported uncertainties in broadband shortwave measurements of 1.8% (Vuilleumier et al., 2014), lingering issues in modeling SW↓ (Kato et al., 1997), or uncertainties in characterizing the atmospheric state. Potential bias effects for clear-sky SW↓ related to aerosols, undetected hydrometers, and sampling field-of-view considerations all act in the opposite direction relative to the LW↓ bias and may also be dependent on the SZA.

Clear-sky SW↑ residuals (Figure 2.3c) indicate an IQR of 15.0 $W\,m^{-2}$, 3.3 $W\,m^{-2}$ higher than the IQR of the SW↓. The median rime-free SW↑ residual is also slightly larger at -7.4 $W\,m^{-2}$. This enhanced variability relative to SW↓ residuals is likely due to the added uncertainty of the clear-sky albedo estimates. Since some biases in SW↑ are due to biases in SW↓, these cancel when considering net SW, such that it has a much smaller net bias ($\approx$ 2.0 $W\,m^{-2}$).

While it is not clear how clear-sky uncertainties relate to all-sky uncertainties, clear-sky biases generally provide an outer bound on the biases expected for all-sky CRF calculations for each radiative component. The bias in total clear-sky CRF based on combining all radiation terms (LW↓ - LW↑ + SW↓ - SW↑) is 9.2 $W\,m^{-2}$. The clear-sky biases in LW↓ and SW↓ are partially due to the lack of modeled aerosols, undetected hydrometers, and field-of-view considerations. The influences of each of these would be smaller during cloudy scenes. For example, a partially opaque cloud below an aerosol layer would inhibit surface forcing by the overlying aerosols, limiting their

contribution to the overall CRF. In addition, in all-sky conditions differences between hemispheric and narrow vertical column fields-of-view can lead to variability in either direction, while only leading to a bias for the "clear-sky" subset. Therefore, it is to be expected that the potential biases associated with the all-sky CRF, and its components, are substantially less than those during clear-sky scenes (i.e., $< 9.2\ W\,m^{-2}$).

2.5 Seasonal cycle of surface flux

The surface energy budget at Summit has been reported briefly in summer by several studies. Cullen and Steffen (2001) describe the various components of the surface energy budget at Summit for the summer of 2000, finding that the net summer radiation is positive by an average of 14 $W\,m^{-2}$. On average the sensible heat, latent heat, and subsurface heat fluxes are small (-4, -3, and -3 $W\,m^{-2}$, respectively), leaving a residual of 4 $W\,m^{-2}$ that is within the uncertainty of the measurements. Kuipers Munneke et al. (2009) reports that during the summer the primary component for surface heating is the net shortwave radiation (peaking around 120 $W\,m^{-2}$), which outweighs the negative net longwave flux and turbulent fluxes. A stable boundary layer in winter, due to prevalent surface-based inversions, limits the turbulent fluxes and the surface energy budget is modulated primarily by the net longwave flux in the absence of sunlight.

Seasonal cycles of the radiative flux components as measured by the ETH radiometers are illustrated in Figure 2.4a. The SW↓ and SW↑ values peak in June with an average net SW of about 60 $W\,m^{-2}$. From October to February the net SW radiation is negligible. Counteracting this solar heating, the surface cools in the LW by emitting more LW radiation than is received from the overlying atmosphere. The surface emits the greatest amount of longwave radiation, and receives the greatest amounts of LW↓, during July when the maximum surface temperatures occur (Shupe et al., 2013b). The difference between LW↑ and LW↓ is greatest in the late spring and early summer, suggesting that the increase in surface temperatures is not driven by the LW↓ but rather by the increase in SW↓. The net radiation is fairly stable ($\approx$ -20 $W\,m^{-2}$) from autumn to spring, while the net radiative flux is positive for the majority of the time from May-August (Figure 2.4b).

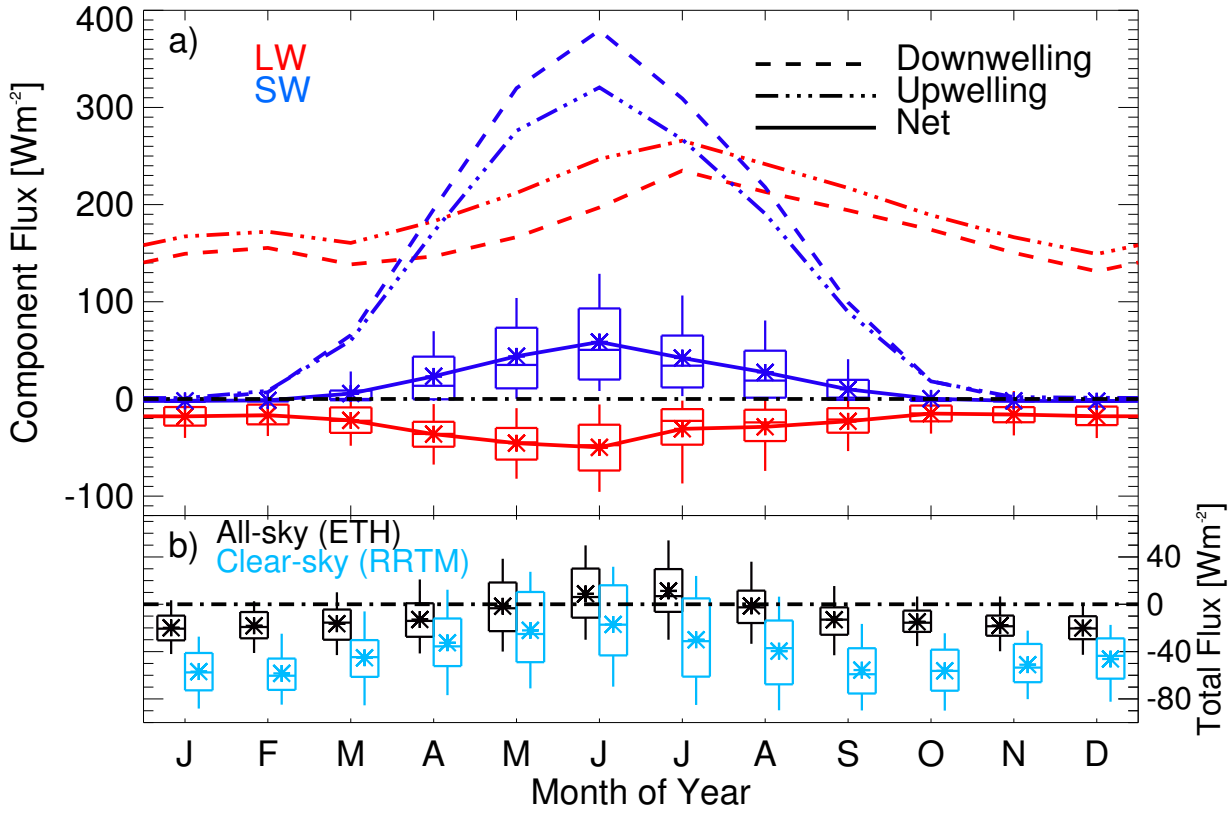

Figure 2.4: a) The annual cycle of ETH measured SW (blue) and LW (red), downwelling (dashed) and upwelling (dashed-dotted), mean monthly fluxes. The monthly net LW and SW distributions are represented by box-and-whisker plots (the box indicates the 25th and 75th percentiles, the whiskers indicate 5th and 95th percentiles, the middle line is the median and the * indicates the mean). b) The monthly distributions of the ETH measured (black) and RRTM modeled (light blue) total flux.

Variability of net LW and SW is mainly due to the diurnal and seasonal cycles of incident solar radiation. The diurnal cycle is largest in June when the solar influence peaks midday and the surface radiatively cools when the sun approaches the horizon near midnight. The mean net SW flux in July is slightly lower than in May, but what is more striking is the asymmetry in the net LW values between May and July. When the net radiation is considered (Figure 2.4b), July is similar to June. Comparatively, the net clear-sky flux, as modeled using RRTM, shows a decrease from June to July. Generally, clear-sky estimates are lower than the measured values indicating that clouds warm the surface relative to clear-skies in all months, as will be discussed in Section 2.6.

2.6 Cloud radiative forcing

The effect of clouds on the annual cycle of surface radiative fluxes is examined via the CRF (Figure 2.5). The SW↓ CRF is negative because clouds reflect incoming solar radiation, leading to cooling at the surface. Interestingly, the greatest SW↓ CRF and SW↑ CRF occurs in July, whereas the peak in SW↓ occurs in June (Figure 2.4a). The small magnitude of net SW CRF indicates that even in the summer the SW CRF is limited because of consistently high surface albedo values. The SW cooling effect peaks in July, with an average of -18 $W\,m^{-2}$ and the 5^{th} percentile approaching -55 $W\,m^{-2}$. The higher variability of net SW CRF in summer months is attributed to the diurnal cycle of incoming solar radiation (i.e., variability of SZA over the diurnal cycle), variability of cloud properties, and uncertainty in the clear sky albedo estimates.

Since the instantaneous CRF of LW↑ is negligible, the net LW CRF is driven by the LW↓ forcing (Figure 2.5b). Positive net LW CRF occurs year round as clouds warm the surface by insulating the surface, effectively reducing its cooling rate compared to clear skies. Similar to the SW CRF, there is an increase in the magnitude of net LW forcing from June to July. The average net LW CRF decreases from July (60 $W\,m^{-2}$) to the end of the year (December = 29 $W\,m^{-2}$), with a slight rebound in winter and a second minimum in April (30 $W\,m^{-2}$).

On average, the total CRF (Figure 2.5c), which combines LW and SW effects, is positive for all months of the year with an annual average value of 33 $W\,m^{-2}$. Including possibly rimed

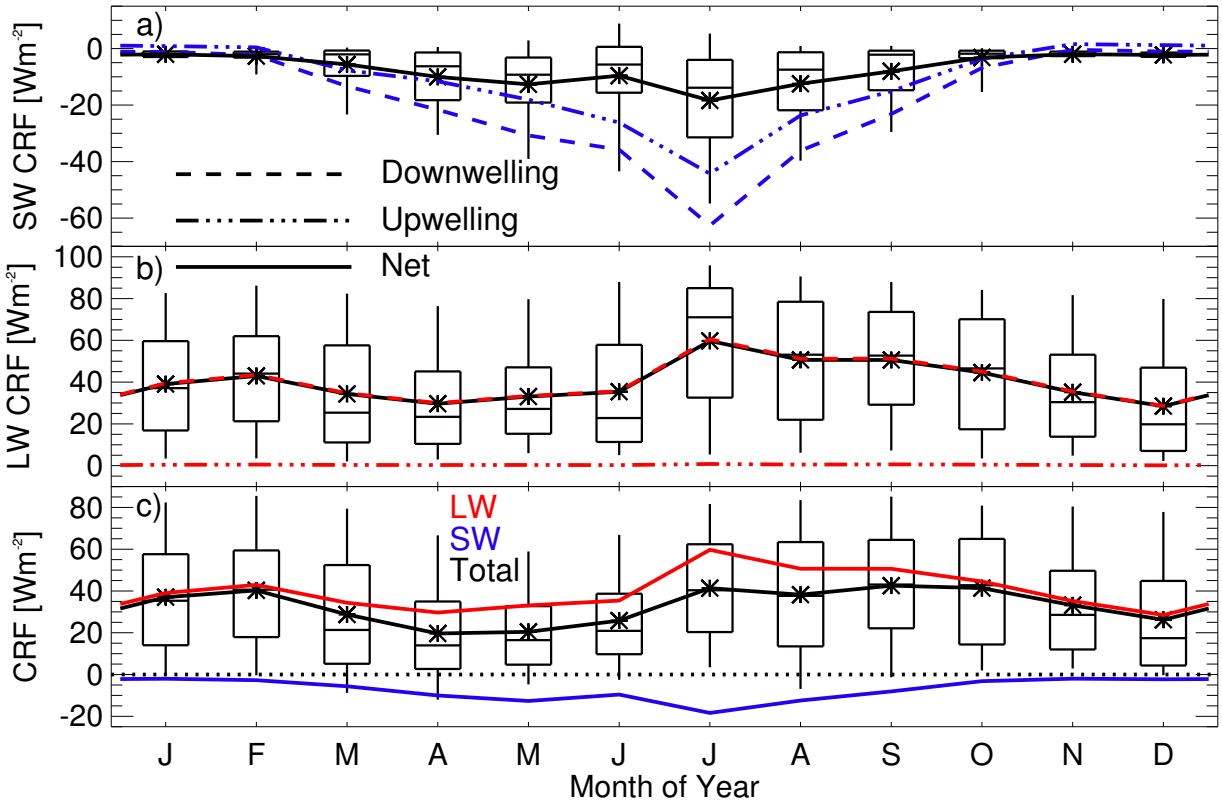

Figure 2.5: a) Monthly mean SW↓ (dashed), SW↑ (dashed-dotted), and net (solid) CRF and b) the equivalent LW CRF components. c) The monthly mean LW (red), SW (blue) and total (black) CRF. Distributions of net SW CRF (a), net LW CRF (b) and total CRF (c) are represented by box-and-whisker plots. The box indicates the 25th and 75th percentiles, the whiskers 5th and 95th percentiles, the horizontal line inside the box is the median and the $*$ indicates the mean.

data decreases the annual average by 3.6 $W\,m^{-2}$, with minimal seasonal influence. However, it is unclear if this decrease is due to eliminating periods with rime, which are often clear-sky, or due to measurement bias caused by the rime itself.

The emergence of negative SW CRF in the spring, combined with a relatively low LW CRF, leads to a spring minimum of the total CRF. During the study period (January 2011 - October 2013) there are 4971 unrimed 3-hour averaged data points and only 1.5% of the total CRF values are negative. A substantial surface warming, due to clouds, occurs in July associated with a sharp increase in the net LW CRF, which overwhelms the cooling effect of the corresponding increase in SW CRF magnitude. The large CRF in July is a departure from results reported for other Arctic locations, which have a period in the summer where the average total CRF is negative (Intrieri et al., 2002; Shupe and Intrieri, 2004; Dong et al., 2010; Kay and L'Ecuyer, 2013). The year round snow cover at Summit limits the amount of SW radiation absorbed by the surface, tempering the ability of the clouds to reduce the net SW, such that the total CRF is dominated by cloud LW warming effects in all months. The diminishing influence of the SW component from summer into fall, coupled with the slowly decreasing LW CRF, results in a relatively constant total CRF from July to October.

Since the annual cycle of the total CRF is primarily influenced by changes in the cloud properties and not large changes in albedo, the following subsections investigate the annual cycle of specific cloud properties and characterize their impact on the surface radiation.

2.6.1 Cloud fraction

Cloud presence is a first-order control that clouds have on the surface. Figure 2.6a depicts the annual cycle of cloud fraction using multi-sensor observations from January 2011 to October 2013. The overall cloud fraction for the study period is 86% with lower values in March (72%) and June (75%). The fact that cloud fraction does not exhibit an annual cycle suggests that it is not the primary driver in defining the annual cycle of total CRF.

Figure 2.7 shows that when the cloud fraction (based on 3 hour averages) is between 80% and

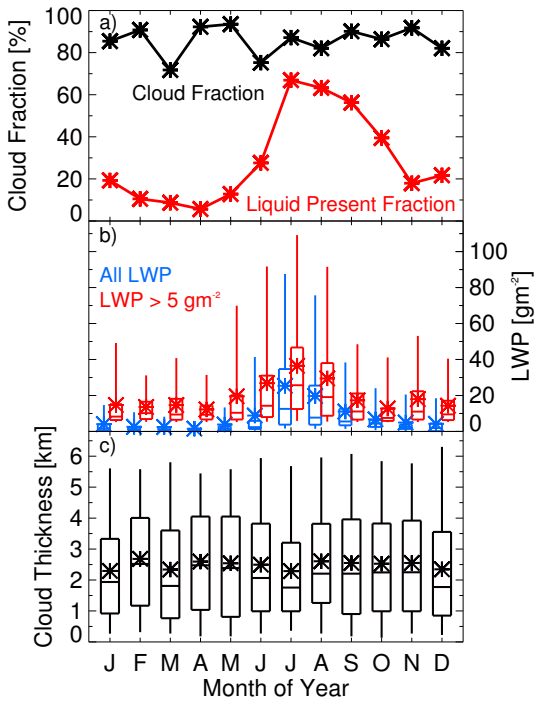

Figure 2.6: a) Monthly total cloud occurrence fraction (black) and fractional occurrence of liquid-bearing clouds (LWP $> 5\ g\,m^{-2}$, red). b) Monthly distributions of LWP for all cases (blue) and liquid-bearing clouds (red). c) Monthly distributions of vertically integrated cloud thickness when clouds are present. The box indicates the 25th and 75th percentiles, the whiskers 5th and 95th percentiles, the horizontal line inside the box is the median and the $*$ indicates the mean.

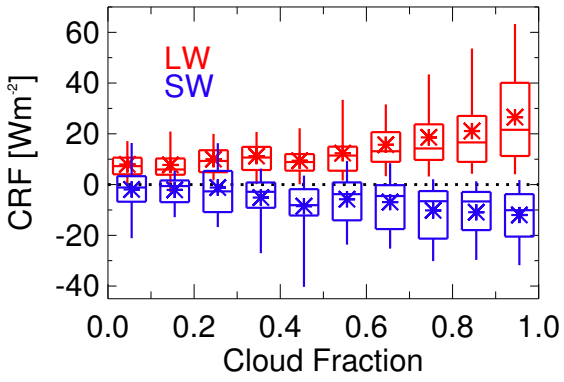

Figure 2.7: Statistics of LW CRF (red) and SW CRF (blue) as a function of cloud fraction over a 3-hour window. The SW data are for SZA $< 90°$. The box indicates the 25th and 75th percentiles, the whiskers 5th and 95th percentiles, the horizontal line inside the box is the median and the $*$ indicates the mean.

90%, the mean LW CRF is about 20 $W\,m^{-2}$, and is greater than 25 $W\,m^{-2}$ when the cloud fraction is more than 90%. A majority of monthly averages have cloud fractions near 90%, accounting for monthly LW CRF averages of 20-30 $W\,m^{-2}$ for most of the year. Over the western Arctic, Dong et al. (2010) and Shupe and Intrieri (2004) find a similar relationship between LW CRF and cloud fraction, but with higher mean LW CRF (55 $W\,m^{-2}$) for large cloud fractions. The smaller mean value found here is likely due to locational differences in cloud and environmental properties, but may also be influenced by a different time-averaging window. The mean SW CRF is about -10 $W\,m^{-2}$ for cloud fractions between 80-100% (Figure 2.7), offsetting less than half of the LW component. LW and SW CRF variability at the lower cloud fractions are partially due to clear-sky model errors discussed in Section 2.4, such as differences in field-of-view and uncertainty in the albedo estimates. The larger variability for the highest cloud fractions is due to variability in cloud microphysics and other environmental properties such as SZA.

2.6.2 Presence of liquid water

Cloud phase is important because the optical properties of liquid-bearing clouds differ from those of ice-only clouds. A significant increase in PWV and LWP occurs in July at Summit (Shupe et al., 2013b; Miller et al., 2013). An increase in water vapor decreases the transmissivity in the 18 μm - 35 μm window and thus the atmosphere emits more downwelling radiation (Turner and Mlawer, 2010). Yet, the effect of PWV on LW$\downarrow$ is small compared to the effect of a coordinated increase in LWP. The occurrence of liquid-bearing clouds at Summit peaks in July (67%), with similarly elevated values in August and September (Figure 2.6a). The largest month-to-month increase in liquid-bearing clouds is for the transition from June to July (+39%), associated with a smaller increase in overall cloud fraction (+12%).

In July and August, not only are there more liquid-bearing clouds, the clouds contain more condensed liquid compared to the rest of the year (Figure 2.6b). In July, when liquid water is present, the average amount throughout the entire atmospheric column is 36 $g\,m^{-2}$. June and August have similar LWP distributions when liquid clouds are present, but the overall liquid-bearing

cloud fraction is much lower in June. April has the lowest liquid-bearing cloud fraction (6%) and the least amount of supercooled water present in these clouds (12 $g\,m^{-2}$, on average). In general, the annual LW CRF cycle (Figure 2.5) follows the annual cycle of liquid-bearing cloud occurrence (Figure 2.6a), with a maximum in July and a minimum in April, suggesting the importance of these clouds on the total CRF.

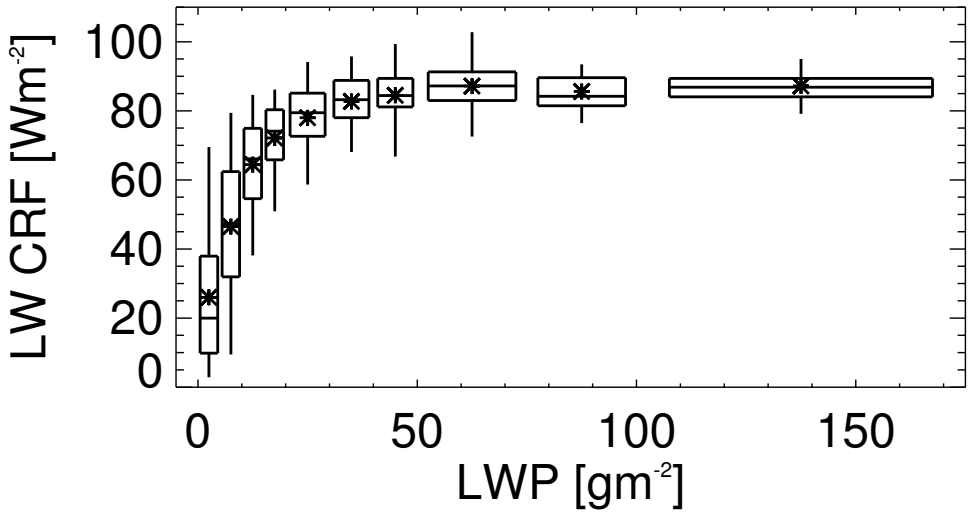

Figure 2.8: Statistics of LW CRF as a function of LWP over a 3-hour window. The box indicates the 25th and 75th percentiles, the whiskers 5th and 95th percentiles, the horizontal line inside the box is the median and the $*$ indicates the mean.

Cloud optical depth is a key factor in determining cloud transmissivity. Using LW optical depth approximations given by Bennartz et al. (2013), it is estimated that the transmission for a cloud with LWP = 20 $g\,m^{-2}$ is less than 10%. When considering a cloud containing 30 $g\,m^{-2}$ of liquid water, the transmission drops to 3%, effectively creating an opaque layer overlying the surface with an emissivity ($\epsilon = 1 - t$) close to 1 (Curry and Herman, 1985). Figure 2.8 shows a non-linear increase in LW CRF as LWP increases from 0 to 30 $g\,m^{-2}$. Above LWP = 30 $g\,m^{-2}$ the LW CRF asymptotes to a mean value of approximately 85 $W\,m^{-2}$. This LW saturation effect has been observed in other studies, although the specific asymptote value varies and is dependent on

such factors as cloud height, temperature and hydrometeor size (Shupe and Intrieri, 2004). Results near Svalbard indicate that LW CRF asymptotes to approximately 75 $W\,m^{-2}$ (Sedlar et al., 2011), while those in the Beaufort Sea asymptote to 65 $W\,m^{-2}$ (Shupe and Intrieri, 2004). Inexplicably, at Barrow, Alaska Dong et al. (2010) show a linear increase in LW CRF (up to $\approx$ 70 $W\,m^{-2}$) with an increase in LWP (up to $\approx$ 150 $g\,m^{-2}$) and no saturation effect.

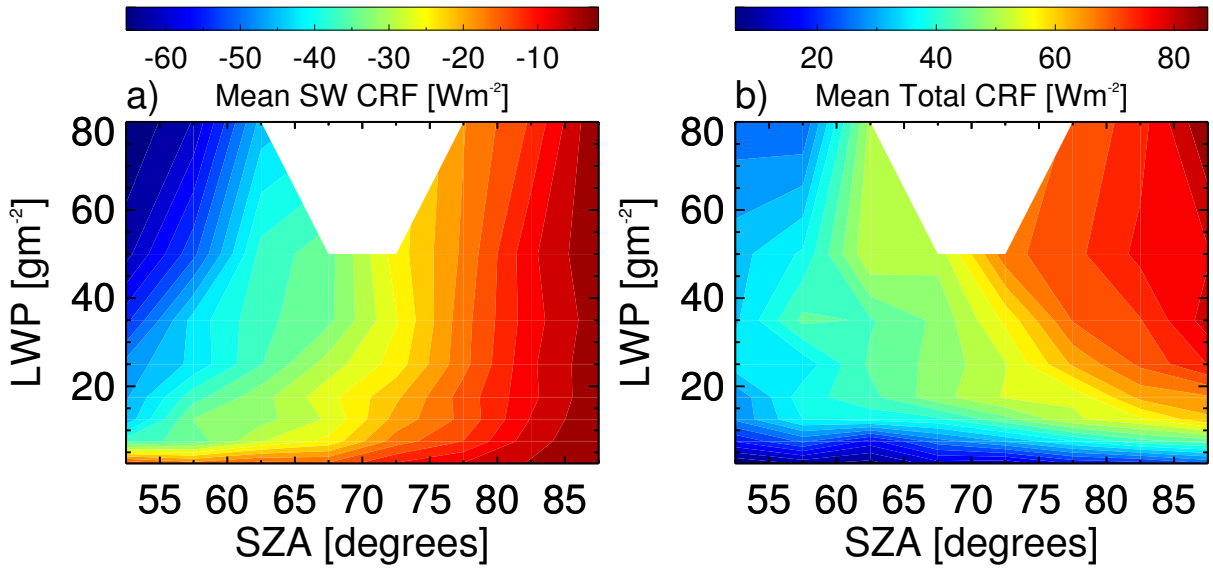

Figure 2.9: a) Mean SW CRF and b) mean total CRF, binned according to solar zenith angle and LWP, for the time period spanning January 2011 – October 2013.

SW CRF is not only a function of LWP but also a function of SZA (Figure 2.9a). The dependence of SW CRF on SZA has been demonstrated above sea ice by Fitzpatrick and Warren (2005) and Shupe and Intrieri (2004). Large SZA corresponds to small SW$\downarrow$ flux and thus a lower overall SW CRF potential, and visa versa. For SZA $< 65°$ an increase in LWP leads to an increase in the magnitude of SW CRF. Mean SW CRF values below -60 $W\,m^{-2}$ can occur for cases of low SZA and large amounts of liquid water. For SZA $> 65°$ the SW CRF sensitivity to LWP is limited to a much smaller range (LWP < 20 $g\,m^{-2}$).

SW CRF, unlike LW CRF, remains sensitive to variations in LWP greater than 30 $g\,m^{-2}$ for relatively low SZA (Figure 2.9a). The SW optical depth, affecting the direct transmission,

is approximately double that of the LW optical depth (Petty, 2006). Even though the direct transmittance of an optically thin (LWP = 10–40 $g\,m^{-2}$) liquid-bearing cloud is lower for shorter wavelengths, the overall transmittance is higher due to the forward scattering of SW radiation. Forward scattering is more pronounced at a lower SZA. In addition, a photon with a high incidence angle will travel through a longer path length through the atmosphere and have a greater chance of being absorbed before reaching the surface. Hence, the decreased sensitivity of SW CRF to changes in LWP at high SZA is likely due to a decrease in the diffuse component of SW↓.

Figure 2.9b depicts mean total radiative forcing that liquid-bearing clouds impart on the surface as a function of SZA. Since the maximum SW cooling of -65 $W\,m^{-2}$ (Figure 2.9a) is smaller in magnitude than the more prevalent maximum warming of 85 $W\,m^{-2}$ (Figure 2.8) clouds warm the surface under all conditions. For times when the sun is close to the horizon (high SZA), the total CRF is dominated by LW effects. However, when the sun is higher in the sky, SW cooling effects become somewhat more important at the highest observed LWPs. At these times, optically thin clouds provide the maximum warming of the surface. The specific LWP value that produces the maximum CRF appears to be larger at higher SZA. The 11 July 2012 Summit case study investigated by Bennartz et al. (2013) reports that without a LWP between 10–40 $g\,m^{-2}$ surface temperatures would not have exceeded the melting point of snow, even during times of peak insolation. Hence, thin liquid-bearing clouds are a significant factor in warming the surface during the summer months.

2.6.3 Ice phase clouds

In addition to cloud presence and phase, the vertically integrated cloud depth can be an important factor in determining its overall optical depth and consequently the radiative forcing at the surface. There is no clear seasonal cycle in the integrated cloud thickness (Figure 2.6c); the average cloud thickness for all months is between 2-3 km, suggesting that cloud thickness is of secondary importance relative to cloud phase.

Figure 2.8 shows that for small LWP values, the LW CRF varies significantly, ranging from

nearly 0-70 $W\,m^{-2}$ for clouds with LWP $< 5\ g\,m^{-2}$. Cases with LWP $< 5\ g\,m^{-2}$ (i.e., those with little or no liquid) are investigated further in order to characterize the influence of cloud thickness on CRF for clouds composed predominantly of ice.

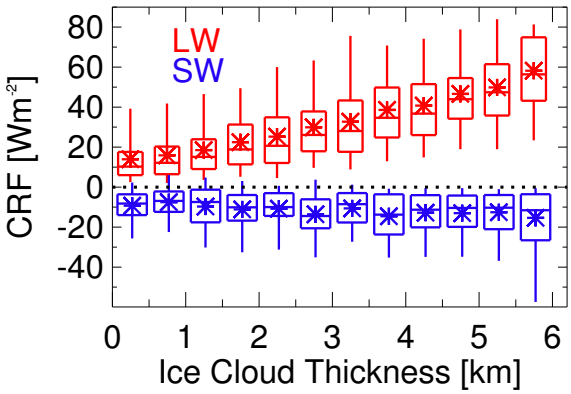

Figure 2.10: Statistics of LW CRF (red) and SW CRF (blue) as a function of cloud physical thickness for clouds consisting of predominately of ice (LWP $< 5\ g\,m^{-2}$). The SW data are for SZA $< 90°$. The box indicates the 25th and 75th percentiles, the whiskers 5th and 95th percentiles, the horizontal line inside the box is the median and the $*$ indicates the mean.

For mixed-phase clouds, de Boer et al. (2011) indicates that CRF is sensitive to the optical depth for ice, which is dependent on the ice water path. The primary determinant of the optical depth of an ice-phase cloud is the area and number concentration of ice crystals (Curry et al., 1990). Cloud thickness is used as a proxy here for the total amount of ice in the column even though the number concentration and hydrometeor size can vary for each atmospheric layer. Figure 2.10 depicts a linear relationship of LW CRF as a function of the integrated depth of the ice-cloud. The variability in each 0.5 km bin is likely due to the aforementioned properties of the ice crystals, while the increase in LW CRF is due to an increasing amount of ice in the column associated with the cloud thickness. The SW CRF, for times when the sun is above the horizon, has a weaker linear relationship with a shallower slope compared to the LW CRF. The average LW CRF of the thickest ice clouds (6 km) is still less than the LW CRF for optically thick liquid-bearing clouds. Thus, while ice properties can have important radiative effects, liquid properties dominate.

2.7 Summary

The radiative influence of clouds above Summit, Greenland is investigated for the time period of January 2011 – October 2013. Cloud radiative forcing, defined as the instantaneous radiative effect that clouds have in an atmospheric scene, is calculated by subtracting a modeled clear-sky radiative flux from the measured all-sky flux. Modeled fluxes are calculated using measured atmospheric thermodynamic profiles, estimated values for surface temperature and clear-sky albedo, and other parameters. Comparing modeled and measured fluxes during clear-sky scenes suggests that the CRF calculations could be biased by as much as 9.2 $W\,m^{-2}$ as a result of not including aerosols in model calculations, differences in instrument viewing geometry, and other sources of model uncertainty. However, the bias in cloudy-sky CRF is expected to be smaller than this bias because aerosol forcing and field-of-view inconsistency biases are diminished under cloudy scenes.

Average monthly CRF values are positive year round, with an annual average of 33 $W\,m^{-2}$. In addition, 98.5% of all quality controlled 3-hourly data indicate that clouds above Summit Station act to warm the GIS. A cloud decreases the net amount of SW radiation at the surface when the sun is above the horizon, yet the magnitude of the cooling effect is limited by the high year-round surface albedo at Summit. Thus, the annual cycle of total CRF is dominated by the downwelling LW component. As a consequence of an increase in radiative flux at the surface, the net surface all-sky radiative flux is positive for a majority of the time in June and July and positive during 34% of the entire study period.

At Summit Station, due to a relatively constant cloud fraction ($\approx 86\%$) and cloud thickness throughout the year, the annual variability in liquid-bearing cloud properties largely drives the annual cycle of CRF. For LWP above 30 $g\,m^{-2}$, a cloud becomes optically opaque to longwave radiation with a resultant LW surface warming of approximately 85 $W\,m^{-2}$. The magnitude of the SW cooling effect only approaches the magnitude of the LW warming effect for large LWP and low SZA but generally SW cooling is smaller than the LW warming. For the smallest observed SZAs, the maximum surface warming is achieved under the influence of optically thin (LWP =

10–40 $g\,m^{-2}$) liquid-bearing clouds. Interestingly, at Summit Station, the maximum warming due to clouds occurs in the late summer and early autumn due to a relatively constant surface albedo and marked increase from June to July in the LW warming effect of liquid-bearing clouds. This result is in contrast to other regions of the Arctic where the magnitude of SW cooling effect is larger than the LW warming effect for periods during the summer (Curry and Ebert, 1992; Shupe and Intrieri, 2004; Dong et al., 2010; Kay and L'Ecuyer, 2013), leading to a minimum in the total CRF (maximum cooling) in July. The minimum CRF in central Greenland occurs in the spring, when there are a limited number of liquid bearing clouds to warm the surface and the shortwave shading effect is a factor in lowering the total CRF at the surface.

Clouds consisting predominately of ice can also play an important role in warming the surface of the GIS. An increase in the integrated thickness of an ice cloud induces a response in the LW CRF that is greater in magnitude than the SW CRF. Hence, ice clouds warm the surface throughout the year, although they have a limited influence in the late summer when more liquid is present.

Cloud occurrence, liquid water path, and integrated ice cloud thickness all impact the atmospheric optical depth above the GIS, influencing the magnitude of warming at the surface. A change in the frequency of occurrence and/or microphysical properties of clouds over Summit will have implications for the net radiative flux at the surface and will enhance or temper the effects of a warming Arctic atmosphere. An increased (decreased) presence of clouds, especially those containing liquid water, would alter the current annual cycle of CRF at Summit by increasing (decreasing) warming of the surface. As the 0°C isotherm encroaches upon central Greenland in the next few decades, warming due to ubiquitous Arctic clouds will play an important role in determining the mass balance of the GIS.

Chapter 3

Surface energy budget responses to radiative forcing at Summit, Greenland

3.1 Introduction

The exchange of energy at the Greenland Ice Sheet (GIS) surface must be thoroughly characterized to fully understand the processes that govern surface temperature variability, which is important in monitoring and modeling ice sheet mass balance (Box, 2013). Observations suggest near-surface temperatures are increasing; the GIS is showing a trend toward greater spatial melt extent (McGrath et al., 2013) with increased melt runoff due to atmospheric warming (Hanna et al., 2008; Tedesco and Fettweis, 2012). The amalgamated freshwater runoff, in combination with ice discharge, determines how this major reservoir of northern hemispheric ice affects freshwater input into the North Atlantic and Arctic oceans and, subsequently, global ocean circulation and sea level rise. Surface melt processes currently account for approximately half of the total mass loss of the entire GIS (van den Broeke et al., 2009), and during prolonged periods of elevated surface temperatures this proportion is even greater (Smith et al., 2014). The melt process occurs in two steps. First, energy flux to the surface is used to increase the surface temperature. Then, after the melting point is reached, excess net surface energy flux is used to convert ice into liquid water. As an increasing area of the interior GIS approaches the melting point of snow in summer, spatial and temporal variations of the net surface energy flux are paramount in determining when the melting point is reached, over what spatial area this occurs, and the amount and rate of melt after this threshold is reached.

The surface energy budget (SEB) is a balance of radiative, turbulent, and ground heat fluxes,

which are coupled through a variety of processes. Once the surface temperature reaches the melting point of snow, additional energy goes toward melt, limiting the surface temperature to 0 °C. In the absence of phase change, however, a change in one of the SEB terms must be balanced by a change in another term or combination of terms. Importantly, the surface temperature is related to multiple SEB terms including upwelling longwave radiation, turbulent sensible heat, and ground heat fluxes. Over timescales long enough for the surface temperature to adjust, closure of the SEB is achieved and all of the energy exchange at the surface is accounted for. Because of the high emissivity (and hence high longwave absorptivity) of the snowpack, the surface is able to adjust relatively quickly to longwave influences (e.g., whether that is a warm cloud or a cold, clear sky). In contrast to its efficient ability to absorb longwave radiation, the GIS has a high shortwave albedo and reflects much of the incoming solar radiation. Liquid-bearing clouds are frequent above the GIS during summer (Shupe et al., 2013b) and have strong implications for increasing melt extent (Bennartz et al., 2013) and meltwater runoff (Van Tricht et al., 2016). In fact, clouds act to radiatively warm the central GIS throughout the year (Miller et al., 2015; Van Tricht et al., 2016), more than would occur via solar radiation acting alone, as a result of the year-round high surface albedo. Thus, the primary radiative influences on raising surface temperatures in this region are the solar zenith angle and occurrence of clouds.

A change in the downwelling radiative flux caused by clouds and/or solar radiation will induce a response of the atmospheric boundary layer and surface. Boundary-layer depth and stability are influential for exchange processes, such as sublimation fluxes, which modulate accumulation (Berkelhammer et al., 2016). Miller et al. (2013) show a degradation of the surface-based temperature inversion in the presence of liquid-bearing clouds, which impacts the near-surface stability (Hudson and Brandt, 2005) and thus turbulent mixing. A regional modeling case study by Solomon et al. (2017) indicates also that the response of turbulent and conductive heat fluxes to cloud radiative forcing (CRF) is important when considering surface–atmosphere interactions. Investigating these responses and interactions throughout the year is paramount for discerning the net effect of liquid-bearing clouds on surface temperatures and, consequently, on subsurface temperatures and melt

processes.

The central GIS is a massive reservoir of snow and ice, responding to energy changes at the surface by conducting heat into or out of the subsurface. Thus, the ice sheet damps the effects of either strong radiative warming or cooling at the atmosphere–snow interface. Warmer subsurface temperatures, resulting from warming of surface temperatures, can change the snow morphology and precondition the surface to have less capacity for removing subsequent heat excesses generated by atmospheric processes (Solomon et al., 2017). Proper atmosphere–ice sheet coupling is important to allow for physically realistic radiational cooling at the surface, in order to minimize surface temperature biases in forecast models (Dutra et al., 2015).

Regional and global climate models are a critical tool for understanding the fate of the GIS and attempt to capture the nontrivial interactions between the atmosphere and the GIS. Early studies parameterized the SEB of the GIS using meteorological measurements from summer camps in western Greenland and observations of albedo from satellites (van de Wal and Oerlemans, 1994; Konzelmann et al., 1994). More recently, computationally advanced, fully coupled climate models project enhanced surface melt as GIS surface temperatures increase under future CO_2 forcing scenarios (Vizcaíno et al., 2014). However, these state-of-the-art climate models have surface temperature biases over the GIS, likely due to the under representation of liquid-bearing clouds (Kay et al., 2016a). To better understand and represent the important processes that currently hinder models, detailed surface-based observations are valuable.

In western Greenland, detailed measurements of the surface mass balance (van de Wal et al., 2005; Charalampidis et al., 2015), surface radiation balance (van den Broeke et al., 2008), and surface energy balance (van den Broeke et al., 2011) have been reported, all of which focus on the ablation zone. In central Greenland, the most sophisticated and comprehensive long-term observations of surface energy budget are made at Summit Station. While a majority of the published literature has focused on the summer season (Cullen and Steffen, 2001; Kuipers Munneke et al., 2009), some studies have targeted SEB annual cycles in 2000–2001 (Cullen, 2003), 2001–2002 (Hoch, 2005), and 2000–2002 (Cullen et al., 2014). In addition, various studies have focused

on specific components of the SEB, such as surface latent (Box and Steffen, 2001) or sensible heat (Cohen et al., 2007; Cullen et al., 2007; Drüe and Heinemann, 2007) fluxes. Annual surface radiation fluxes have been reported at Summit by van den Broeke et al. (2008), Cox et al. (2014), and Miller et al. (2015), as well as longwave flux divergence in the boundary layer by Drüe and Heinemann (2007) and Hoch et al. (2007). Yet, prior to May 2010 there have been limited ground-based measurements of the atmospheric state and cloud properties to complement these temporally sporadic SEB investigations and to support process-based understanding of SEB variability on timescales from minutes to seasons.

This study uses comprehensive ground-based measurements to investigate interactions between the atmosphere and the central GIS throughout the year in order to understand how energy exchange drives temporal variability in surface temperature. Summit Station is currently within the accumulation zone, recording only two melt events since 1889 (Nghiem et al., 2012). The lack of melt events provides the opportunity to examine relationships between the various surface energy fluxes in all seasons without the energetic influence of phase change at the surface. We characterize the annual and diurnal cycles of the radiative, turbulent, and conductive heat fluxes for 1 year and evaluate SEB closure. Next, using a unique complement of data/measurements at 30 min temporal resolution, we present a pair of case studies to illustrate cloud effects on the balance of energy at the surface and, consequently, the subsurface snow in central Greenland. Finally, we investigate the seasonal responses of the turbulent heat fluxes, subsurface heat flux, and upwelling longwave flux to changes in downwelling longwave and net shortwave fluxes, establishing process-based energy flux relationships.

3.2 Measurements and methods

Near-surface instrumentation at Summit Station (72° N 38° W, 3211 m) is used to characterize the surface energy budget. Net radiative (Q), turbulent sensible (SH), turbulent latent (LH), and total subsurface (G) heat fluxes determine the net surface flux (F_s) according to the following

equation:

$$F_{\mathrm{s}} = Q + SH + LH + G. \tag{3.1}$$

The total subsurface heat flux (G) considered here is a combination of the conductive heat flux (C) and heat storage in a near-surface layer (S), detailed in Sect. 3.2.5. Each of these four terms is defined such that a positive value sends energy towards the surface and vice versa. For all measurements described here, a 30 min time window is used; this time window was chosen to fit the constraints set by eddy covariance calculations for sensible turbulent flux (Sect. 3.2.3) but is sufficiently brief to capture both the diurnal cycle and the SEB response to atmospheric variability of interest here.

All SEB terms are estimated for 75.3 % of an annual cycle, spanning July 2013–June 2014, although Q, SH, and LH are also measured prior to July 2013. The techniques used to calculate each SEB term, the data availability periods, and associated uncertainties are outlined in the following subsections. The estimated uncertainty in each SEB term is summarized in Table 3.1. While each component of the SEB has its own uncertainty, at times the various estimates use the same input and are thus not independent. For example the longwave measurements are used to derive the skin temperature, which is input into both the bulk sensible heat flux and conductive heat flux estimates.

Table 3.1: Estimated uncertainty in each surface energy budget term.
* SW↑ in 2014 = 2.8 % > 5.0 $W\,m^{-2}$.

LW↓ or LW↑	SW↓ or SW↑ *	SH	LH	C	S
5.0 $W\,m^{-2}$	1.8 %	8.7 $W\,m^{-2}$	60 %	26 %	80 %
	> 5.0 $W\,m^{-2}$		> 8.0 $W\,m^{-2}$	> 3.0 $W\,m^{-2}$	> 10.0 $W\,m^{-2}$

3.2.1 Meteorological and snow measurements

Redundancy of many direct measurements used to derive the SEB components is imperative in the harsh Arctic environment where frost, rime, and extreme cold create operational challenges.

Certain measurement techniques are only valid during specific atmospheric conditions and operational temperature ranges of the instrumentation. As a result, redundant data streams and multiple independent methodologies are considered whenever possible to investigate suspected biases and fill in data gaps during instrument downtime. Table 3.2 summarizes the measurements made by the various instruments described below.

Table 3.2: List of measurements at Summit Station used in this study. Nominal heights are given for measurements made at two levels.

Parameters measured ($\approx$ heights)	Instrument	Project
Atmospheric temperature	Vaisala RS92 radiosondes	ICECAPS
Snow temperature	Campbell Scientific 107 temperature probes	CIBS
Surface height	Campbell Scientific SR-50A sonic ranger	CIBS
Temperature (2, 10 m)	Logan RTD – PT139 special order	NOAA/GMD
	Vaisala HMP 155 temperature probes	CIBS
	Metek USA1 sonic anemometers	CIBS
Wind speed (2, 10 m)	Metek USA1 sonic anemometers	CIBS
	Met One 010-CA cup anemometers	CIBS
Relative humidity (2, 10 m)	Vaisala HMP 155 RH probes	CIBS
Water vapor mix. ratio (2, 10 m)	Picarro L2120 spectrometer	CIBS
Barometric pressure	Setra 270	NOAA/GMD
LW$\downarrow$, LW$\uparrow$	Kipp and Zonen CG4 pyrgeometers	ETH
	Eppley PIR pyrgeometers	NOAA/GMD
SW$\downarrow$, SW$\uparrow$	Kipp and Zonen CM22 pyranometers	ETH
	Kipp and Zonen CM22 pyranometers	NOAA/GMD
Liquid water path	RPG MWRs - HATPRO and HF	ICECAPS
Precipitable water vapor	RPG MWRs – HATPRO and HF	ICECAPS
Cloud occurrence	Millimeter cloud radar – 35 GHz	ICECAPS

Twice daily Vaisala RS92 radiosondes (0 and 12 UTC) from the Integrated Characterization of Energy, Clouds, Atmospheric State, and Precipitation at Summit (ICECAPS, Shupe et al., 2013b) project are used to directly measure the atmospheric temperature with an uncertainty of 0.5°. A near-surface meteorological tower, maintained by the National Oceanic and Atmospheric Administration's Global Monitoring Division (NOAA/GMD), is the primary source of the near-surface ($\approx$ 2 and $\approx$ 10 m) temperature measurements (Logan RTD – PT139 special order) with a specified resolution of 0.1 °C. An experiment on Closing the Isotope Balance at Summit (CIBS), approximately 1 km northeast of the NOAA tower, included a broad suite of advanced meteorological measure-

ments for evaluating surface exchange processes, including aspirated temperature measurements at 2 and 10 m. The CIBS instruments were mounted on a 50 m tower operated by the Swiss Federal Institute of Technology (ETH) Zürich. On average the CIBS 2 m temperatures are 0.72 °C greater than the NOAA/GMD 2 m temperatures with a root mean square (RMS) difference of 1.64 °C. A portion of the RMS difference is due to spatial distance between measurement locations and possibly also due to local variability in snow accumulation which would lead to differences in the measurement heights of the sensors. In addition, CIBS included Metek USA1 three-dimensional ultra sonic anemometers to directly measure orthogonal components of high-frequency fluctuations in temperature and wind speed. The sonic anemometers (20 Hz sampling rate), equipped with heated transducers to prevent riming or frost buildup, were mounted at 2 and 10 m on the 50 m tower. Before 19 January 2013 the heaters operated only when there were significant data dropouts due to rime/frost; after this date the heaters were on constantly. Comparison of the data before and after the heater configuration change indicate that sensible fluxes generated by the heating elements are sufficiently small that they are well within the measurement uncertainty. The high-frequency sonic anemometer wind speed measurements are averaged to estimate the mean 30 min wind speed. Redundant wind speed measurements are also made by CIBS cup anemometers, which have moving parts that have a frictional threshold that requires a wind speed of at least $0.5\,m\,s^{-1}$ for reliable measurements. Comparisons between the two measurements for conditions above $0.5\,m\,s^{-1}$ show a RMS difference of $1.75\,m\,s^{-1}$ and a bias of $-0.55\,m\,s^{-1}$ in the cup anemometer data.

Subsurface temperatures are measured by Campbell Scientific 107 temperature probes buried in the snow (every 20 cm in depth) near the 50 m tower. The height of the surface relative to the thermistor string is estimated from a downward facing sonic ranger mounted on the tower above the thermistor string. During the single year when the thermistor data were available (July 2013–June 2014) the surface height increased by 0.68 m. Due to scatter in the reported surface heights, the snow depths are smoothed using a 5-day running window to remove erroneous spikes in the snow depth. Realistic longer-term discontinuities due to actual snow events were maintained by limiting the period over which data smoothing occurred. Inexplicably, on 27 May 2014 the sonic ranger

reported an abrupt 17.8 cm decrease in the surface height. The near-surface thermistor variability indicates that this was unrealistic; hence an offset of −17.8 cm was applied to the thermistor depths thereafter through the end of the study period. The standard deviation over 30 min of the 1 min subsurface temperature data indicates that the variability decays as a function of depth because of a decline in the thermal effects of wind ventilation and direct solar heating due to solar penetration. To minimize the impact of these complicating issues a standard deviation threshold of 0.1 is used to determine that the acceptable minimum depth to use for the shallowest subsurface thermistor is about −20 cm.

The specific humidity at 2 and 10 m, which is needed for deriving LH, is calculated from the CIBS relative humidity, CIBS temperature, and NOAA/GMD pressure measurements. The saturation vapor pressure, at a given temperature, is calculated using the Goff–Gratch formulation and then multiplied by the relative humidity to get the vapor pressure. Specific humidity is proportional to the ratio of the vapor pressure to the difference in vapor pressure and air pressure. To provide continuity in the LH estimates the meteorologically derived specific humidity values are used as input to the LH flux calculations, while direct measurements of water vapor are used to estimate the uncertainty in this technique during overlapping time periods. From July 2012 to December 2013 direct measurements of water vapor mixing ratio are obtained via a Picarro model L2120 spectrometer, which was calibrated using a LiCor LI160 dew point generator (Bailey et al., 2015). The instrument directly samples air moisture content once an hour at multiple levels on the 50 m tower using a constrained inlet system to limit large ($> 50\,\mu m$) hydrometeors from being incorporated into the vapor measurements. Comparing meteorologically derived specific humidity values at approximately 1–2 and 9–10 m above the surface to the highly accurate Picarro measurements reveals a small bias of $+0.065\,g\,kg^{-1}$. The percent error, relative to the Picarro measurements, at the 2 and 10 m levels are 53 and 30 %, respectively.

3.2.2 Radiative flux

Four broadband radiation components comprise the net radiation at the surface (Q):

$$Q = \mathrm{LW}\downarrow - \mathrm{LW}\uparrow + \mathrm{SW}\downarrow - \mathrm{SW}\uparrow. \tag{3.2}$$

At Summit Station ETH maintains broadband radiative flux measurements, at approximately 2 m above the surface. The radiation station is located between the 50 m tower and the NOAA/GMD met tower. Kipp and Zonen CG4 pyrgeometers measure the upwelling and downwelling thermal emission (LW↑ and LW↓) in the spectral range of 4.5–40 μm and Kipp and Zonen CM22 pyranometers measure the upwelling and downwelling solar irradiance (SW↑ and SW↓) in the spectral range of 200–3600 nm. In this study the radiative flux measurements extend from January 2011 to June 2014.

Data processing for radiation measurements used here is similar to Miller et al. (2015), including corrections to the LW↓ components based on the net longwave radiation and comparison to co-located broadband radiation measurements operated by NOAA-GMD. The radiation components have an estimated Gaussian longwave radiation measurement uncertainty of 4–5 $W\,m^{-2}$ (Gröbner et al., 2014). Assuming an emissivity uncertainty of 0.005 a LW-derived surface temperature has an approximate uncertainty of 0.6 °C, which is derived from the radiation measurements thusly:

$$T_{\mathrm{surf}} = \left[\left(\mathrm{LW}\uparrow - (1-\epsilon)\ \mathrm{LW}\downarrow\right) / \left(\epsilon\sigma\right)\right]^{0.25}, \tag{3.3}$$

where surface emissivity (ϵ) = 0.985 and σ is the Stefan–Boltzmann constant. Comparing LW↑ to similar, proximate NOAA/GMD radiation measurements indicates that there is general agreement within the estimated 4–5 $W\,m^{-2}$ uncertainty of the longwave radiative components. Yet, for very cold surface temperatures (i.e., < -46 °C) differences between the NOAA/GMD and ETH LW↑ are more pronounced. Hence, a third degree polynomial was used to fit the difference between the ETH and NOAA/GMD LW↑ as a function of the ETH LW↑. A correction factor (y) was applied based on the measured ETH LW↑ (x) value according to $y = -14.99 + 0.1715x - 0.000668x^2 + 8.579 \times$

$10^{-7}x^3$, which assumes the more recently calibrated NOAA/GMD pyrgeometers are accurate. After applying the adjustments to LW↑ and LW↓ (Miller et al., 2015) the 1 min LW data are consistent with a total uncertainty of 4–5 $W\,m^{-2}$.

The surface albedo is determined by dividing the measured SW↑ by the measured SW↓ and for clear-sky days should have a minimum at solar noon. During 2014 an asymmetry in the diurnal cycle is observed in the measured albedo, where the albedo in the morning is up to 10 % lower than in the evening. The NOAA/GMD measurements, which are mounted on the same fixed arm, indicate the same issue (possibly a gradual slope to the surface due to snow drifts). There is good agreement between the ETH SW↓ measurements and the total direct plus diffuse SW↓ values, suggesting that asymmetry in the diurnal cycle of albedo is likely a problem in the SW↑ component. Hence, the SW↑ value is estimated in 2014 using the SW↓ value according to SW↑ = αSW↓, where α is the albedo. A linear relationship between albedo and solar zenith angle (Z) for 2011–2013 is used to estimate an albedo in 2014 according to $\alpha = 0.798 + 0.00107\,Z$. Comparing the measured SW↑ to the parameterized SW↑ yields an RMS difference of 5.7 $W\,m^{-2}$ for SW↓ $< 278\,W\,m^{-2}$ and 12.6 $W\,m^{-2}$ for SW↓ $> 278\,W\,m^{-2}$. Thus, the uncertainty in the parameterized SW↑ component is $\approx 5.7\,W\,m^{-2}$ for small sun angles and ≈ 2.8 % for larger SW↓ values. These uncertainty estimates are larger than the reported uncertainty in the measured SW components of 1.8 % (Vuilleumier et al., 2014) because, in addition to Z, albedo is dependent on other factors such as the optical thickness of overlying clouds and surface snow properties.

During periods of 2013 and 2014 the SW↓ component has a bias that is evident when the sun is below the horizon, hypothesized to be due to a grounding issue. A bias correction of 2.45 $W\,m^{-2}$ was applied to 20 November 2013 to 30 January 2014, determined by the average value when the solar zenith angle was greater than 95°. From 31 January 2014 to 14 April 2014 a bias correction of 4.61 $W\,m^{-2}$ is applied to the SW↓ to remove the negative bias.

3.2.3 Turbulent sensible heat flux

The net surface flux is influenced by the temperature of the overlying air; i.e., warmer near-surface air will increase the sensible heat transferred to the surface. Direct heat transfer, via conduction, from the atmosphere to the snowpack is only prominent very close to the surface; thus heat is primarily transferred via turbulent eddies. These eddies act to mix the air within the surface layer, reducing the vertical temperature gradient. Estimates of the sensible heat flux are calculated using two independent methods: eddy correlation (EC) method and the bulk aerodynamic method.

The EC method (e.g., Oke, 1987) calculates the covariance between the anomalies in the vertical wind (w') and temperature (θ') to determine the turbulent sensible heat flux according to the following equation:

$$\mathrm{SH} = \rho c_\mathrm{p} \overline{w'\theta'}, \tag{3.4}$$

where the constants are the density (ρ) and heat capacity (c_p) of air. By using direct measurements of wind speed and temperature from a three-dimensional sonic anemometer, an accurate calculation of the heat exchange at $\approx 2\,\mathrm{m}$ is obtained.

A 30 min averaging period is a short enough time window to exclude issues of nonstationarity while still long enough to include low frequency contributions to the turbulent heat flux. Various quality-control (QC) measures are implemented to ensure the data is representative of the entire sensible heat flux during the 30 min window. QC measures exclude large changes in wind speed or wind direction, upwind contamination by the experimental apparatus, and $\pm 30\,\%$ deviations from characteristic $-5/3$ slope in the inertial subrange. Applying the QC criteria flags 75 % of the available data, spanning September 2011–June 2014. Thus, for the 85 % of this period that either has instrument downtime or where the data are QC flagged, an alternative approach is used.

Due to the limited data set available from the EC method, a bulk aerodynamic method is also used in order to fill in data gaps for the time period June 2011–June 2014. The bulk transfer method

uses Monin–Obukhov similarity theory to estimate turbulent sensible heat flux at the surface:

$$\mathrm{SH} = \rho c_\mathrm{p} C_\mathrm{h} U \left(T_\mathrm{surf} - T_{2\,\mathrm{m}}\right), \tag{3.5}$$

where U is the mean horizontal wind speed at 2 m, T_surf is the skin temperature, $T_{2\,\mathrm{m}}$ is the temperature at 2 m, and C_h is the sensible heat transfer coefficient for the 2 m reference height (Persson et al., 2002; Fairall et al., 1996). NOAA/GMD meteorological data are the primary source of the 2 m temperature measurements and data gaps are filled with CIBS temperature data. Cup anemometer measurements fill in data gaps of the sonic anemometer-derived 2 m wind speed measurements. C_h is based on the roughness of the surface and assumes scalar velocity and temperature roughness lengths with corrections to account for boundary-layer stability. An optimal (as compared to the EC measurements) velocity roughness length of 3.8×10^{-4} m (Kuipers Munneke et al., 2009) and a roughness length for temperature of 1×10^{-4} m (Andreas et al., 2005) are assumed constant in time. Separate stability correction functions for stable or unstable boundary-layer conditions are used to iteratively converge on the best-estimate sensible heat flux (Persson et al., 2002).

Comparing the bulk sensible heat flux to the quality-controlled EC data gives an indication of the uncertainty in the bulk method. Bulk data are deemed valid when the surface friction velocity ($u_* = [-\overline{u'w'}]^{0.5}$) value exceeds $0.03\,m\,s^{-1}$. A correlation coefficient of 0.89 exists between the two techniques for the subset of data deemed valid for both techniques. The RMS difference between the two methods ($8.7\,W\,m^{-2}$) is the net estimated uncertainty in the sensible heat flux. Compared to the EC data the bulk method has a bias of $+7.0\,W\,m^{-2}$. For instances where the bulk sensible heat flux magnitude is less than $10\,W\,m^{-2}$ the bias and RMS difference decrease to +3.5 and $2.60\,W\,m^{-2}$, respectively. This improvement suggests some of the differences could be due to inaccurate stability correction functions, uncertainty in the surface temperature derived from LW measurements and snow emissivity assumptions, or roughness length values. Sensible heat flux discrepancies could also be due to measurement height differences between the EC and bulk methods. While the bulk method uses the measured surface skin temperature the EC values are

measured at 2 m, which could differ from the sensible heat flux directly at the surface under very stable conditions. This suggests that the true SH uncertainty is smaller than estimated here. The covariance u_* and bulk u_* are well correlated (0.84) with a RMS difference of $0.55\,m\,s^{-1}$ and the bulk values are biased low ($-0.026\,m\,s^{-1}$). Changing the velocity roughness length to 4.5×10^{-4} m, which was determined for snow-covered multi-year sea ice (i.e., Persson et al., 2002), increases the RMS differences for the sensible heat flux by $1.4\,W\,m^{-2}$, suggesting that variability in the roughness of the surface could contribute to error in the bulk parameterization. A majority of the $8.7\,W\,m^{-2}$ uncertainty in the bulk estimates is likely due to uncertainties in the skin temperature as estimated from a constant surface emissivity. From June 2011 to June 2014 the bulk estimates are available for 78 % of the time period. Thus, filling in EC data gaps with the bulk values vastly improves the temporal coverage of the sensible heat estimates.

3.2.4 Turbulent latent heat flux and stability

Turbulent eddies also affect the surface energy budget by transferring latent heat toward or away from the surface. Frequently the specific humidity increases with height above the surface, resulting in a transfer of latent energy toward the surface possibly resulting in deposition. The bulk method used by Persson et al. (2002) assumes saturation conditions at the surface, which is not always a valid assumption for dry snow (Albert and McGilvary, 1992). In central Greenland the two-level profile method has been shown to be superior to the bulk method (Box and Steffen, 2001) as it can account for sublimation and deposition to the surface.

The profile method used here is similar to Steffen and DeMaria (1996) such that the latent heat flux is calculated from near-surface horizontal wind (U) and mixing ratio (q) gradients ($\Delta =$ value at 10 m $-$ value at 2 m) according to the following equation:

$$\mathrm{LH} = \rho L_\mathrm{v} k^2 z_\mathrm{r}^2 \left(\frac{\Delta U}{\Delta z}\frac{\Delta q}{\Delta z}\right)(\phi_\mathrm{m}\phi_\mathrm{e})^{-1}\,, \tag{3.6}$$

where ρ is the density of air, L_v is the latent heat of vaporization, k is the von Kármán constant (0.4), and z_r is the log mean height ($\frac{\Delta z}{\ln(z_2 z_1{}^{-1})}$). The stability functions for the transfer of momentum

Table 3.3: Stability functions for unstable and stable regimes from Cullen (2003).

Stability function	Unstable ($Ri < 0$)	Stable ($0 < Ri < 0.25$)
ϕ_{m}	$(1 + 27\lvert Ri\rvert)^{-0.2}$	$\left(1 + \frac{4Ri}{1-4Ri}\right)$
ϕ_{e}	$(1 + 19\lvert Ri\rvert)^{-0.55}$	$\left(1 + \frac{3Ri}{1-4Ri}\right)$

(ϕ_{m}) and water vapor (ϕ_{e}) are corrections based upon the stability of the boundary layer and will either increase (unstable conditions) or decrease (stable conditions) the surface flux.

A measure of boundary-layer stability is attained via calculation of the bulk Richardson number (Ri). The sign of Ri indicates whether mechanical mixing (positive) or buoyancy (negative) is more important in producing turbulence. Ri is dependent on the gradient in virtual potential temperature ($\Delta\theta_v$), wind speed (Δu), and respective measurement heights (Δz) according to the following equation:

$$Ri = \frac{g}{\overline{\theta_v}} \frac{\Delta\theta_v \Delta z^{-1}}{(\Delta u \Delta z^{-1})^2}, \tag{3.7}$$

where g is the acceleration due to gravity ($9.81\, m\, s^{-2}$) and $\overline{\theta_{\mathrm{v}}}$ is the average virtual temperature (K) between the two levels. In accordance with Steffen and DeMaria (1996), Ri is used to calculate the stability corrections. Coefficients for relating Ri to the stability factors are obtained from a study conducted in 2000, which used EC turbulence measurements to obtain the relationships in Table 3.3 (Cullen, 2003). For stable Ri values greater than zero the stability functions act to reduce the magnitude of the latent heat flux. For Ri greater than the critical Richardson number ($Ri = 0.25$) vertical turbulence becomes small and, in theory, results in laminar flow. Grachev et al. (2013) indicate that intermittent and nonstationary turbulence can exist even in this super-critical regime. Assuming LH = 0 for $Ri > 0.25$ could underestimate latent heat flux from intermittent nonstationary turbulence but isotopic closure calculations indicate that for very stable boundary layers tracers are conserved, suggesting little to no net water vapor exchange at the surface (Berkelhammer et al., 2016). Thus, for Ri measurements which fall into the super-critical regime, 44 % out of the 33 090 total measurements from March 2012 to June 2014, the latent heat fluxes are set to zero, providing

a reminder of the significance of high stability in limiting mass transfer.

LH is the data set most susceptible to data gaps because there must be input values of specific humidity, wind speed, and temperature at both the 2 and 10 m levels. Yet by using the best available meteorological data from NOAA/GMD and/or the CIBS project we estimate LH for 81 % of the time period from March 2012 to June 2014. The main driver of uncertainty is the estimation of the mixing ratios with uncertainties of 53 and 30 % at 2 and 10 m, respectively, as compared to the Picarro measurements. The resultant error contribution (60 %) to the LH estimate dominates the contribution from uncertainty in the wind speeds.

3.2.5 Subsurface heat flux

The energy flux from the overlying atmosphere to the subsurface includes direct radiative heating of the snowpack due to solar penetration (Kuipers Munneke et al., 2009), the thermal effects of wind ventilation (Albert and McGilvary, 1992), and conduction. To minimize the complications in calculating subsurface heat flux caused by the other factors, an estimation of the conductive heat flux (C) at a depth below the solar penetration depth (at least 20 cm) combined with a heat storage (S) in the snow above this level is used to provide an estimation of the total subsurface heat flux (G), such that

$$G = C + S. \tag{3.8}$$

In this study we calculate the storage heat flux across the uppermost layer and assume the heat flux to the subsurface below is equivalent to C.

The conductive heat flux (C) represents the diffusion of heat between the subsurface and the overlying surface. The effectiveness of the heat transfer is a function of the thermal conductivity of the snow (K) and the vertical temperature gradient ($\Delta T/\Delta z$):

$$C = -K\frac{\Delta T}{\Delta z}. \tag{3.9}$$

The temperature gradient for the uppermost subsurface layer (ΔT_{01}) is estimated as the difference between the surface temperature (T_{surf}, Eq. 3.3) and the temperature measured by the shallowest,

subsurface sensor. To estimate C, at $\approx 20\,\mathrm{cm}$ depth, the conductive heat flux at the two levels bracketing this depth is calculated and averaged, according to the following equation:

$$C = -\frac{1}{2}\left(K_{01}\frac{\Delta T_{01}}{\Delta z_{01}} + K_{12}\frac{\Delta T_{12}}{\Delta z_{12}}\right). \tag{3.10}$$

The thermal conductivity of the upper most layers of snow is estimated from average density profile measurements taken from five snow pits around Summit Station in July 2014. The average standard deviation of density among pits at all depths is $50\,kg\,m^{-3}$. There is a known annual cycle in snow density in this region based on seasonally varying thermal and snow properties (Albert and Shultz, 2002). The first two density minima with increasing depth are assumed to be different solely due to compaction of the snow over the course of a year, resulting in a linear compaction factor of $-22\,kg\,m^{-3}\,year^{-1}$. This factor is used to estimate the annual evolution of near-surface snow density as a function of time from the profile measurements collected July 2014. The adjusted density profile is used to determine an average snow layer density for the representative near-surface conditions from July 2013 to June 2014. The result is a range of density values varying annually between 348 and $413\,kg\,m^{-3}$. Snow density is converted to thermal conductivity according to Jordan (1991), resulting in a seasonally varying thermal conductivity with an average value of $0.47\,W\,m^{-1}\,K^{-1}$. The average value is higher than summer sea-ice values (Sturm et al., 1997; Persson et al., 2002) of $0.3\,W\,m^{-1}\,K^{-1}$, although the summer minimum conductivity ($0.39\,W\,m^{-1}\,K^{-1}$) is more similar to the sea-ice values.

The uncertainty in the conductive flux is related to the uncertainties in the calculated skin temperature, subsurface temperature, subsurface measurement height, and snow conductivity estimate. The LW-derived skin temperature uncertainty is approximately 0.6 K. The thermistor accuracy specifications indicate an interchangeability tolerance of 0.38 K at 0 °C and 0.6 K at −40 °C. We estimate the uncertainty in the measurement height of the shallowest thermistor as 2 cm. A $50\,kg\,m^{-3}$ uncertainty in the snow density translates to $0.1\,W\,m^{-1}\,K^{-1}$ uncertainty in snow conductivity. The average temperature difference between the surface and −40 cm is about 7.2 °C. The resultant uncertainty in the conductive flux, calculated by taking the quadrature sum of the

fractional uncertainties, is 26 %.

The storage of heat in a layer is related to the time rate of temperature change averaged over that layer. The storage heat flux (S) includes energy associated with solar heating, longwave emission, and turbulent heat flux within the snow. In the uppermost layer ($\approx 20\,\mathrm{cm}$), S is calculated by the layer averaged temperature difference (δT) between chronologically adjacent time steps ($\delta t = 30\,\mathrm{min}$), where T_1 is the temperature of the shallowest thermistor at a depth z_1 (similar to Hoch, 2005):

$$S = -c_{\mathrm{ice}}\rho\left[\frac{\delta T_{\mathrm{surf}} + \delta T_1}{2\delta t}\right](-z_1)\,, \tag{3.11}$$

where c_{ice} is the specific heat of ice and ρ is the average density of the layer. The large uncertainty in the skin temperature measurements (0.6 °C) are close to the average temperature change from one time step to the next (0.76 °C), resulting in an estimated uncertainty in S of 80 %. The estimate of S is the most uncertain term in the SEB.

3.2.6 Cloud properties and precipitable water vapor

Investigating the surface flux estimates in combination with active and passive cloud property measurements yields a comprehensive understanding of how clouds affect the GIS energy budget. In addition to the aforementioned radiosondes, ICECAPS also measures the cloud properties via a comprehensive suite of instruments, in operation since May 2010. ICECAPS is described in detail by Shupe et al. (2013b). Liquid water path (LWP) and precipitable water vapor (PWV) are estimated using a physical retrieval via a pair of microwave radiometers (MWR), similar to Turner et al. (2007a). In a dry environment, such as Summit, it is advantageous to use a total of three channels (23.84, 31.40, 90.0 GHz) to increase sensitivity and effectively reduce uncertainty in LWP ($\approx 5\,g\,m^{-2}$) and PWV ($\approx 0.35\,\mathrm{mm}$) (Crewell and Löhnert, 2003). The primary changes to the LWP values estimated in Miller et al. (2015) are an improved liquid water model (TKC; Turner et al., 2016) and the use of three channels in the retrieval instead of four. By excluding the 150.0 GHz channel, biases in LWP retrievals due to precipitating ice hydrometers will not impact the overall

statistical results (Pettersen et al., 2016). The liquid present cloud fraction for a given month is the number of LWP samples greater than $5\,g\,m^{-2}$ divided by the total number of samples. During May and June 2014 the microwave radiometer measuring 23.84 and 31.40 GHz was off site for repairs and thus LWP and PWV are unavailable for these months. A 35 GHz millimeter cloud radar (MMCR) determines vertically resolved cloud presence. Monthly cloud fractions are calculated using a MMCR detection threshold of −60 dBz, retaining sensitivity to most hydrometeors.

3.3 Results

Observationally based results capture atmospheric–ice sheet interactions. This section will first examine temperature profiles at Summit, providing a foundational understanding for how the atmosphere and snowpack are related. Secondly, investigation of the partitioning of surface energy flux over the annual and diurnal cycles illuminates when various SEB terms are most influential. Finally, quantifying the response of the SEB to changes in the downwelling radiation, predominately affected by cloud presence and insolation, shows how the non-radiative SEB terms effect the surface temperature variability.

3.3.1 Temperature profiles

The temperature variability at and below the ice sheet surface is important for understanding the flow of heat through this interface and can influence processes such as snow compaction and melt. Figure 3.1 depicts the variability in temperature above, below, and at the surface from 1 July 2013 to 30 June 2014. The maximum surface temperature (T_{surf}) was −3.1 °C on 10 July 2013 and the minimum was −68.8 °C on 23 March 2014 (Fig. 3.1a). A warm or cold pulse at the surface propagates to deeper portions of the GIS over time and can take days to influence the temperatures at 1–2 m depth. In general, the slope of a pulse is about 10 cm of penetration per day.

In the spring, fall, and winter, surface-based temperature inversions are prevalent (Miller et al., 2013) and the warmest layers of the atmosphere occur between 100 and 1000 m a.g.l. as can be seen in Fig. 3.1a. In fact, the minimum temperature in the near-surface layer (−2 to 20 m) occurs

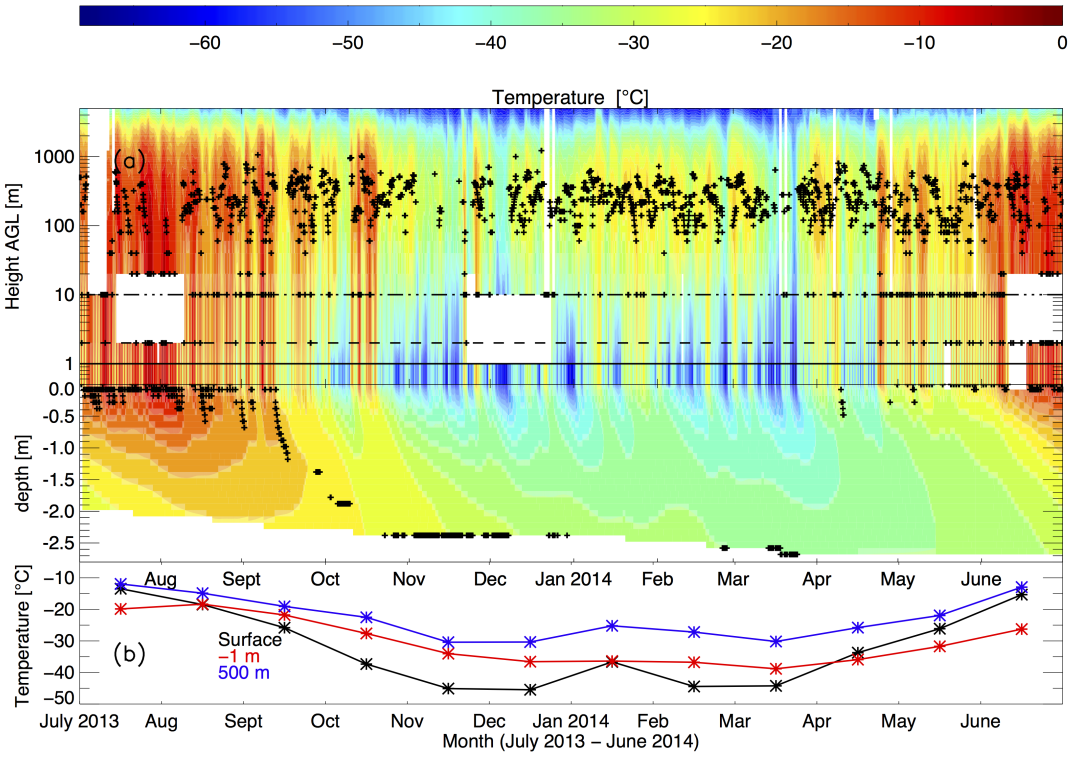

Figure 3.1: Temperature evolution from 1 July 2013 to 30 June 2014. **(a)** Values between the solid horizontal lines indicate surface temperatures (T_{surf}). The dashed (dashed-dotted) line at 2 m (10 m) level is NOAA/GMD measurements, and that from 20 m to 5 km a.g.l. is derived from twice-daily radiosoundings. The height scale above ground level is logarithmic to emphasize the near-surface values where the atmospheric and GIS are physically coupled. Subsurface temperatures are on a linear scale. White areas indicate periods of data gaps and black symbols indicate the height of the maximum temperature in each profile. (b) Monthly mean temperatures at 500 m, T_{surf}, and −1 m.

at the surface 46 % of the year. At times the subsurface is the warmest level in the full temperature profiles (−2 m to 5 km) shown in Fig. 3.1a. The average monthly surface temperature is colder than the average 500 and −1 m temperatures from September to April (Fig. 3.1b), although January 2014 had anomalously warm (compared to Januaries 2011–2013) surface temperatures. The maximum temperature in the near-surface layer occurs at the surface only 3.4 % of the year, indicating that the default state of the system is strong surface cooling to space.

Advection of air masses over the GIS is the foundational mechanism that influences temperatures at the surface. Temperature changes at 1–5 km a.g.l. are indicative of synoptic influences that transport warmer or colder air masses to Summit. During 10 January 2014 (Fig. 3.1a) warmer air advection corresponds to relatively warm surface temperatures of −25 °C. Yet there are instances, such as 15 January–4 February 2014, with large variability in T_{surf} that are not associated with large-scale advection, as evidenced by fairly constant temperatures from 50 m to 5 km in altitude. The correlation between the temperatures at 5 km and the surface is 0.77 and from 1 to 2 km the correlation with surface temperature increases to 0.87. Seasonal synoptic variations in the free troposphere above ≈ 1 km influences surface temperatures, especially when the downwelling longwave emission originates from the warmest levels of the atmosphere. Synoptically driven warm air advection enhances the formation of optically thick liquid-bearing clouds, which decrease the difference in emitted longwave radiation between the air aloft and the surface.

3.3.2 Surface energy budget

3.3.2.1 Annual cycle

Monthly averages of the four SEB terms from Eq. (3.1) illustrate the seasonal balance of energy fluxes at the surface (Fig. 3.2). The bottom numbers in Fig. 3.2 indicate the percentage of the month for which all four SEB terms are available. In addition, Fig. 3.2 includes additional data for Q, SH, and LH indicating that July 2013–June 2014 is, in general, consistent with previous years and indicates that January 2014 was somewhat anomalous. The extended data periods for

Q, SH, and LH all end June 2014 and include start dates of January 2011, June 2011, and March 2012, respectively.

The sensible and radiative heat fluxes have nearly compensating influences on the SEB during the non-summer months when temperature inversions are prevalent. During the summer, on average, all SEB terms are relatively small in magnitude. The monthly mean total radiative flux (Q) is positive in June and July (Fig. 3.2). Only these two months correspond to periods when the amount of absorbed SW exceeds the net LW radiational cooling. June and July are also when the sensible and latent heat fluxes are at their seasonal minima. The subsurface heat flux monthly minimum values occur a month earlier in the year, due to the cooler subsurface temperatures in the spring compared to the fall (Fig. 3.1). Colder subsurface temperatures enhance the ability of the GIS to remove heat from the surface via conduction, resulting in a mean cooling effect in the spring and warming effect in the fall.

Over the entire year the SEB residual, or the sum of all the SEB terms, when available (75.3 % of the time), is $0.9\,W\,m^{-2}$. The monthly residuals (top numbers in Fig. 3.2) indicate that there are times of the year when the residuals are larger but there is no apparent seasonality in the combined SEB terms. Generally, the monthly mean residuals could be due to energy imbalances, under sampling, measurement biases, and/or measurement uncertainties. Each monthly residual is below the total SEB uncertainty (excluding the S term) of $12.4\,W\,m^{-2}$.

3.3.2.2 Diurnal cycles

The magnitudes of the monthly mean SEB terms are small from May to August ($< 10\,W\,m^{-2}$), yet the diurnal variability peaks during this period, driven largely by the solar cycle. The net radiative flux increases during times of peak insolation (Fig. 3.3a), although the high surface albedo limits the maximum Q to $40\,W\,m^{-2}$. The maximum values of the net radiative flux occur in July, when the sun still rises more than 30° above the horizon and liquid-bearing clouds are frequent (Fig. 3.4a, b), which act to radiatively warm the surface at Summit Station year round (Miller et al., 2015).

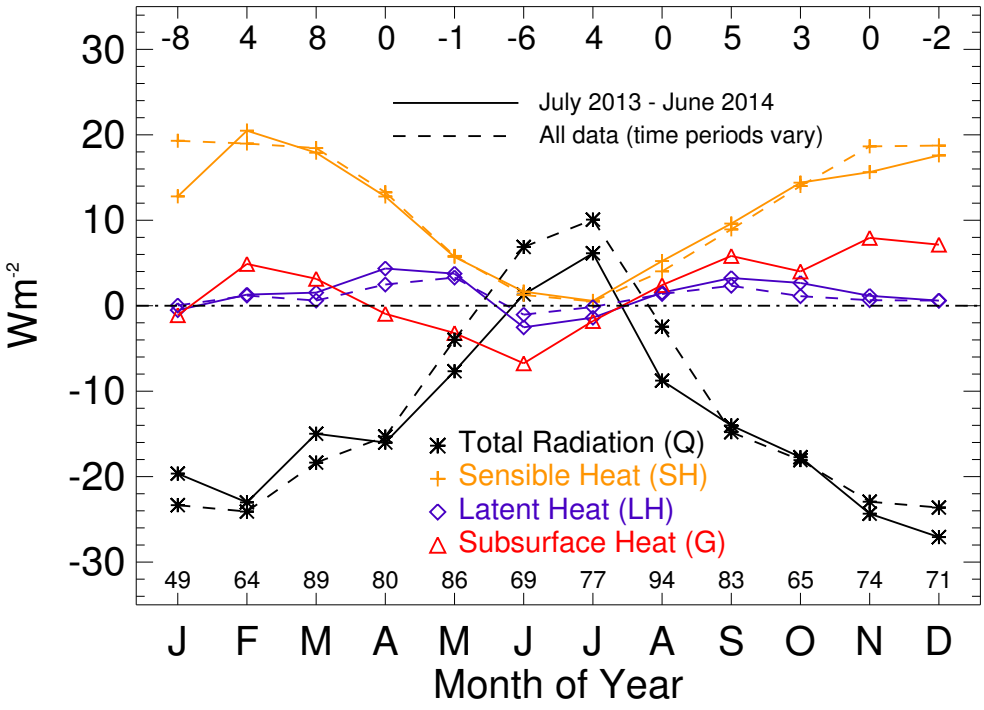

Figure 3.2: Monthly mean values of the four SEB terms for the period July 2013–June 2014. The values at the top of the figure are the monthly residual of the SEB ($W\,m^{-2}$). The values at the bottom of the figure are the percentage of the month for which all four SEB terms are available.

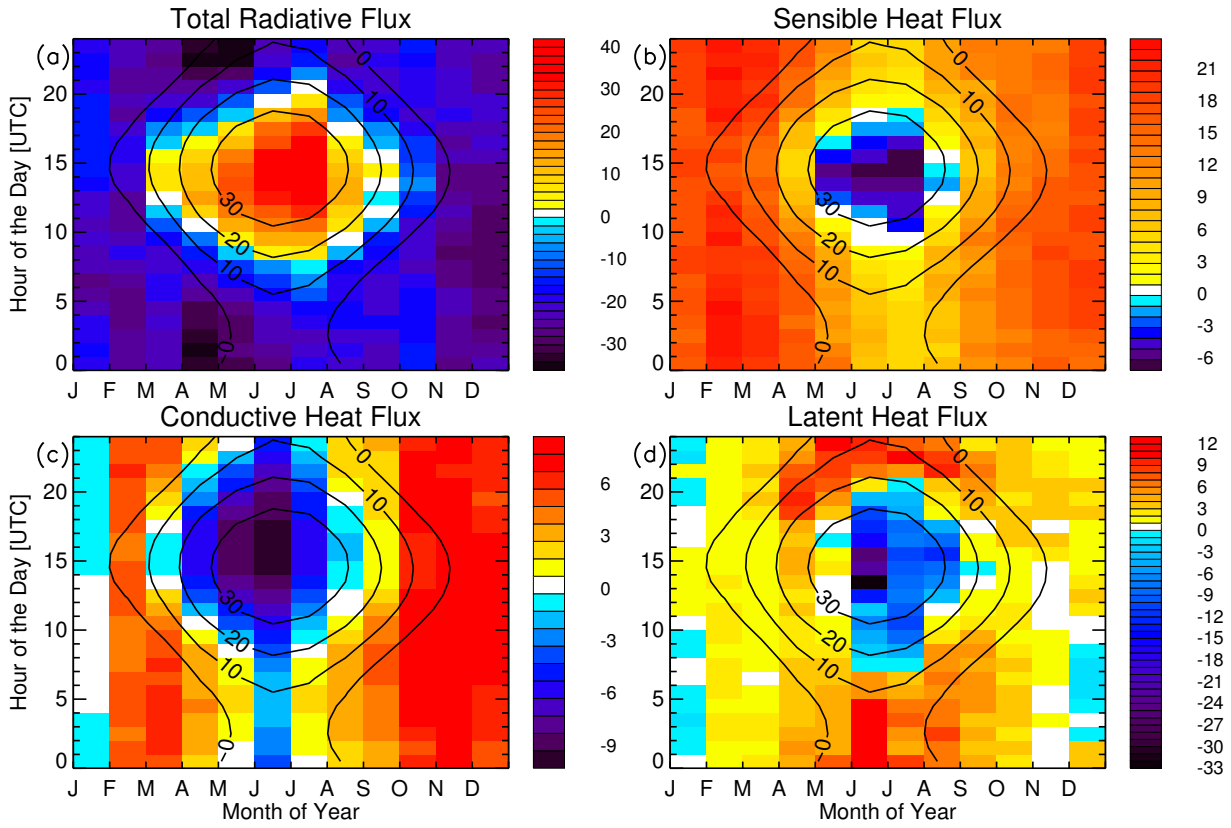

Figure 3.3: Monthly–hourly mean values from July 2013 to June 2014 of **(a)** total radiative flux, **(b)** sensible heat flux, **(c)** conductive heat flux, and **(d)** latent heat flux. Black contour lines indicate the solar elevation angle. Units on the color bars are all in $W\,m^{-2}$.

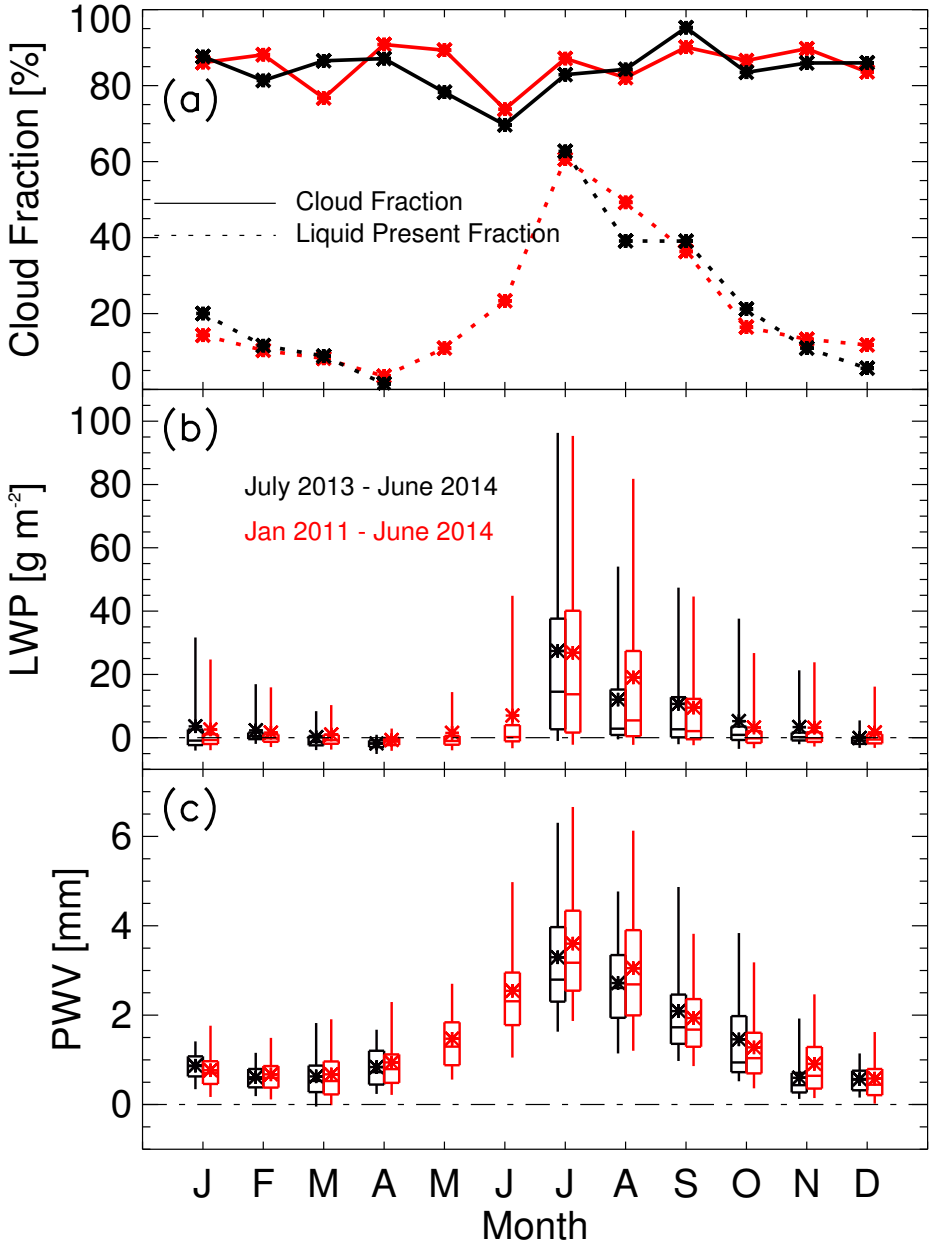

Figure 3.4: **(a)** MMCR derived cloud fraction (solid) and MWR derived liquid present fraction (dotted, LWP $> 5\,g\,m^{-2}$), **(b)** liquid water path, and **(c)** precipitable water vapor. Statistics shown in black (red) are for available data spanning July 2013–June 2014 (January 2011–June 2014). Distributions are represented by box-and-whisker plots (the box indicates the 25th and 75th percentiles, the whiskers indicate 5th and 95th percentiles, the middle line is the median, and the * is the mean).

Counteracting the net radiative flux, the sensible heat flux is negative for large sun angles and warms the surface by approximately $20\,W\,m^{-2}$ when the sun is below the horizon (Fig. 3.3b). The diurnal variability for this term is largest in summer due to an enhanced diurnal cycle of the near-surface temperature gradient (Miller et al., 2013). The cooling effect of the conductive heat flux (Fig. 3.3c) is most prominent when the sun is above the horizon and is maximized at solar noon. In agreement with the results in Fig. 3.2, more conductive surface cooling occurs in the spring compared to the fall due to the lag in subsurface response, which results in relatively colder subsurface temperatures in the spring. The diurnal variability of the latent heat flux is largest in June ranging from hourly average values of -33 to $12\,W\,m^{-2}$ (Fig. 3.3d) due to an increase in available moisture (Fig. 3.4c).

Sun angle, and the associated change to the net radiative flux, is a main driver of energy fluxes at the surface (Fig. 3.3). The monthly–hourly energy fluxes in Fig. 3.3b–d are generally anti-correlated with the net radiative flux in Fig. 3.3a (correlation coefficients are $b = -0.81$, $c = -0.65$, $d = -0.69$). The following case studies investigate how liquid-bearing clouds effect the surface energy budget by increasing the net surface radiation.

3.3.3 Cloud forcing case studies

3.3.3.1 Liquid-bearing cloud without insolation

A case study (12 UTC 10 November to 12 UTC 11 November 2013) is used to illustrate how the different terms of the SEB interact to influence the surface temperature and surface heat exchange. Variability in this case is driven by low-level liquid-bearing clouds and the case was intentionally chosen to minimize the effects of solar influences. Cloud occurrence as measured by the MMCR up to a height of 5 km (Fig. 3.5a) indicates a clear-sky scene at the beginning of the case study, a low-level cloud from 17 to 2 UTC, then a brief period of clear-sky from 2 to 3 UTC, and finally a deep cloud (> 3 km) during the end of the case study. The radar reflectivity measurements indicate the presence of ice crystals in most of these clouds. LWP values ranging from 20 to $60\,g\,m^{-2}$ from

17 to 24 UTC on 10 November (Fig. 3.5b) show that the low-level cloud at this time is mixed phase, in contrast to the deep ice cloud at the end of the case study with little liquid present.

Coincident with the appearance of the liquid-bearing cloud, the LW↓ increased by $88\,W\,m^{-2}$ from 15 UTC (clear) to 23 UTC (cloudy), similar to the LW CRF value in Miller et al. (2015) for optically thick liquid-bearing clouds ($\approx 85\,W\,m^{-2}$). This cloud radiative effect resulted in an increase in T_{surf} and thus LW↑ of $43\,W\,m^{-2}$ (Fig. 3.5c). During the clear-sky period the boundary layer was weakly stable ($Ri = 0.15$), but the occurrence of the liquid-bearing cloud and its warming effect on the surface changed the stability to neutral ($Ri \approx 0$) (Fig. 3.5d). During the transition back to clear-sky (2 UTC), LW↓ decreased by about $70\,W\,m^{-2}$ and the Richardson number became critically stable. LW↓ was smaller in the presence of the deep ice cloud, compared to the liquid-bearing cloud, resulting in a much smaller LW↑ at the time. In the presence of the deep ice cloud the boundary layer became weakly stable again ($Ri = 0.2$).

Changes to the net radiative flux caused by the cloud (Fig. 3.5e) elicited a response in the other SEB terms. On 10 November from 15 UTC to 23 UTC the sensible heat flux decreased by a factor of 2, from 36 to $18\,W\,m^{-2}$. The conductive heat flux changed from having a warming effect on the surface by $+8.1\,W\,m^{-2}$ to having a $-0.3\,W\,m^{-2}$ cooling effect by 23 UTC. The average latent heat flux increased from $0.8\,W\,m^{-2}$ during the clear-sky period (12–18 UTC) to an average value of $2.4\,W\,m^{-2}$ during the cloudy period (18–24). The net result is that the liquid-bearing cloud increased the surface temperature from $-47.8\,°C$ (15 UTC) to $-33.0\,°C$ (23 UTC). This is half the temperature increase that would have occurred ($\approx 28.4\,°C$) if the entire LW↓ increase ($88\,W\,m^{-2}$) had gone toward heating the surface. This example demonstrates how changes to the turbulent and conductive heat fluxes are an important compensation mechanism that modulates surface warming due to CRF. This damping effect on the radiative forcing by the response terms was noted by previous Arctic researchers (e.g., Persson, 2012; Sterk et al., 2013; Solomon et al., 2017).

The subsurface cooled in response to the surface cooling during the clear-sky period on 10 November (Fig. 3.5f), yet the minimum measured temperature at $-0.2\,m$ ($-41.8\,°C$) was not realized until 18 UTC. This shallowest subsurface temperature sensor ($-0.2\,m$) cooled by $0.8\,°C$ from

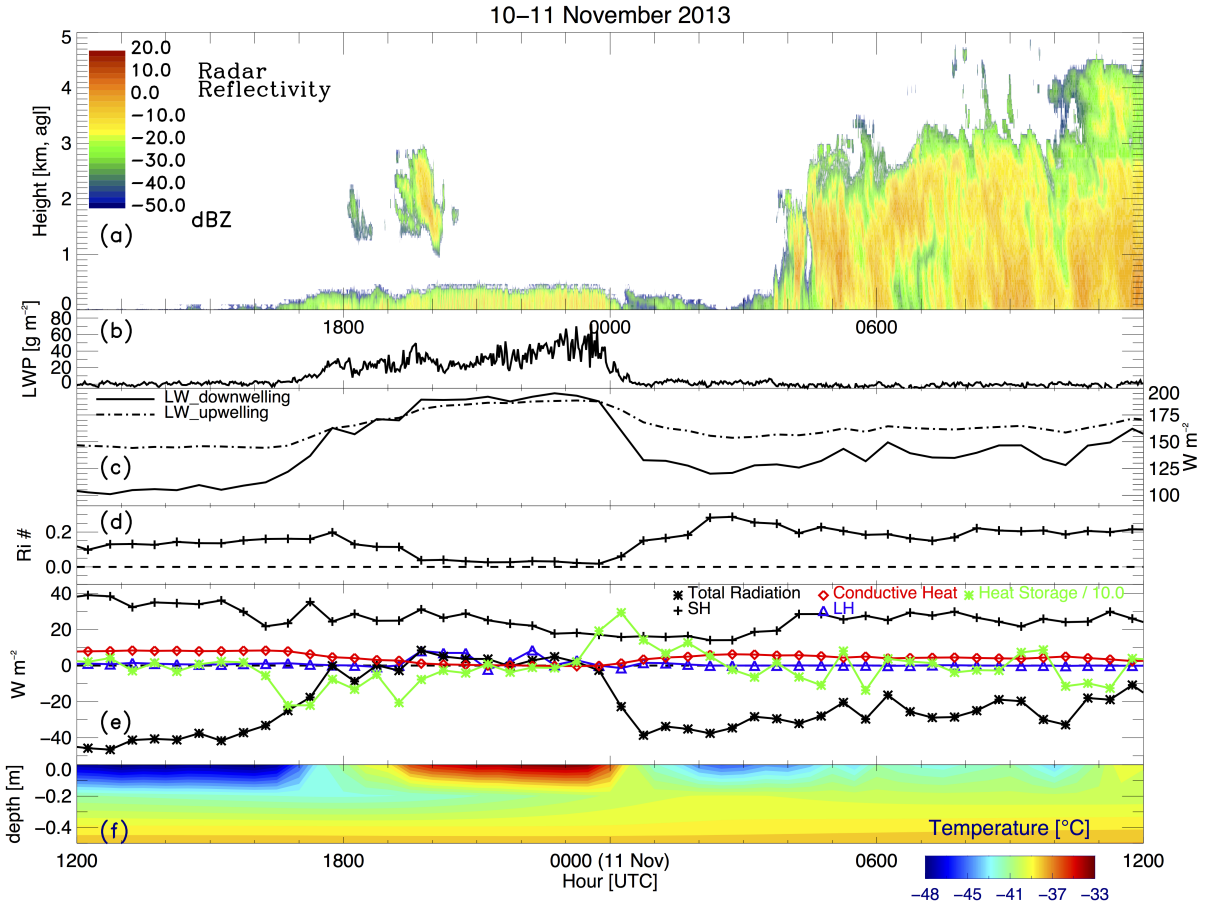

Figure 3.5: A case study from 12 UTC on 10 November 2013 to 12 UTC on 11 November 2013. **(a)** Cloud occurrence as seen by the MMCR; **(b)** liquid water path; **(c)** longwave upwelling and downwelling radiation; **(d)** Richardson number; **(e)** surface energy fluxes: total radiation, sensible heat, latent heat, conductive heat, and heat storage/10.0; and **(f)** subsurface temperatures.

12 to 18 UTC on 10 November. The cooling from above at −0.2 m on 10 November was damped by the relatively warm snowpack below. During the liquid-bearing cloud period the subsurface layer at −0.2 m was warmed from above and below allowing for a 1.8 °C temperature increase from 18 UTC on 10 November to 2.5 UTC on 11 November. This suggests that a time lag of the effect of the surface temperature on the subsurface temperatures is important in determining the ground heat flux. The heat storage in the upper layer of snow had an average value of $-12.9\,W\,m^{-2}$ for the 24 h period shown in Fig. 3.5e, indicating that a portion of the increase in LW↓ went toward increasing the internal energy of the top layer of snow. Large negative values of S occur during the transition from clear to the onset of the liquid-bearing cloud presence (17–20 UTC), as this layer warms rapidly, and vice-versa during the transition back to a clear-sky scene (0–2 UTC).

3.3.3.2 Liquid-bearing cloud with insolation

A case study on 6 August 2013 also illustrates the longwave warming effect of liquid-bearing clouds and investigates the additional influence of shortwave radiation. Similar to the first case study, surface temperature variability is driven by the downwelling radiative flux, which in this case is a combination of longwave and shortwave influences.

MMCR measurements (Fig. 3.6a) indicate a clear-sky scene from 2 to 6 UTC, a low-level cloud from 6 to 13.5 UTC, clear-sky from 13.5 to 16 UTC, a deep cloud from 18 to 22 UTC, and finally a low-level cloud during the last hour of the case study period. The low-level cloud is mixed phase from 6 to 13.5 UTC and LWP values ranging from 0 to $15\,g\,m^{-2}$ (Fig. 3.6b) indicate that it is optically thin. LWP values ranging from 0 to $20\,g\,m^{-2}$ also indicate that the deep cloud later in the day is mixed phase from 18 to 21 UTC, although after ≈19 UTC LWP values are low due to competition from falling ice into the mixed phase layer from above. The low-level cloud from 23 to 24 UTC is optically thicker then the previous low-level cloud with LWP ranging from 5 to $30\,g\,m^{-2}$.

The presence of the optically thin liquid-bearing cloud (6–13.5 UTC) produces an approximate increase of $70\,W\,m^{-2}$ of LW↓ compared to the preceding clear-sky scene. Over this period shortwave

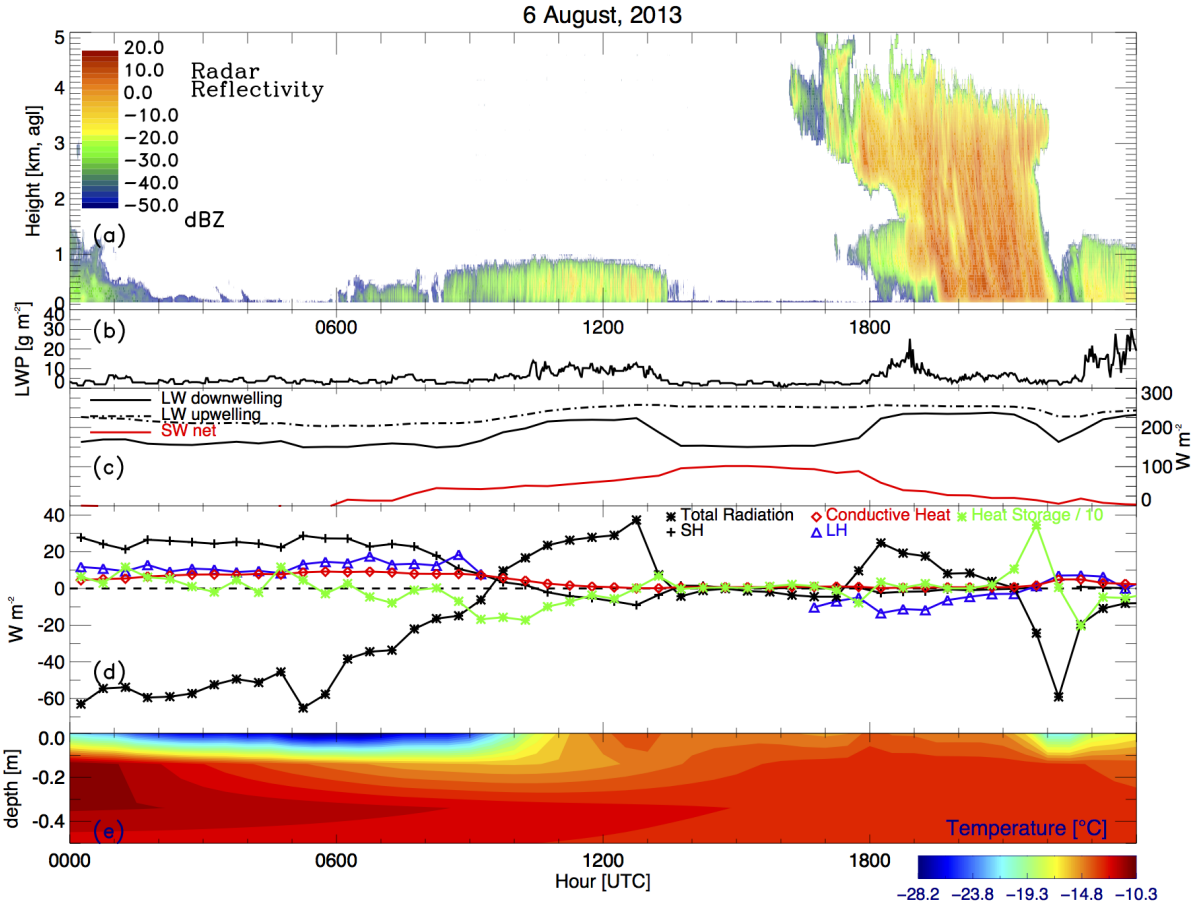

Figure 3.6: A case study on 6 August. **(a)** Cloud occurrence as seen by the MMCR; **(b)** liquid water path; **(c)** longwave upwelling, longwave downwelling, and net shortwave radiation; **(d)** surface energy fluxes: total radiation, sensible heat, conductive heat, and heat storage/10.0; and **(e)** subsurface temperatures.

radiation increases the net radiation at the surface by an additional 5–75 $W\,m^{-2}$. In response, LW↑ radiation increases by 50 $W\,m^{-2}$. The combination of thin liquid-bearing clouds and insolation produces positive net radiation at the surface from 9.5 to 13 UTC (Fig. 3.6c). During the daytime clear-sky period the net radiation is near zero, indicating that shortwave warming is offset by the longwave cooling at the surface. Net radiation again goes positive in the presence of liquid-bearing clouds that occur after 18 UTC. After 18 UTC the net radiation declines as the solar radiation diminishes.

The compensating response of the non-radiative terms to changes in the downwelling radiation, shortwave and/or longwave, is similar to the November case study. The sensible heat flux decreases from 29 $W\,m^{-2}$ at 5 UTC to −9 at 12.5 UTC (Fig. 3.6d). The fact that the SH is negative during the presence of the liquid-bearing cloud indicates that the surface temperature is warmer than the 2 m temperature; thus the near-surface atmospheric layer is unstable. The conductive heat flux decreases from 9 $W\,m^{-2}$ at 5 UTC to 0 $W\,m^{-2}$ at 12.5 UTC, indicating the subsurface temperature gradient as been reduced (Fig. 3.6e). The 10 m temperatures from 9 to 16 UTC are questionable and thus LH is not shown during this period. During the daytime clear-sky period (13.5–16 UTC) the net radiation is near zero as is the ground heat flux and sensible heat flux. In the presence of the deep mixed-phase cloud after solar noon the net radiation again is positive, the sensible and ground heat flux are near zero, and the latent heat flux is approximately −10 $W\,m^{-2}$. Section 3.3.4 expands the analysis to include annual responses of the LW↑, latent, sensible, and conductive heat flux terms to changes in LW↓ + net SW.

3.3.4 Responses to surface radiative forcing

The surface energy budget at Summit Station is largely driven by changes in the downwelling radiation. In general, the LW↑, turbulent, latent, and subsurface heat fluxes (response terms) respond to changes in the LW↓ and net SW flux (forcing terms). The response terms are not always governed by the forcing terms, as, for instance, under high wind conditions the turbulent heat fluxes can operate independently as the Ri in these cases is dominated by the wind shear

(see Eq. 3.7). Cloud presence influences the radiational balance at the surface by modulating the downwelling radiation; increasing LW↓ and decreasing SW↓. Miller et al. (2015) show that clouds increase the net surface radiation compared to an equivalent clear-sky scene, because the high year-round surface albedo limits the magnitude of the cloud SW cooling effect to less than that of the LW warming effect. Statistical relationships for the current study reinforce the fact that liquid-bearing clouds increase the forcing terms during two distinct periods: with and without solar insolation (Fig. 3.7a). Hence, the occurrence of liquid-bearing clouds correspond to warmer surface temperatures in both circumstances (Fig. 3.7b) and consequently greater LW↑ (Fig. 3.7c), which is proportional to the surface temperature to the fourth power. In addition, variability in surface albedo acts as a forcing, although at Summit the magnitude of downwelling radiation variations are much greater than the effect of albedo variations on forcing terms.

LW↑ has less variability (all cases in Fig. 3.7c) than the variability of the forcing terms (all cases in Fig. 3.7a). In addition, the differences between the cloudy and non-cloudy states are more pronounced in Fig. 3.7a, compared to Fig. 3.7c. Thus, compensation by the non-radiative SEB terms must account for imbalances to the radiative flux at the surface, as illustrated in the case studies presented in Sect. 3.3.3 and in Figs. 3.2 and 3.3. The annual cycle of the responses of LH, SH, G, and LW↑ are explored in Sect. 3.3.4.2 after investigating the effect of liquid-bearing clouds and/or sun angle on boundary-layer stability (Sect. 3.3.4.1).

3.3.4.1 Boundary-layer stability response

The degree to which the overlying atmosphere can dynamically interact with the surface is important for determining the turbulent heat exchange. Atmosphere–ice sheet interaction is modulated by low-level stability, which can be influenced by both thermodynamic and dynamic processes. Mechanical mixing, via high wind speeds, is one way to decrease near-surface stability and increase turbulence near the surface. The 10 m wind speed is greater than $8\,m\,s^{-1}$ for 16 % of 32 130 stability estimates. The median Richardson number decreases from 0.19 for all cases to 0.06 for the cases that report higher wind speeds ($>8\,m\,s^{-1}$), showing the expected decreases of

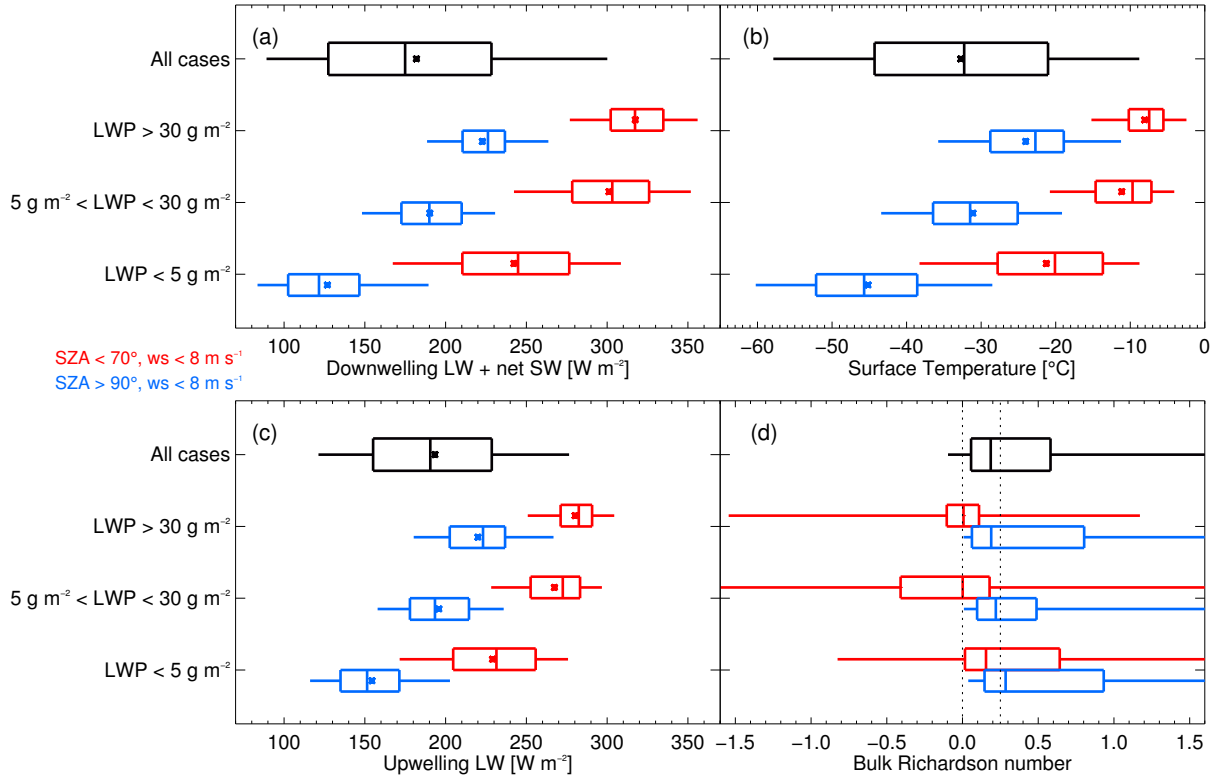

Figure 3.7: Statistics of **(a)** LW↓ + net SW, **(b)** surface temperature, and **(c)** LW↑ for the period spanning January 2011–June 2014. **(d)** Statistics of the bulk Richardson number for the period spanning March 2012–June 2014. The black distribution represents all quality-controlled cases. The red (blue) distributions represent periods when the wind speed $< 8\,m\,s^{-1}$ and the solar zenith angle is $< 70°$ ($> 90°$). Distributions are represented by box-and-whisker plots (the box indicates the 25th and 75th percentiles, the whiskers indicate 5th and 95th percentiles, the middle line is the median, and the * is the mean).

stability. In addition, cloud-driven atmospheric mixing can also affect the low-level atmospheric structure (Shupe et al., 2013a) and liquid-bearing cloud presence, especially in combination with enhanced solar radiation, decrease the near-surface temperature gradient (Hudson and Brandt, 2005; Miller et al., 2013).

This study explicitly shows that the radiative influences of liquid-bearing clouds and/or insolation create neutral or unstable boundary-layer conditions. When the sun is below the horizon, as for the first case study (Sect. 3.3.3.1), the presence of liquid-bearing clouds decreases the stability such that a majority of the cases are weakly stable ($0 < Ri < 0.25$) (Fig. 3.7d). In the absence of liquid-bearing clouds ($\mathrm{LWP} < 5\,g\,m^{-2}$) the surface radiatively cools, the stability increases, and consequently a majority of the cases are strongly stable ($Ri > 0.25$). Solar radiation ($\mathrm{SZA} < 70°$) warms the surface sufficiently to decrease the near-surface stability (Fig. 3.7d). When the sun is present yet there are no liquid-bearing clouds the median Ri is weakly stable. However, when optically thick liquid-bearing clouds ($\mathrm{LWP} > 30\,g\,m^{-2}$) are present the boundary layer is near neutral on average. Interestingly, optically thin liquid-bearing clouds ($5\,g\,m^{-2} < \mathrm{LWP} < 30\,g\,m^{-2}$) lead to more frequent occurrence of more unstable conditions in the presence of insolation, because these clouds emit significant longwave radiation while also allowing significant penetration of solar radiation, thus producing the maximum surface heating. Our results that liquid-bearing clouds of intermediate thickness lead to higher instability agree with studies that show these clouds produce the maximum CRF for elevated sun angles (Bennartz et al., 2013; Miller et al., 2015). Hence, liquid-bearing clouds and/or solar insolation enhance turbulent mixing, facilitating sensible and latent heat exchange, although instability (negative Ri) requires SW↓.

3.3.4.2 SEB responses

Process-based relationships distill our understanding of the underlying physical processes into a succinct form that is informative, yet practical. While clouds, the solar cycle, and other processes can influence the downwelling radiation, process relationships between response terms and forcing terms reveal how variability in downwelling radiation affects the other SEB terms. Performing a

linear fit (fitexy, Press et al., 1992) on the relationship between the forcing and response terms, which includes uncertainties in both terms, yields a slope of −1.01 (Fig. 3.8a), indicating that the SEB is largely radiatively driven, the response terms account for all of the forcing energy flux, and there is approximate closure for the SEB terms calculated here. The scatter in this relationship is due to measurement uncertainties, mismatches of response times in different terms, and the spatial distribution of the instrumentation. The annual evolution of this slope (Fig. 3.9) shows that the SEB response terms balance the forcing terms to within $\approx 10\,\%$ in all months of the year. Thus, any change in forcing terms elicits an approximately equal change in flux through the combination of response terms.

The response to the radiative forcing can be evaluated for each term independently (Fig. 3.8b–e), and as a function of month, showing that each term responds differently throughout the annual cycle (Fig. 3.9). The slope of the linear fit provides an estimate of the relative magnitude (percentage) of the response of each term. The RMS error of the monthly response estimates in Fig. 3.9 is calculated by comparing the estimated values, using the linear fit, to the measured values (Fig. 3.10). The RMS error includes the uncertainty of the measurements involved, any delay in response time greater than 30 min, and variability in the physical response not represented by the linear fit. Generally, the RMS error of the linear fits of all response terms to the driving terms are on the same order of magnitude as the combined uncertainty of the SEB components.

The annual response in the LW↑ term (77 %, Fig. 3.8b) is the largest out of all the response terms, as its magnitude is directly proportional to the surface temperature to the fourth power. The annual cycle of this response shows a weaker response in summer (50–60 %) and a stronger response in winter (65–85 %). The lower response of the LW↑ term in June 2014, compared to winter months during December 2013–February 2014 (or compared to values from June 2011 to 2014), is partially due to the increased response of the latent heat flux for this specific month (Fig. 3.9). Any increase (decrease) of response of an individual term will effectively decrease (increase) the change in surface temperature, and hence the response of LW↑, to radiative forcing.

The response of the sensible heat flux (11 %, Fig. 3.8d) is fairly constant throughout the

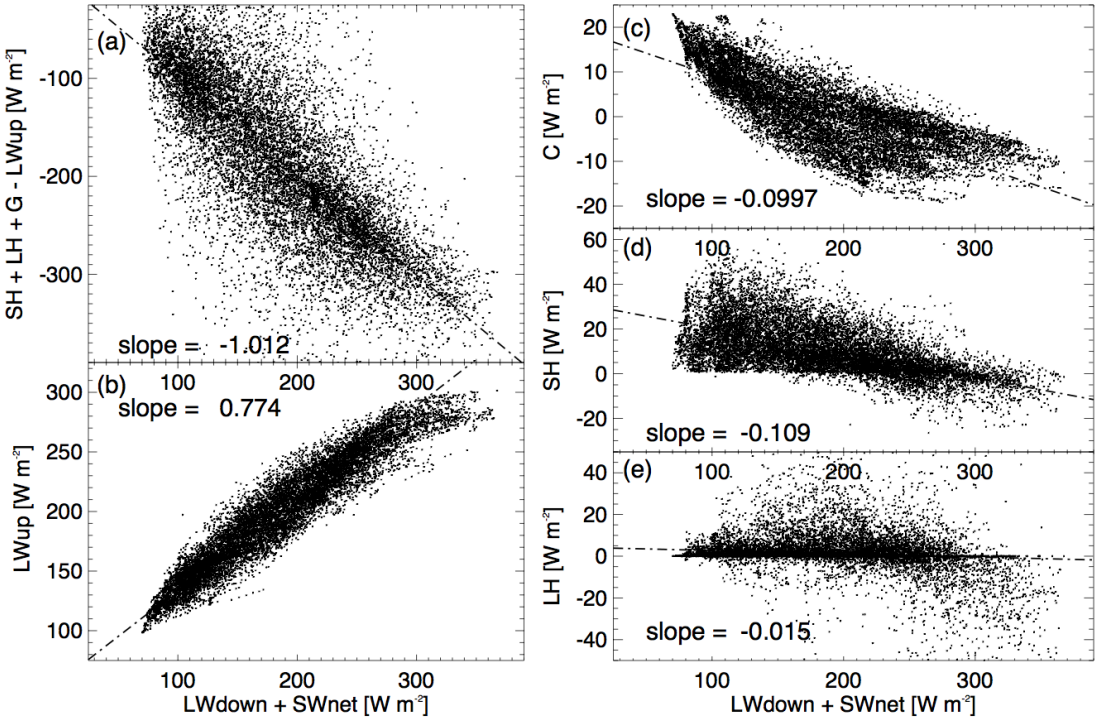

Figure 3.8: Linear regression of data from July 2013 to June 2014. **(a)** Total response (SH, LH, $-$LW$\uparrow$, and G) as a function of the forcing terms (LW$\downarrow$ + net SW). **(b)** LW$\uparrow$, **(c)** conductive heat, **(d)** sensible heat, and **(e)** latent heat flux as a function of the forcing terms. The slope of the best fit linear regression is included in each panel.

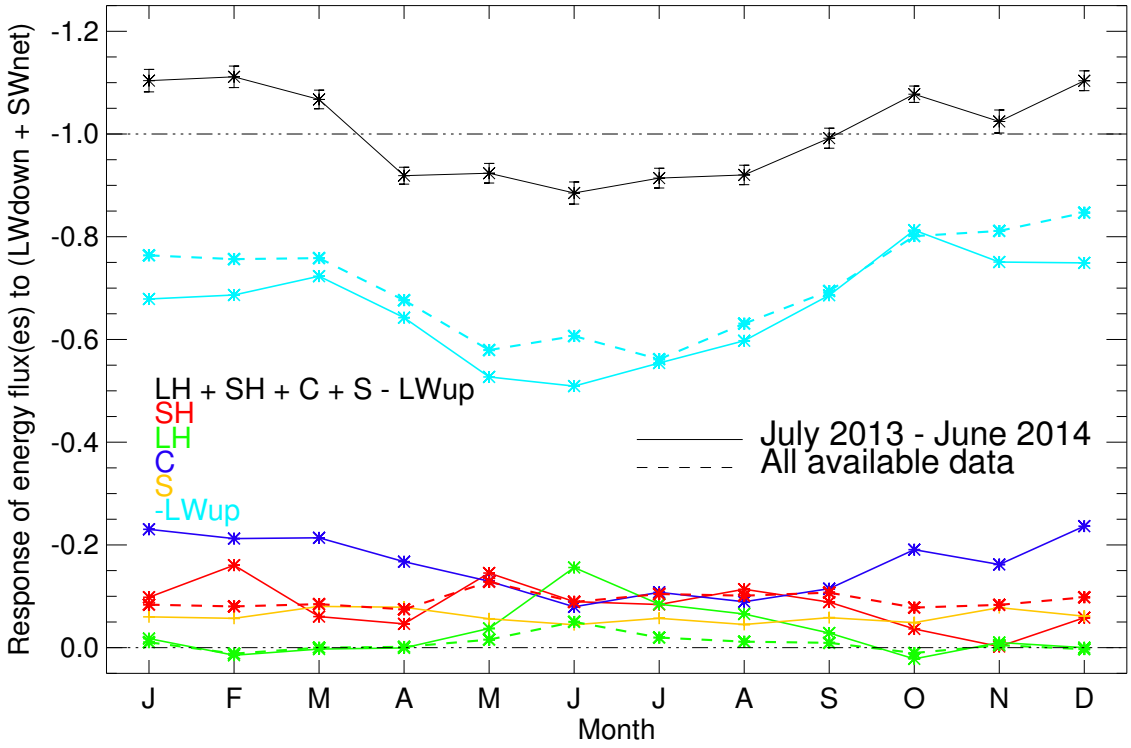

Figure 3.9: Annual cycle of monthly linear regression of responses to the forcing terms. The solid lines are for data spanning July 2013–June 2014 during which all SEB estimates are available. The dashed lines are representative of all available data for the given subset. Note that the y axis decreases upwards.

annual cycle (Fig. 3.9) due to its dependence on both the near-surface temperature gradient and stability (heat transfer coefficient – see Eq. 3.5). For weakly stable conditions, the former term dominates decreasing (increasing) the heat flux for surface warming (cooling), while for very stable conditions the latter term dominates limiting turbulent exchange and increasing (decreasing) the sensible heat flux for surface warming (cooling) (e.g., Grachev et al., 2005). Since these Summit data generally show a decrease in sensible heat flux for an increase in the forcing terms (surface warming), this is consistent with weakly stable conditions on the unstable side of the stability transition shown by Grachev et al. (2005). Therefore, the response of the sensible heat flux to changes in the surface temperature is similar throughout the year and does not show an annual cycle. However, the RMS error of the linear fit (Fig. 3.10) during winter ($9.7\,W\,m^{-2}$) is greater than during summer ($6.0\,W\,m^{-2}$) (i.e., there is more scatter in the sensible heat response in winter), suggesting that conditions in winter are at times very stable and that the sensible heat flux response to radiative forcing is then different. In summer, conditions are rarely very stable so the response in sensible heat flux is more strongly correlated with the change in the forcing terms.

The response of the latent heat flux (1.5 %, Fig. 3.8e) increases in summer compared to other months of the year (Fig. 3.9). The amount of available moisture (Fig. 3.4c) peaks in summer and average PWV values for non-summer (winter) months are below 2 mm (1 mm). Thus, changes to near-surface stability due to changes in the forcing terms produce a smaller response when moisture gradients are small in magnitude.

The response of the conductive heat flux to radiative forcing (10 %, Fig. 3.8c) is greatest in winter (December–February) at 23 % compared to 9 % in summer (June–August). Seasonal changes in the conductive heat response are due to changes in snow density, thermal conductivity, and subsurface temperatures. Warmer subsurface temperatures resulting from prior warm surface temperatures precondition the snowpack, reducing its ability to remove heat from the surface. Decreased density in the summer decreases the thermal conductivity of the near-surface snow pack, also limiting the ability of the subsurface to remove energy from the surface. The RMS error of the linear fit of the conductive heat flux to the forcing terms is relatively low with an annual mean

of $3.2\,W\,m^{-2}$.

The response of the heat storage in the upper subsurface layer is important to consider when accounting for all the energy responses at the surface. Even though the annual mean of S is less than $1\,W\,m^{-2}$ (i.e., there is effectively no annual net change in temperature in the near-surface snow), it is highly variable (annual standard deviation $= 62.5\,W\,m^{-2}$) as this layer can warm or cool rapidly from one half hour period to the next. The heat storage response to the forcing terms also accounts for subsurface heating due to solar penetration. Over the annual cycle the response of S ranges from 4 % in June to 8 % in March, with an average monthly response of 6 % (Fig. 3.9). The slightly larger response of S in March–April indicates the relatively cold near-surface snow is able to store larger amounts of energy originating from radiative sources.

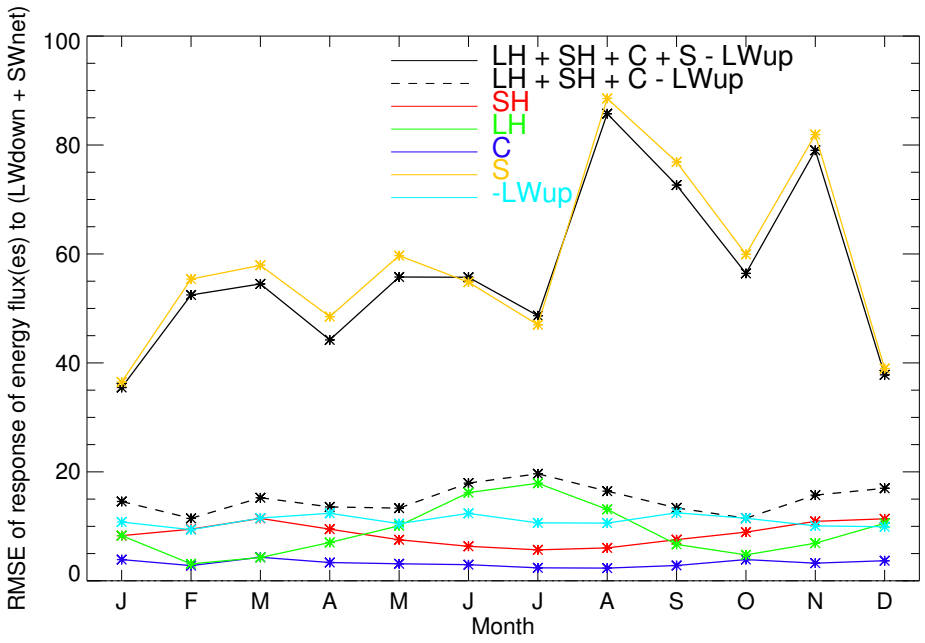

Figure 3.10: Root mean square error ($W\,m^{-2}$) computed from the differences between the measured response of a given term (or combination of terms) and the estimated monthly responses in Fig. 3.9.

Since scatter in S in response to forcing is so large, we first examine the scatter of all the other terms jointly. The RMS error of the linear fit of $(\mathrm{LH} + \mathrm{SH} + C\ -\ \mathrm{LW}\uparrow)$ vs. $(\mathrm{LW}\downarrow + \mathrm{SW_{net}}$ is maximum in July ($19.6\ W\,m^{-2}$) and has an annual mean value of $15.0\,W\,m^{-2}$ (Fig. 3.10). The

maximum RMS error occurs in summer due to an increase in the latent heat RMS error of the linear fit from an annual average value of 9.1 to 15.7 $W\,m^{-2}$ in summer. The RMS error of the linear fit of S is lowest in January (36 $W\,m^{-2}$) and highest in August (89 $W\,m^{-2}$) and has monthly mean RMS error of 63 $W\,m^{-2}$. The high variability, uncertainty, and generally weaker relationship of S with the forcing terms indicate that the estimation of S is the largest unknown in closing the energy budget on short timescales. The 1σ uncertainty of the response of $\mathrm{LH} + \mathrm{SH} + C + S - \mathrm{LW}\uparrow$ to the forcing terms, shown by the error bars in Fig. 3.9, is primarily due to the variability and associated uncertainty in S. However, correctly accounting for the ground heat flux in the upper most layer provides near closure of the surface energy balance, a critical accomplishment of the synthesis of comprehensive data sets given here.

At the ice sheet–atmosphere interface surface temperature is the linchpin that connects the subsurface to the atmospheric boundary layer, responding to changes in the net flux at the surface. The variability in the surface temperature is controlled by changes in the forcing terms and modulated by the response terms. An increase in radiative forcing warms the snowpack; increasing the surface temperature and decreasing the near-surface atmospheric stability. Not surprisingly, the response terms are all associated with surface temperature – either directly proportional or a function of the near-surface temperature gradient. Latent heat flux is also dependent on the near-surface moisture gradient and the ground heat flux is dependent on the thermal conductivity of the snow pack, leading to seasonal differences in their responses. This study highlights the importance of the seasonal changes in the non-radiative responses, which determine the annual cycle of the LW↑ response.

3.3.4.3 Cloud effects on the SEB

The seasonal response of the SEB to cloud presence is estimated by combining the radiative effects of clouds with the observationally based and statistically derived relationships between the forcing and response terms. CRF at the surface, as detailed in Miller et al. (2015), is the instantaneous net radiative effect of clouds. Furthermore, changes in the forcing terms elicit a

response of the surface temperature and the non-radiative SEB terms. Thus, we combine the monthly CRF values reported in Miller et al. (2015) and monthly responses, calculated from the maximum available data (Fig. 3.9), to estimate the corresponding increase in LW↑ and decreases in SH, LH and G attributed to cloud presence. Figure 3.11a shows LW↑ has the smallest increase due to CRF in May ($11.8\,W\,m^{-2}$), the largest increase in October ($33.2\,W\,m^{-2}$), and an annual mean response of $23.4\,W\,m^{-2}$. The non-radiative responses to the annual CRF value of $32.9\,W\,m^{-2}$ are -3.0 (SH), -0.24 (LH), and -7.2 (G) $W\,m^{-2}$. Subtracting the monthly LW↑ response from the monthly mean LW↑ yields an estimate for the amount of LW radiation that would be emitted by the GIS surface in the absence of clouds. Comparing the monthly mean surface temperatures, derived from the measured LW↑ and the estimated clear-sky LW↑, produces the approximate monthly differences shown in Fig. 3.11b, suggesting that clouds increase the surface temperature by 7.8 °C annually during the time period January 2011–October 2013.

3.4 Summary

Characterization of surface energy fluxes and their variability illuminates the important processes that control surface temperatures in central Greenland. Here observations from Summit Station are used to derive all terms of the surface energy budget and to examine key relationships among these terms and with other key atmospheric drivers. Despite the harsh Arctic environment SEB estimates could be made for all the terms for 75 % of the year spanning July 2013–June 2014.

Over the annual cycle atmospheric temperatures in the free troposphere (>1 km) are well correlated with surface temperatures, although energy exchange processes at the surface enhance surface temperature variability. In general, time-series data, monthly mean values, and monthly diurnal cycles all show that the non-radiative SEB terms oppose the increase or decrease of the net radiation. Liquid-bearing clouds and solar insolation strongly modulate the radiative flux that reaches the surface, which affects subsurface temperatures, the stability of the boundary layer, and the near-surface temperature gradients. A pair of case studies illustrate how all the pieces fit together to depict how an increase in surface radiation elicits a response in the surface

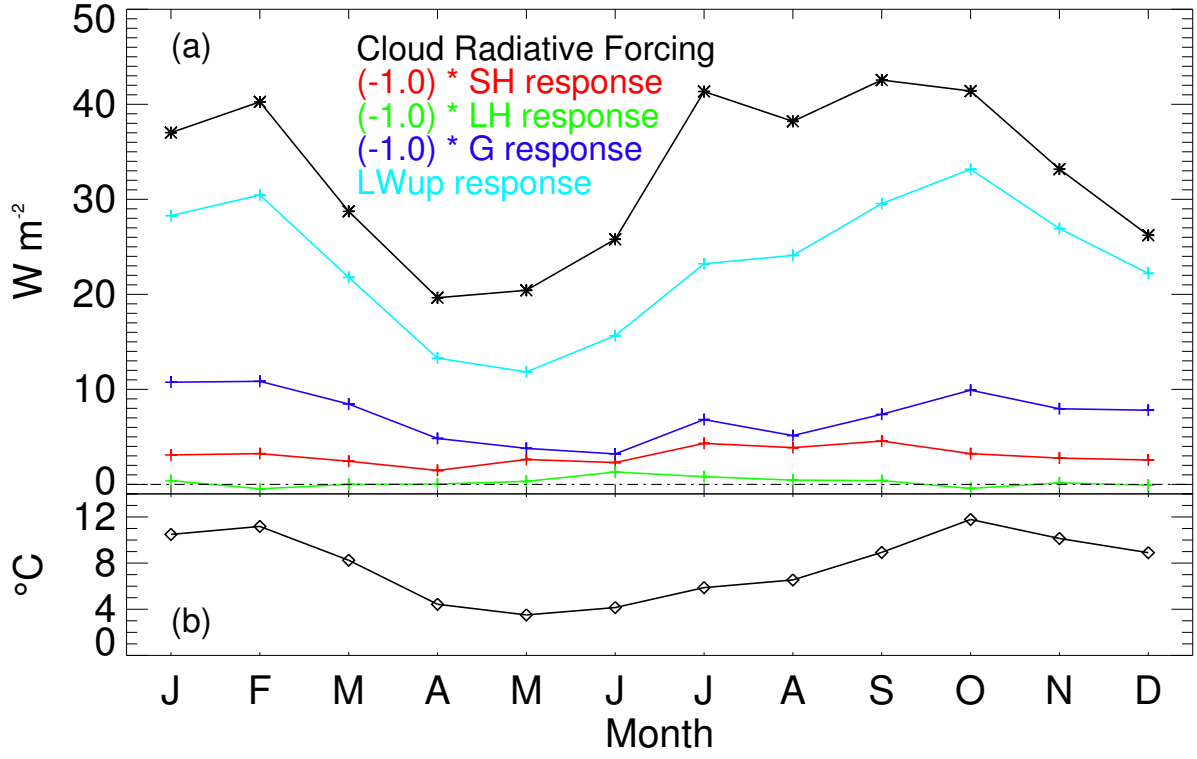

Figure 3.11: **(a)** The annual cycle of cloud radiative forcing (black) from January 2011 to October 2013 (Miller et al., 2015) and estimated annual cycle of responses, calculated from the values in Fig. 3.9, of sensible heat flux, latent heat flux, ground heat flux, and LW↑. **(b)** Monthly temperature effect due to clouds, estimated from the difference between the measured LW↑ and the estimated clear-sky LW↑ value, for the period January 2011–October 2013.

temperature, while also indicating that the increase in temperature is lessened by a decrease in sensible and conductive heat fluxes. The resultant compensation of the non-radiative SEB terms thereafter affects the net amount of surface warming that occurs due to cloud radiative forcing and/or insolation. Similar compensation is apparent when looking at longer-term averages.

To examine these relationships in more detail, radiative forcing terms (LW$\downarrow$ + net SW) were related to the response terms (SH, LH, C, S and LW$\uparrow$) throughout the annual cycle. Linear regression analysis, for the year-round data set relating the response terms as a function of the forcing terms, resulted in a -1.01 slope, indicating general closure in the calculated SEB terms. On average LW$\uparrow$, which is directly linked to surface temperature, responds by about 70 % of a perturbation in incident radiation, with a diminished response in summer. Quantifying how each non-radiative response changes throughout the year provides insight into how much SH, LH, and/or G limit the surface temperature increase due to the occurrence of liquid-bearing clouds and/or insolation:

- Latent heat flux response is near-zero for much of the year, with an increased response in summer.
- Sensible heat flux response is fairly constant throughout the annual cycle ($\approx$ 9 %).
- Ground heat flux, consisting of both heat storage in the upper most $\approx$ 20 cm of snow and the conductive flux below this layer, is the largest non-radiative response for most of the year, with a decreased response in summer.

The enhanced summer latent heat flux response is due to an increase in available moisture and an increase in turbulence during relatively frequent periods of neutral/unstable near-surface conditions. In winter the effect of the stable boundary layer is to dampen the response of the turbulent sensible heat flux, yet this dampening effect is offset by the enhanced near-surface temperature gradient. The consequence of a limited sensible heat exchange during periods of strong radiational cooling is that the sensible heat flux response is relatively constant throughout the annual cycle. Finally, the

ground heat flux response decreases in the summer due to decreases in near-surface snow density and warmer subsurface temperatures.

A previous study by Cullen et al. (2014), spanning the time period 17 June 2000–18 June 2002, also reports the annual cycle of the surface energy budget components at Summit Station. Comparing the annual mean values of this study to the earlier study reveals that Q is $6.8\,W\,m^{-2}$ smaller and SH, LH, and G are 1.6, 0.9, and $4.8\,W\,m^{-2}$ larger, respectively. The differences in the annual mean values could be due to possible decreases in cloud cover (Comiso and Hall, 2014), since the recent annual forcing value is $7.3\,W\,m^{-2}$ smaller than the $190.1\,W\,m^{-2}$ reported by Cullen et al. (2014). July 2014 had the largest occurrence of liquid-bearing clouds for the current study resulting in an average Q of $6.1\,W\,m^{-2}$ compared to $15.6\,W\,m^{-2}$ reported by Cullen et al. (2014). The July 2014 forcing terms are $265.3\,W\,m^{-2}$ compared to $268.0\,W\,m^{-2}$ in 2000–2002, suggesting that a $6.8\,W\,m^{-2}$ increase in LW↑ is likely due to synoptically driven warmer air masses above Summit Station in 2014 and not due to changes in CRF.

In central Greenland, cloud presence in winter (longwave forcing) is unable to produce a neutral stratification. It is only with insolation that neutral and unstable conditions exist. In contrast, over Arctic sea ice, wintertime conditions are near neutral or even slightly unstable nearly 25 % of the time (Persson et al., 2002). More instability over sea ice compared to the GIS may be due to warming of the surface from below due to oceanic influences. Springtime/summertime near-neutral and slightly unstable conditions with shortwave forcing observed here is similar to that observed over sea ice (e.g., Ruffieux et al., 1995; Persson et al., 1997, 2002). Also in agreement with our findings are process diagrams obtained via a modeling study over sea ice (Sterk et al., 2013) that found the non-radiative SEB terms lessen the change in surface temperature due to changes in downwelling radiation. Moreover, observational studies over sea ice (Persson et al., 2002) and in the Greenland ablation zone (van den Broeke et al., 2011) suggest that if/when Summit Station more frequently experiences melt the non-radiative compensation, detailed in this study, may be significantly diminished as energy goes towards surface melting.

These central Greenland results can be used to evaluate how well the annual and diurnal

cycles of the SEB terms are represented in climate models and reanalyses, and specifically the relationship among key terms. It is known that global climate models underestimate the occurrence of liquid-bearing clouds above Greenland (Kay et al., 2016a). We estimate that the underrepresentation of clouds, especially liquid-bearing clouds, should produce annual surface temperature biases ranging from 0 to $-7.8\,^{\circ}\mathrm{C}$. If the representation of liquid-bearing clouds were to improve then the modeled downwelling radiation would likely also improve, but it is unclear if the other SEB terms would realistically adjust. A regional or global climate model's modus operandi is to achieve absolute closure of the SEB; hence this study will be useful in future studies as a valuable tool for pinpointing the processes responsible for possible model surface temperature bias over Greenland and for evaluating model representation of physical processes at the ice sheet–atmosphere interface.

Chapter 4

Model evaluation utilizing surface energy budget measurements

4.1 Introduction

Accurate representation of the exchange of energy at the surface is critical in modeling the Greenland ice sheet (GIS) surface temperature. Fluctuations in the surface energy budget are becoming more consequential to melt duration, extent, and the amount of energy available to melt snow into liquid in the context of increased summer GIS surface temperatures in a warming climate (Hanna et al., 2008). Satellite observations show two major melt events and increasing GIS surface temperatures since 2000 (Hall et al., 2013). The combined amount of surface melt, ice discharge, and snow accumulation ultimately determine the GIS surface mass balance (SMB), which has contributed to about 0.74 $mm\,yr^{-1}$ of global sea level rise during this decade (McMillan et al., 2016). Projected SMB increases due to the precipitation component are lower than decreases due to melt water runoff (Fettweis et al., 2013a), suggesting further GIS mass loss will occur in the future.

Modeling tools are useful to represent past, present, and future Earth system components because they are spatially and temporally complete and can represent many aspects of the system that cannot be observed. By using a static version of data assimilation techniques and model parameters, reanalysis products are a valuable tool for representing the past state of the climate system across many decades. Reanalysis products are often used as "truth" because they incorporate observational datasets into the model framework to produce a spatially consistent and comprehensive portrait of most surface and atmospheric variables. These reanalyses rely on physical parameter-

izations and tend to have higher uncertainties in regions with less assimilation data. Operational weather prediction systems are used to provide accurate forecasts, because they assimilate observations to get an initial atmospheric state; furthermore the model physics are updated more frequently than a reanalysis in order to achieve the best possible forecast of the atmospheric state and surface properties. Global climate models (GCMs) are valuable for investigating future climate scenarios with controlled forcing mechanisms. In addition, GCMs are able to estimate natural variability of the climate system because numerous realizations of the climate can be produced, thus enhancing our understanding of the significance of observed changes. These models are free running without observational constraints.

Global climate models can be used to investigate if SMB trends are anthropogenically forced. Projections using the Community Earth System Model (CESM) suggest the emergence of an anthropogenically derived positive SMB signal is occurring near Summit Station correlated with a negative SMB signal at the GIS periphery (Fyke et al., 2014). It is possible the signal to noise ratio used to determine the emergence of the signal is influenced by an under representation of liquid-bearing clouds in central Greenland that precipitate too frequently (McIlhattan et al., 2017) and an associated cold bias in the maximum summer 2 m temperatures (Kay et al., 2016a). If representation of mixed-phase clouds were to be more realistically represented, surface temperatures would increase in response to cloud presence (Miller et al., 2015), thus decreasing GIS surface mass balance (Van Tricht et al., 2016) and increasing the small amount of mass lost due to sublimation (Cullen et al., 2014). Hence, model deficiencies may limit our ability to represent natural variability of the climate system and predict future changes.

Direct observations are valuable for evaluating the performance of all types of models including GCMs, operational forecast models, and reanalyses. In the past, observations have been sparse in the Arctic (Serreze et al., 2000), but recently larger spatial coverage of satellite, ground-based observations, and reanalysis products have become more readily available (Christensen et al., 2016). Yet there remain significant uncertainties in estimates of surface temperatures from satellite (Shuman et al., 2014) and reanalysis products (Zhang et al., 2011) in central Greenland. Similarly,

difficulties in reproducing diurnal cycles of near-surface temperature in stable atmospheric boundary layers, which occur frequently above the GIS, beleaguers model performance (Holtslag et al., 2013). In addition, models may have offsetting biases when simulating the various components of surface energy budget (Boeke and Taylor, 2016). Thus, to evaluate model surface temperature biases, it is advantageous to measure a comprehensive set of all surface energy budget (SEB) components.

Distilling key physical processes into SEB relationships derived from observations is a useful tool to assess model representation of these processes because a model must inherently account for all energy flux at the surface. Thus, process-based evaluation will lead to improvements in reanalysis, operational models, and GCMs, including the improved ability to represent climate feedbacks. Here, a comprehensive set of measurements at Summit station is used to compare observed components of the SEB and SEB processes to ERA-Interim, Climate Forecast System version 2, and a beta version of the Community Earth System Model. Process-based relationships (Miller et al., 2017) provide a unique perspective on how realistically the ice sheet/atmosphere interaction is represented, discerning whether or not surface temperatures are realistically responding to changes in radiative forcing at the surface and pinpointing which modeled surface energy flux(es) improperly modulate changes in the downwelling radiation. As such, it can be determined if an improved representation of cloud properties or other processes in a model will effectively improve the representation of surface temperature variability.

4.2 Datasets

4.2.1 Measurements

The SEB over the central GIS is a combination of radiative (Q), sensible heat (SH), latent heat (LH), and ground heat (G) fluxes and balances according to the following equation:

$$0 = Q + SH + LH + G \tag{4.1}$$

All SEB components have the same convention, such that a positive value represents an energy flux toward the surface and negative value represents energy flux away from the surface. At other GIS locations melt is a more important factor of the SEB but in general at Summit Station the melt term is neglected because of the rarity of surface melt (Nghiem et al., 2012).

The radiative flux is separated into upwelling(↑) and downwelling(↓) components of the longwave(LW) and shortwave(SW) radiation, thusly:

$$Q = LW\downarrow - LW\uparrow + SW\downarrow - SW\uparrow. \tag{4.2}$$

The upwelling and downwelling radiation components, measured by Kipp and Zonen CG4 pyrgeometers (LW) and pyranometers (SW), are provided by the Swiss Federal Institute of Technology. The SH and LH fluxes are primarily calculated via the bulk aerodynamic method and the two-level profile method, respectively. The ground heat flux is estimated for a 1-year period only, providing a complete annual cycle of estimates of all the surface energy budget terms from July 2013 – June 2014. Measurements of the radiative components, SH, and LH predate the beginning of the ground heat flux measurements (1 July 2013), with start dates of January 2011, June 2011, and March 2012, respectively. The SEB calculations and meteorological measurements used as input are detailed in Miller et al. (2017) and can be accessed online from the Arctic Data Center [1] .

Ground-based observations at Summit Station are used to represent larger domains in the model simulations, hence the observations are smoothed over a 3-hour running window to remove local variability in a given parameter. The 3-hour window is the approximate amount of time it would take a typical parcel of air to advect across a model grid box. The relative homogeneity of the central Greenland ice sheet, compared to complexities associated with terrestrial sites (Foken, 2008), limits the sampling error when comparing point measurements to larger domains. All model fields are interpolated to the Summit coordinates from the four model coordinates in closest proximity. When applicable, the observations are averaged over the model integration period, requiring the observed values to be available for at least 2/3 of the averaging period. Each model requires a

[1] doi:10.18739/A2Z37J

different averaging time, thus the observational variability shown by the monthly statistics will be different in each of the model comparison sections.

Miller et al. (2017) find that the surface energy budget at Summit is radiatively driven, such that the statistics over an annual cycle indicate that changes in the radiative forcing terms (LW↓ + net SW) are completely compensated by the response terms (SH + LH + G - LW↑). The responses of individual SEB terms to radiative forcing are calculated by performing a linear fit using the sum of the forcing terms as the dependent variable and taking into account measurement uncertainly of all components. The resultant slope represents the response of a given term to changes in forcing over a specified time period. The main drivers that influence the forcing terms are the presence of a cloud, especially a liquid-bearing cloud, and/or insolation. Cloud presence has a positive radiative forcing affect throughout the annual cycle, due to high albedo year-round which limits the cloud SW cooling effect (Miller et al., 2015). Variability in surface albedo can also influence the forcing terms but at Summit Station the relatively constant surface albedo is less of a factor than variations in downwelling radiation. The response of LW↑ is used as a proxy for a surface temperature response, because it is proportional to temperature to the fourth power, such that a positive(negative) response of LW↑(-LW↑) indicates warming of the surface due to forcing. The responses of SH, LH and G modulate the degree to which LW↑ responds to changes in forcing.

Surface temperatures are estimated from the LW↑ measurements using a greybody approximation, with an estimated surface emissivity of 0.985. Albedo is calculated as the daily total SW↑ divided by the daily total SW↓, which reduces errors due to sub-daily changes in snow metamorphism, possible tilting of sensors, and poor cosine response (van den Broeke et al., 2004). Liquid water path (LWP) is derived from a pair of microwave radiometers, similar to Turner et al. (2007a). During May – June 2014 the HATPRO microwave radiometer was off-site for repairs, hence there are no statistics available for LWP during these months.

4.2.2 Model Description

Proper representation of surface temperatures and the physical-processes that determine surface temperature variability are important in all types of models including reanalysis, operational models, and climate models. Thus, an example of each model type is evaluated, including ERA-Interim (ERA-I), Climate Forecast System version 2 (CFSv2) model, and the Community Earth System Model (CESM).

The European Center for Medium-Range Weather Forecasts provides 3-hourly forecasts initialized every 12-hours by ERA-Interim (ERA-I) Reanalysis (Dee et al., 2011). The spatial resolution of ERA-I is approximately 80 km and the time period considered here spans January 2010 – May 2016. Since the system is not coupled the ground heat flux is regarded as the residual of the other SEB terms, maintaining conservation of surface energy flux, which is critical to the modeling framework.

The NOAA National Centers for Environmental Prediction (NCEP) created the Climate Forecast System (CFS) model for seasonal retrospective and operational forecasts. CFSv2 (Saha et al., 2014) output, spanning January 2011 – October 2016, is the operational extension of the Climate Forecast System Reanalysis (CFSR, Saha et al., 2010) with updated coupled atmosphere-ocean-land model physics. The spatial resolution is 0.2 by 0.2 degrees, which is equivalent to a grid box of approximately 22.6 km by 6.9 km around Summit Station. NCEP CFSv2 data was provided by the NOAA/OAR/ESRL PSD and can be obtained from their web site[2] .

The Community Earth System Model (CESM) is a fully coupled global climate model (Hurrell et al., 2013) maintained by the Climate and Global Dynamics Laboratory at the National Center for Atmospheric Research. This free running climate model should generally reproduce the state of the current climate within its natural variability, but is not expected to model specific synoptic events. In fact, a process based evaluation framework is well-suited for a free running model in that this perspective can provide some degree of insight without having to run the model for multiple years or ensemble members. The 1-year CESM dataset shown here is beta version 7, composed of potential

[2] http://www.esrl.noaa.gov/psd/

candidates for the Community Atmosphere Model version 6 (CAM6) and Community Land Model version 5 (CLM5), which are critical components of the soon to be released CESM2. The data, output at 30-minute intervals, are representative of the current climate, using representative sea surface temperatures and green house gas forcing from 2000. A spatial resolution of 0.94 (latitude) by 1.25 (longitude) translates to a grid box size around Summit Station of 104 km x 43 km. The lack of liquid-bearing clouds over Greenland is a major deficiency in CAM5 (Kay et al., 2016a), likely due to an overactive Wegener-Bergeron-Findeisen process (McIlhattan et al., 2017). Observations found in Miller et al. (2015) have been useful in evaluating the radiational impact at the surface of potential changes to cloud microphysical parameterizations. Improving the representation of clouds has been a major thrust for the development of CAM6.

4.3 Model Evaluation

4.3.1 ERA-I

The ERA-I skin temperatures, hereafter considered to be the surface temperature, are compared to the observationally derived surface temperature estimates. Monthly statistics of the 3-hourly surface temperature values (Figure 4.1) indicate that the ERA-I monthly averages are greater than the observed values due to larger discrepancies in minimum monthly temperatures compared to the maximum values. A subsampled data set (red and the black statistics in all figures) contains matching sampling times from the year July 2013 – June 2014 where there exist quality controlled observations of a given parameter. Sampling over longer time periods (ERA-I: January 2010 – May 2016 and Obs: January 2011 – June 2014, when available) provides context on how deviations of the year long data set are the result of inter-annual variability. The annual mean surface temperature for the 1-year period is 2.8°C greater in ERA-I compared to the observations and 3.9°C greater for the extended sampling periods. The bias in the 2 m temperature is 0.4°C smaller than the surface temperature bias. For most months the bias of the 1-year dataset is representative of the extended time period, with the notable exception being in January 2014, which indicates a greater

inter-annual variability in the observations compared to ERA-I.

To investigate the differences in the minimum temperature values and the resultant warm bias of ERA-I, comparisons of the individual radiative components are performed to characterize differences in the radiative balance at the surface. Generally, LW↓ is greater in the observations (Figure 4.2a), with exceptions in April, May, August and September, resulting in an annual bias of $-8.3\,W\,m^{-2}$ in the 1-year data and $-5.1\,W\,m^{-2}$ for the extended datasets. Despite the underestimation of LW↓ in ERA-I, the LW↑ comparisons (Figure 4.2b) reinforce the warm biases in Figure 4.1 indicating that differences in surface emissivity are not the primary reason for surface temperature differences. The annual mean SW↓ biases of 8.7 $W\,m^{-2}$ in the 1-year data set and 5.2 $W\,m^{-2}$ in the extended data set (Figure 4.2c), oppose the LW↓ biases. Despite the monthly SW↓ being too large in ERA-I, the SW↑ is smaller in the model compared to observations (annual biases of 1-year: $-6.3\ W\,m^{-2}$ extended-data: $-7.6\ W\,m^{-2}$). Because clouds serve to increase the LW↓ and reduce the SW↓, the differences in sign of the LW↓ and SW↓ biases suggest cloud presence and/or optical thickness is under-represented.

The turbulent and ground heat flux comparisons between ERA-I and the observations (Figure 4.3) indicate other possible contributions to surface temperature biases. The surface is warmed(cooled) by turbulent mixing of overlying warm(cold) air, deposition(sublimation), or conduction of subsurface heat toward(away from) the surface. Compared to the observations, ERA-I sensible heat flux is biased high and has greater variability, as indicated by the monthly interquartile range (IQR), particularly in the winter months. In fact, the ERA-I SH variability is greater during all months, but during the summer the monthly mean values are much closer to observed values and from May – August have a small negative bias (Figure 4.3a). The ERA-I LH monthly values are also biased low from May – August and biased high throughout the rest of the year (Figure 4.3b). Stronger radiative cooling by ERA-I in the winter (Figure 4.3d) correlates with an over estimation of the SH flux, in contrast to May – August when a stronger than observed radiative warming in ERA-I results in an under estimation of the SH flux. The annual ERA-I bias of G for the 1-year dataset is $-2.3\ W\,m^{-2}$ (Figure 4.3c). The high variability in the observed G values is in part due to the

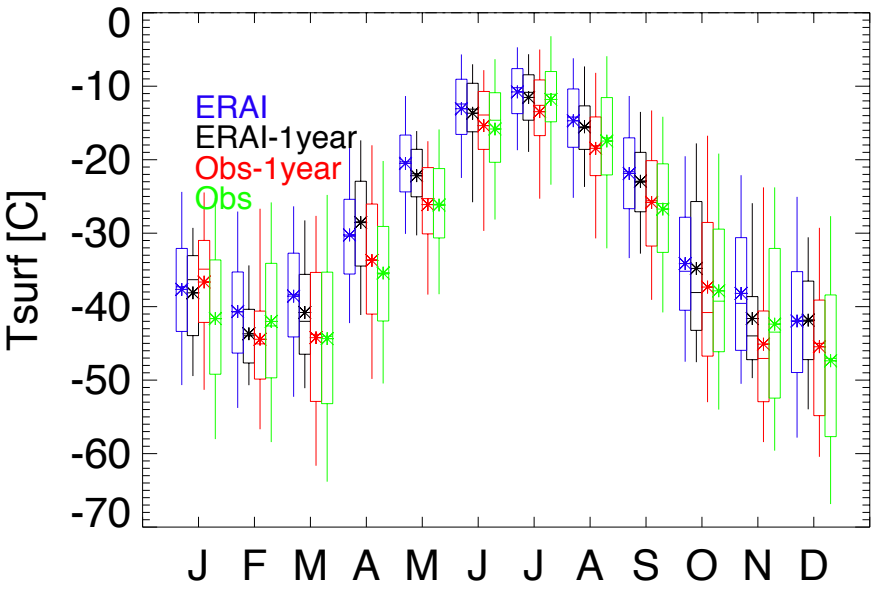

Figure 4.1: Monthly surface temperature distributions are represented by box-and-whisker plots (the box indicates the 25th and 75th percentiles, the whiskers indicate 5th and 95th percentiles, the middle line is the median and the * indicates the mean). Red (observed) and black (ERA-I) distributions are during identical sampling periods when T_{surf} observation is available from July 2013 – June 2014. Green (observed) distributions are from January 2011 – June 2014. The blue (ERA-I) distributions are from January 2010 – May 2016.

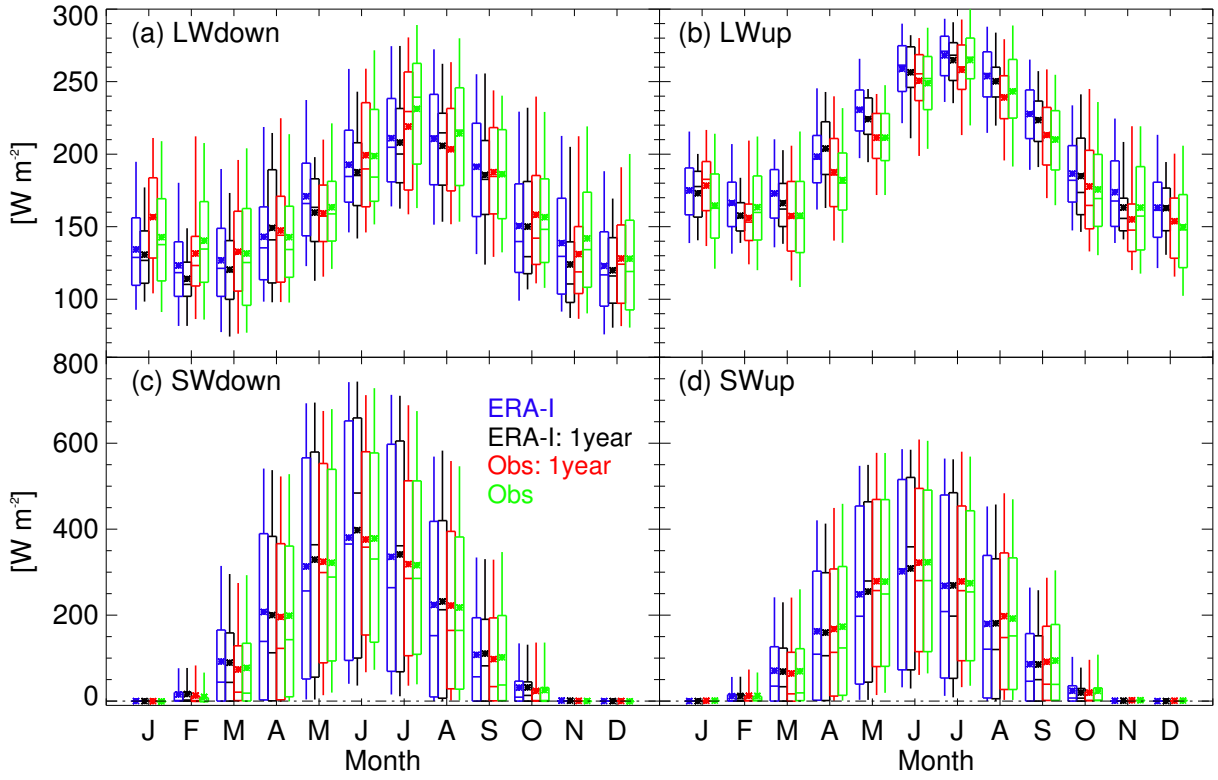

Figure 4.2: Monthly distributions of (a) LW↓, (b) LW↑, (c) SW↓, and (d) SW↑. Red (observed) and black (ERA-I) distributions represent identical sampling periods when the given observation is available from July 2013 – June 2014. Green (observed) distributions are from January 2011 – June 2014, when available. Blue (ERA-I) distributions are from January 2010 – May 2016.

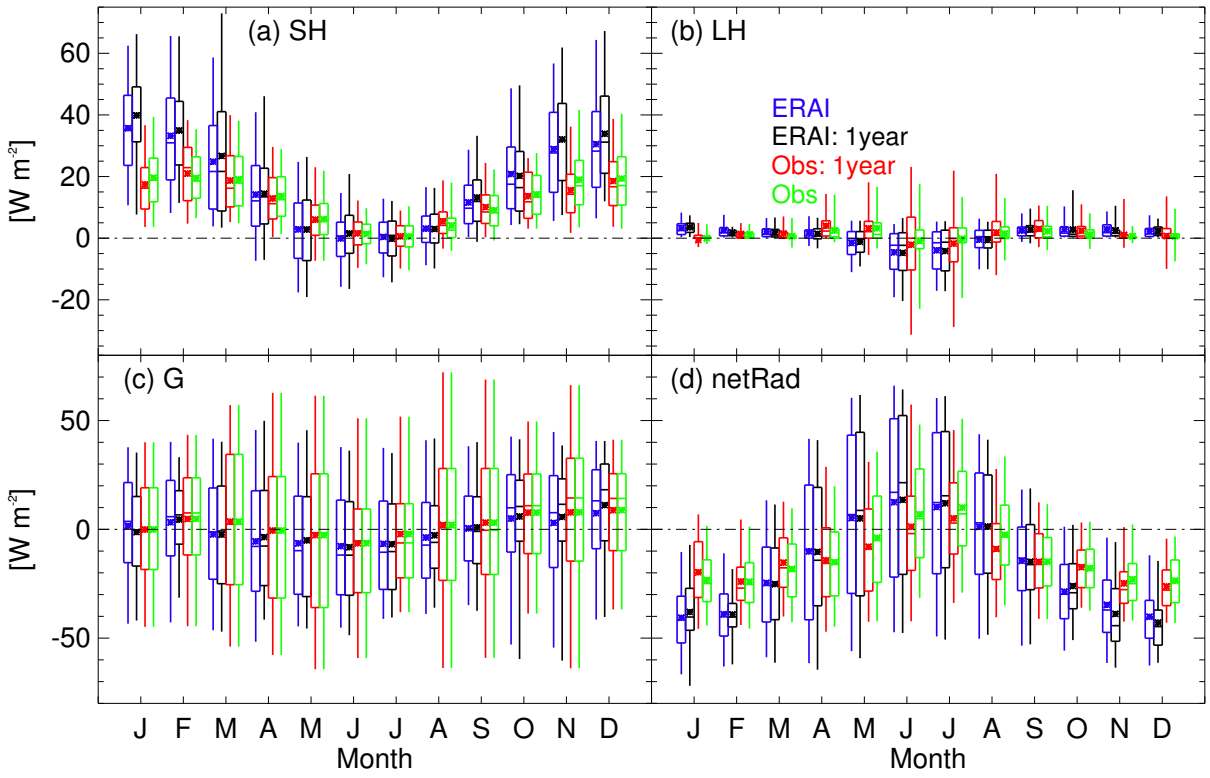

Figure 4.3: Monthly distributions of (a) SH, (b) LH, (c) G, and (d) net radiation. Red (observed) and black (ERA-I) distributions represent identical sampling periods when the given observation is available from July 2013 – June 2014. Green (observed) distributions are from January 2011 – June 2014, when available. Blue (ERA-I) distributions are from January 2010 – May 2016.

80% uncertainty in the estimates of G (Table 3.1). March and August have the largest G biases, when the monthly mean values indicate G is warming the surface in the observations and cooling the surface in ERA-I. The biases in the turbulent and ground heat flux components could be due to differences in boundary-layer parameterizations or inadequacies in the cloud radiative forcing.

The presence of liquid-bearing clouds results in additional radiation at the surface, compared to a clear-sky scene. The amount of liquid water contained in overlying clouds, or the liquid water path (LWP), modulates the amount of downwelling radiation impinging on the surface, decreasing SW↓ and increasing LW↓ (Miller et al., 2015). The surface temperature adjusts accordingly, resulting in new radiative balance at the surface, altering the temperature gradients between the overlying atmosphere, surface, and subsurface. Monthly ERA-I and MWR based observations (Figure 4.4) show an underestimation of LWP by ERA-I throughout the annual cycle. This deficiency of LWP is consistent with the deficiency of LW↓ and surplus of SW↓ in ERA-I.

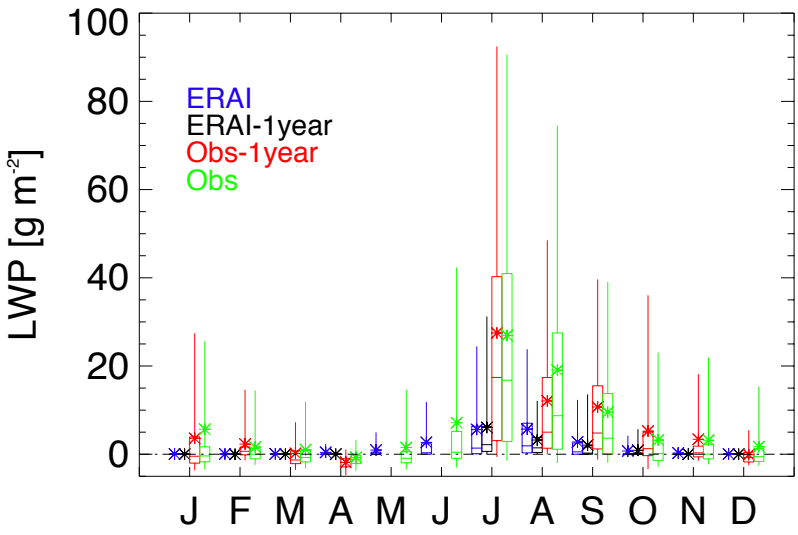

Figure 4.4: Monthly distributions of liquid water path. Red (observed) and black (ERA-I) distributions represent identical sampling periods when the given observation is available from July 2013 – June 2014. Green (observed) distributions are from January 2011 – June 2014, when available. Blue (ERA-I) distributions are from January 2010 – May 2016.

Miller et al. (2017) report that the SEB is primarily radiatively driven by the forcing terms,

which are a combination of LW↓ plus net SW. At Summit the sun is below the horizon from mid November to early February. Figure 4.5a reinforces that from November - February the ERA-I deficiencies in the LW↓ component corresponds to deficiencies in the LWP. The occurrence of liquid-bearing clouds in January 2014 was more frequent than during Januarys 2011 – 2013 and, thus, the ERA-I January forcing bias was -26.0 $W\,m^{-2}$ for the 1-year data compared to -4.8 $W\,m^{-2}$ for the extended data. Despite the observations indicating the monthly LWP being greater than ERA-I values the ERA-I forcing terms are greater than the observations and have more variability from April – September (Figure 4.5a). The summer (June – August) ERA-I forcing bias is 17.7 $W\,m^{-2}$ and 10.9 $W\,m^{-2}$ for the 1-year and all data sets, respectively. Excess SW radiation absorbed by the surface in ERA-I, due to the surface albedo being too low, results in an overestimation of the forcing terms during periods of significant insolation. From March – September the average albedo in ERA-I is 0.79 compared to 0.87 in the observations. The observed values are similar to May - July broadband albedo values reported in Wright et al. (2014), which varied between approximately 0.82 – 0.90.

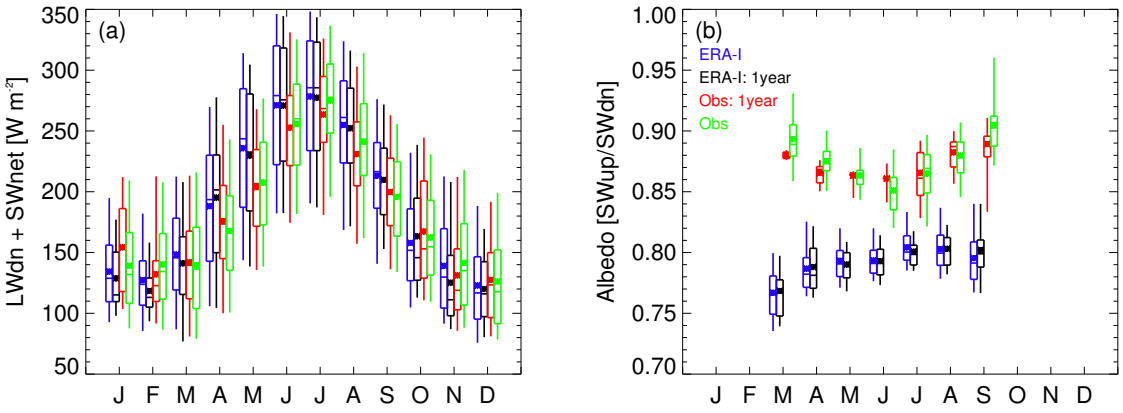

Figure 4.5: Monthly distributions of (a) LW↓ + net SW and (b) surface albedo. Red (observed) and black (ERA-I) distributions represent identical sampling periods when the given observation is available from July 2013 – June 2014. Green (observed) distributions are from January 2011 – June 2014, when available. Blue (ERA-I) distributions are from January 2010 – May 2016.

ERA-I underestimation of liquid-bearing clouds and surface albedo will have compensating effects on surface temperature biases. The response terms, which comprise SH, LH, G, and LW↑

components of the SEB, are dependent on the magnitude of the forcing terms. Hence, to investigate whether biases in the response terms are attributable to discrepancies in radiative forcing, a process-based perspective is utilized to indicate if changes in forcing elicit a realistic response. By defining the G as the residual of the other SEB terms the sum of the ERA-I responses completely account (i.e., -1.0 slope) for any changes to the forcing terms (Figure 4.6). The observations do not show an exact accounting (i.e., -1.0 slope) of the total response to changes in the observations, indicating possible seasonal errors in some of the SEB component responses.

Comparisons between ERA-I and observationally derived responses illuminate differences and similarities regarding the modulation of surface temperature by the sensible, latent, and ground heat fluxes. From April – September the ERA-I sensible heat flux response is within 3% of the observed values (Figure 4.6), yet from October – March the modeled SH response discrepancy increases and changes sign, indicating an increase in SH for an increase in radiative forcing. This could be due to the model limiting heat exchange during high stability periods or the surface not cooling enough during clear-sky periods. The LH response is also positive from October – March and the April – September LH response is similar to the observed response from the 1-year data set. The inferred ERA-I ground heat flux response is overestimated throughout the annual cycle, producing a response 26% greater than the observed response. The ground heat flux response serves to lessen the LW↑ response, which is 17% lower than what is observed by the broadband measurements. Generally, the bias in ERA-I surface albedo produces more radiative forcing, but is compensated by an overactive response of G, resulting in moderately warmer surface temperatures.

4.3.2 CFSv2 evaluation

Similar to ERA-I, CFSv2 LW↓ is underestimated and LW↑ is overestimated for most of the annual cycle (Figure 4.7a,b). Throughout this Chapter the biases of the extended data period will be indicated in parenthesis to provide a muti-year perspective, if available. The LW↑ annual bias for CFSv2 is 8.7(9.9) $W\,m^{-2}$ for the 1-year(extended) data set, indicating that annual mean surface temperatures are too warm. During summer the LW↑ bias for the 1-year period is negative

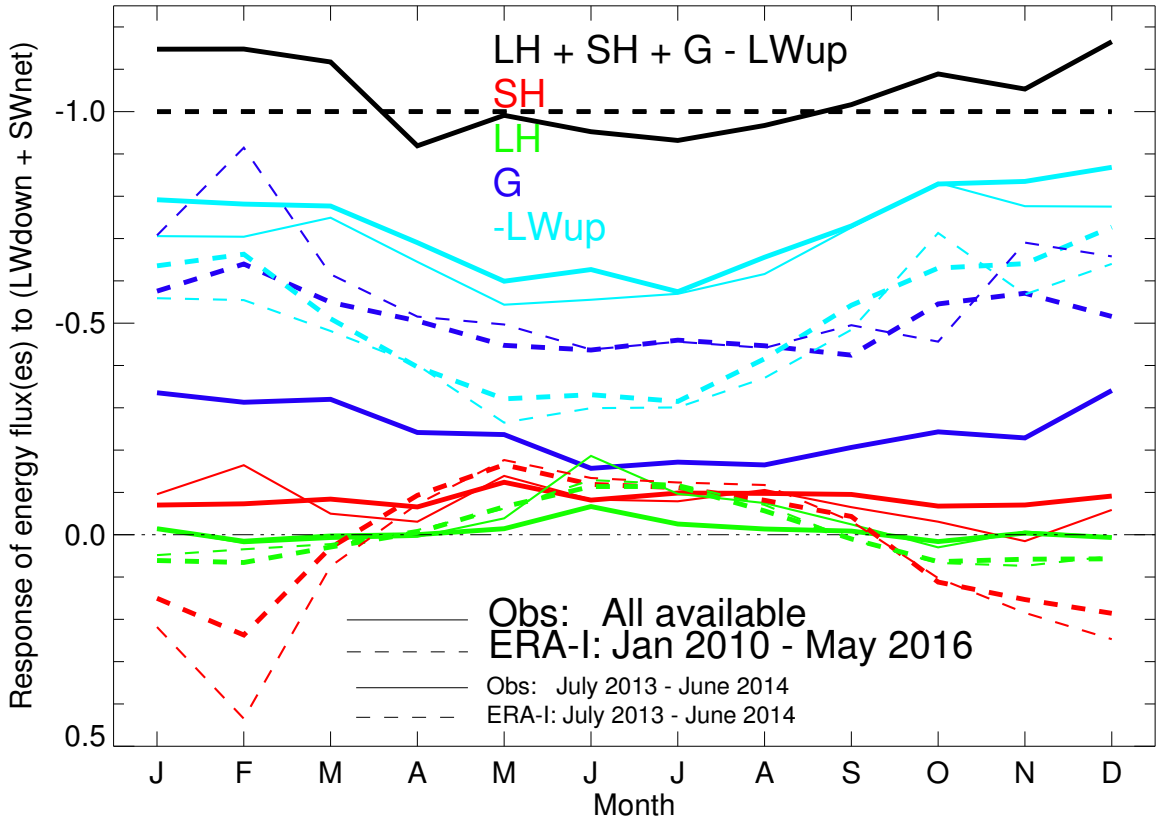

Figure 4.6: Annual cycle of monthly linear regression of responses to the forcing terms. The thin solid lines are for observational data spanning July 2013 – June 2014 during which all SEB estimates are available and the thick solid lines are representative of all available data for the given subset. The thin dashed lines are for ERA-I data representative of identical sampling periods when the given observations are available from July 2013 – June 2014 and the thick dashed lines are ERA-I data from January 2010 – May 2016.

-2.4(-5.9) $W\,m^{-2}$ indicating that the surface is too cold. SW↓ has more variability (IQR) but less range (difference between the 5th and 95th percentiles) than observed values (Figure 4.7c), with an annual bias of 4.6(4.3) $W\,m^{-2}$. The negative bias in LW↓ and positive bias in SW↓ suggest that CFSv2 under represents liquid-bearing clouds. The annual SW↑ bias is less than 1 $W\,m^{-2}$ yet has greater variability than the observed SW↑ (Figure 4.7d), due to higher variability of the SW↓ component.

The monthly mean net radiative fluxes in CFSv2 are less than the observed radiative balance (Figure 4.8d) due to a deficiency in LW↓ and an excess of thermal emission. An annual SH positive bias of 16.2(14.0) $W\,m^{-2}$ is a major contributor to enhanced warming of the surface in CFSv2 (Figure 4.8a). LH flux biases are smaller than those of the SH flux and lead to enhanced warming of the surface in the winter and more cooling during the summer (Figure 4.8b). The CFSv2 ground heat flux values and variability are extremely small, indicating heat flux into the snowpack is negligible.

Annually, CFSv2 forcing terms are 5.5 $W\,m^{-2}$ lower than observed values (Figure 4.9a). In contrast to ERA-I, there is a deficit of summer CFSv2 forcing despite similarities in enhanced SW fluxes compared to observations. The CFSv2 albedo is closer than ERA-I to the observed albedo value (Figure 4.9b) with a bias of -0.024(-0.026), effectively over-estimating the amount of SW radiation absorbed by the surface.

The CFSv2 responses of the sensible, latent and ground heat fluxes all compensate for increases or decreases in the forcing terms throughout the annual cycle (Figure 4.10). The LH and SH responses are greater than observed responses, respectively averaging 8% and 15% higher responses for all available data. The monthly CFSv2 ground heat flux response ranges between 3-7%, much less than the observed range of 15-35%. The weak response of the ground heat flux is partially offset by the stronger than observed responses of the turbulent heat fluxes. The result is that the bias of annual mean CFSv2 LW↑ response (11%) is less than the bias of the ERA-I response (22%). Generally, the CFSv2 surface temperatures are too warm despite deficits in the forcing terms because SH provides too much warming.

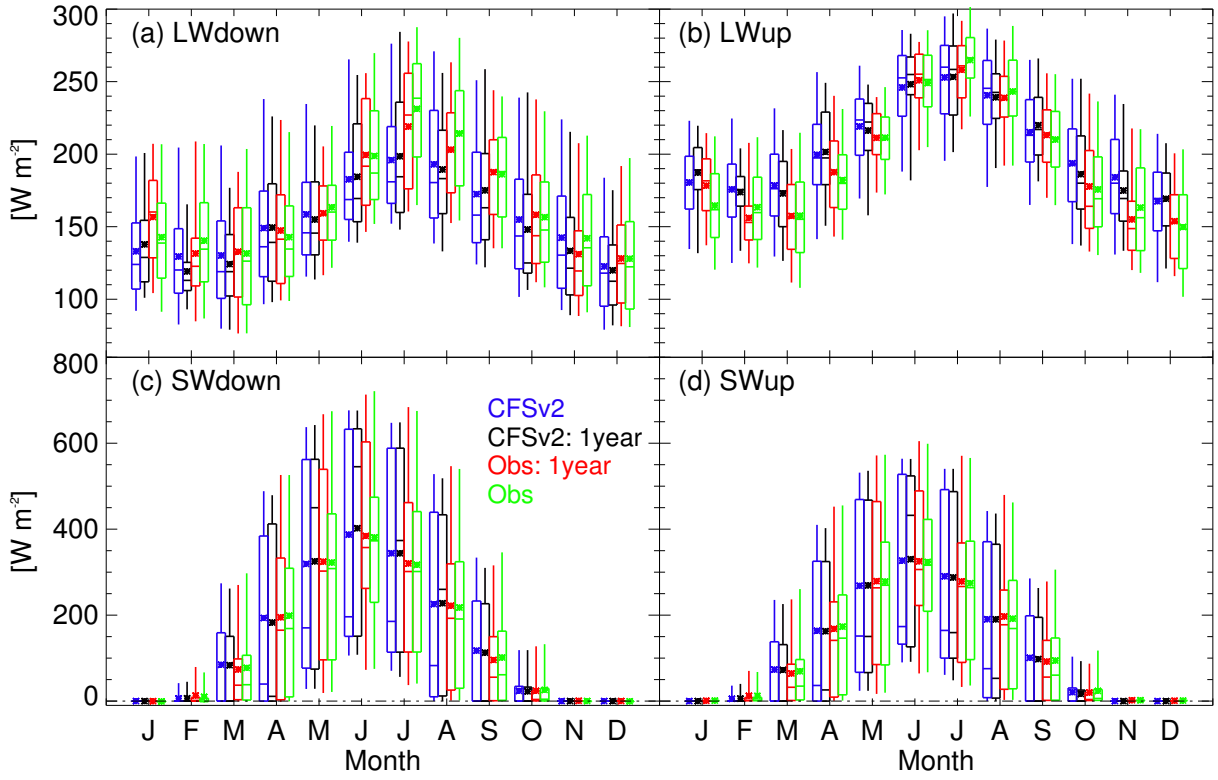

Figure 4.7: Monthly distributions of (a) LW↓, (b) LW↑, (c) SW↓, and (d) SW↑. Red (observed) and black (CFSv2) distributions represent identical sampling periods when the given observation is available from July 2013 – June 2014. Green (observed) distributions are from January 2011 – June 2014, when available. Blue (CFSv2) distributions are from January 2011 – October 2016.

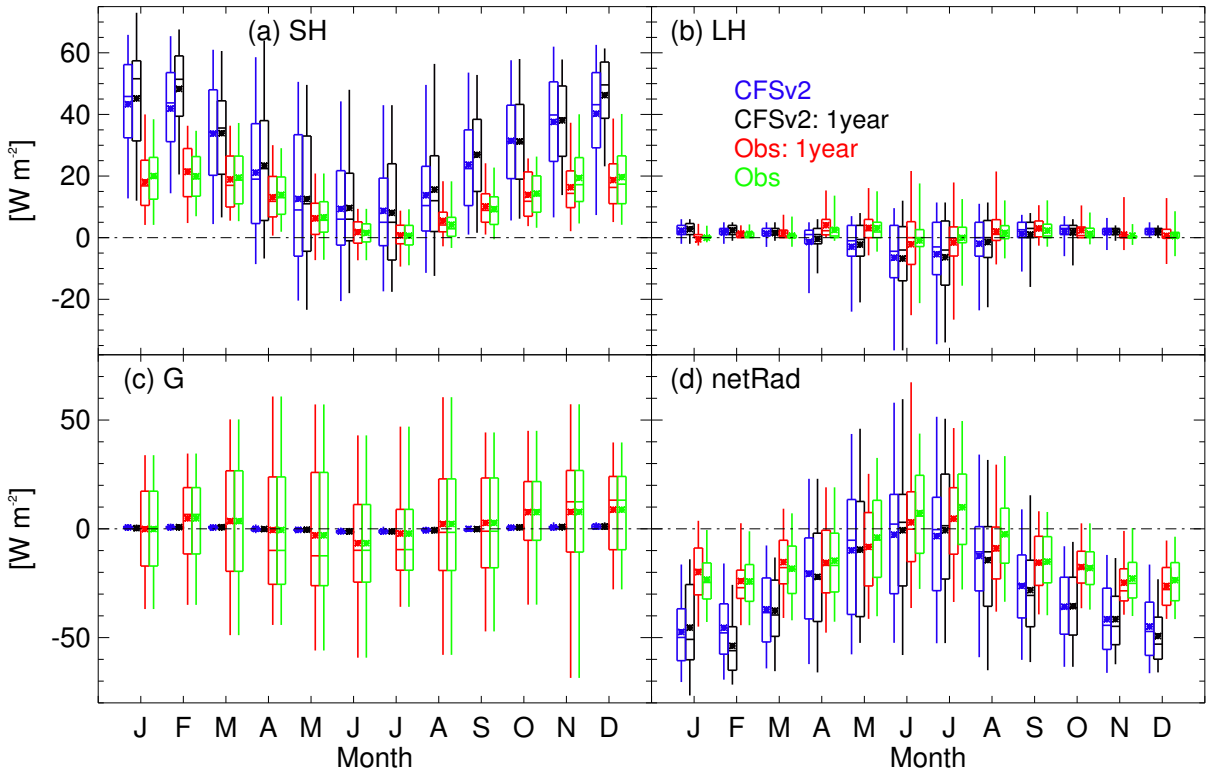

Figure 4.8: Monthly distributions of (a) SH, (b) LH, (c) G, and (d) net radiation. Red (observed) and black (CFSv2) distributions represent identical sampling periods when the given observation is available from July 2013 – June 2014. Green (observed) distributions are from January 2011 – June 2014, when available. Blue (CFSv2) distributions are from January 2011 – October 2016.

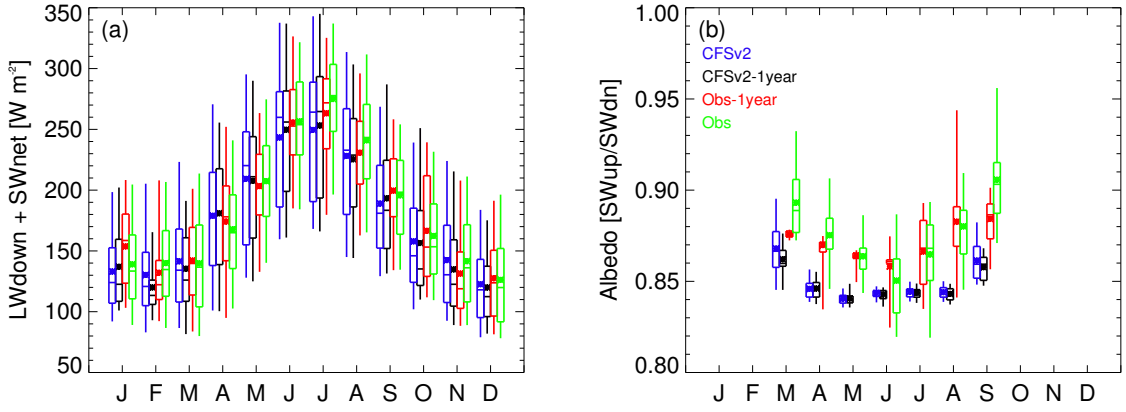

Figure 4.9: Monthly distributions of (a) LW↓ + net SW and (b) surface albedo. Red (observed) and black (CFSv2) distributions represent identical sampling periods when the given observation is available from July 2013 – June 2014. Green (observed) distributions are from January 2011 – June 2014, when available. Blue (CFSv2) distributions are from January 2011 – October 2016.

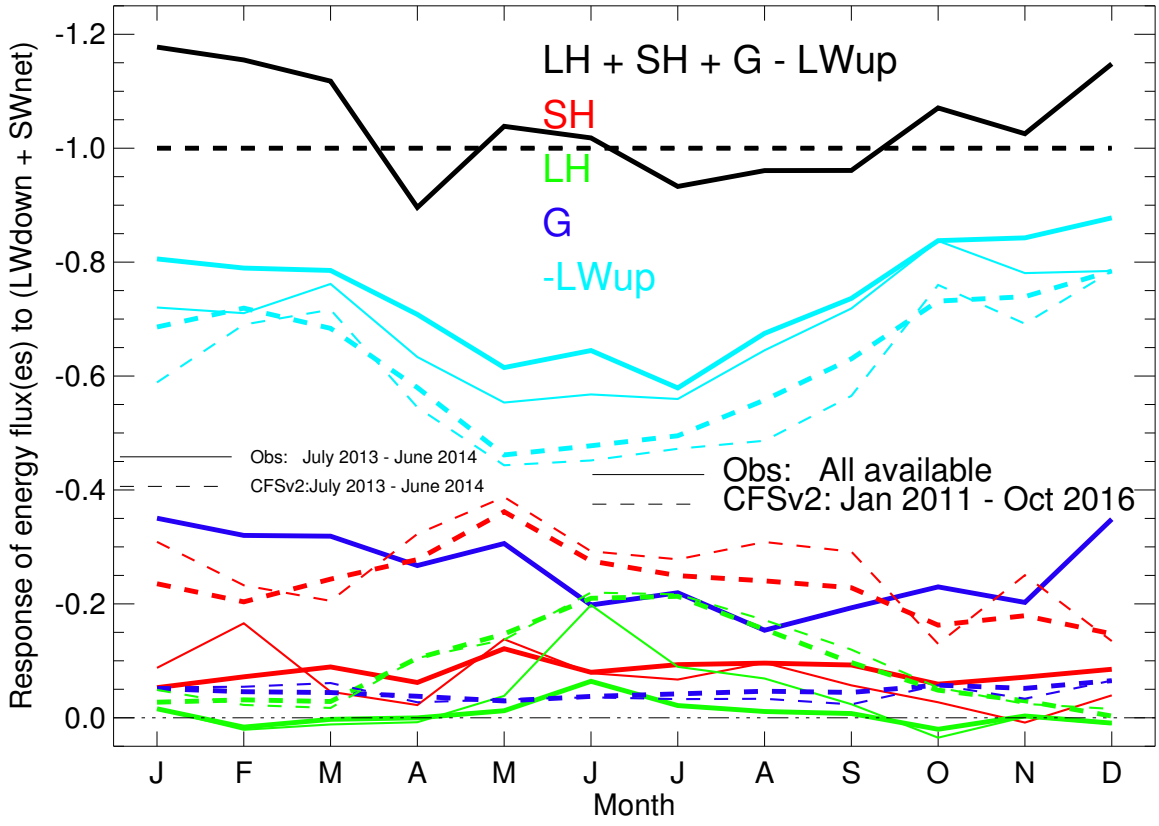

Figure 4.10: Annual cycle of monthly linear regression of responses to the forcing terms. The thin solid lines are for observational data spanning July 2013 – June 2014 during which all SEB estimates are available and the thick solid lines are representative of all available data for the given subset. The thin dashed lines are for CFSv2 data representative of identical sampling periods when the given observations are available from July 2013 – June 2014 and the thick dashed lines are CFSv2 data from January 2010 – October 2016.

4.3.3 CESM evaluation

The one year CESM data set is representative of current climate conditions, yet this free running model is not expected to reproduce actual synoptic conditions for a given time period. Hence, figures in this subsection will only diplay monthly statistics for the CESM run and the maximum data available for the corresponding observational data set.

The CESM annual LW↑ bias of 7.1 $W\,m^{-2}$ indicates that surface temperatures in CESM are warmer than observed, with exceptions occuring during the months of January, April, and July (Figure 4.11b). The largest LW↑ deficit occurs in January (-15.2 $W\,m^{-2}$) and the largest surplus in November (29.1 $W\,m^{-2}$). The annual CESM LW↓ bias is -3.7 $W\,m^{-2}$, with May, June, and October producing more LW↓ than observed (Figure 4.11a). Despite a small mean summer LW↓ bias, there are large offsetting differences between June (27.1 $W\,m^{-2}$) and July (-22.3 $W\,m^{-2}$). The annual mean biases of the SW↓ and SW↑ components are -3.9 and -8.3 $W\,m^{-2}$, respectively (Figure 4.11c,d). The IQR of the CESM SW components indicate a more accurate representation of the net SW variability compared to ERA-I and CFSv2.

From August – April the CESM SH warms the surface more than is reported in the observations, contributing an annual bias of 6.7 $W\,m^{-2}$ (Figure 4.12a). In addition, the monthly variability of the modeled SH is greater than the observed values. The deficit in the CESM LH values from April – August is offset by the surplus throughout the rest of the year resulting in a mean annual bias of -0.6 $W\,m^{-2}$ (Figure 4.12b). The annual CESM G bias is -1.8 $W\,m^{-2}$ (Figure 4.12c). The CESM net radiative flux is biased low (-7.0 $W\,m^{-2}$) except for the months of May and June (Figure 4.12d), indicating more near-surface stability in CESM from July – April compared to observations.

Instances of high LWP occur in CESM (Figure 4.13), indicating the ability to model mixed-phase clouds throughout the annual cycle. The 95th percentiles of the monthly CESM distributions (upper whiskers, Figure 4.13) are in many months greater than the observed values. This skewness indicates that the model may under-estimate the frequency of occurrence of liquid-bearing clouds

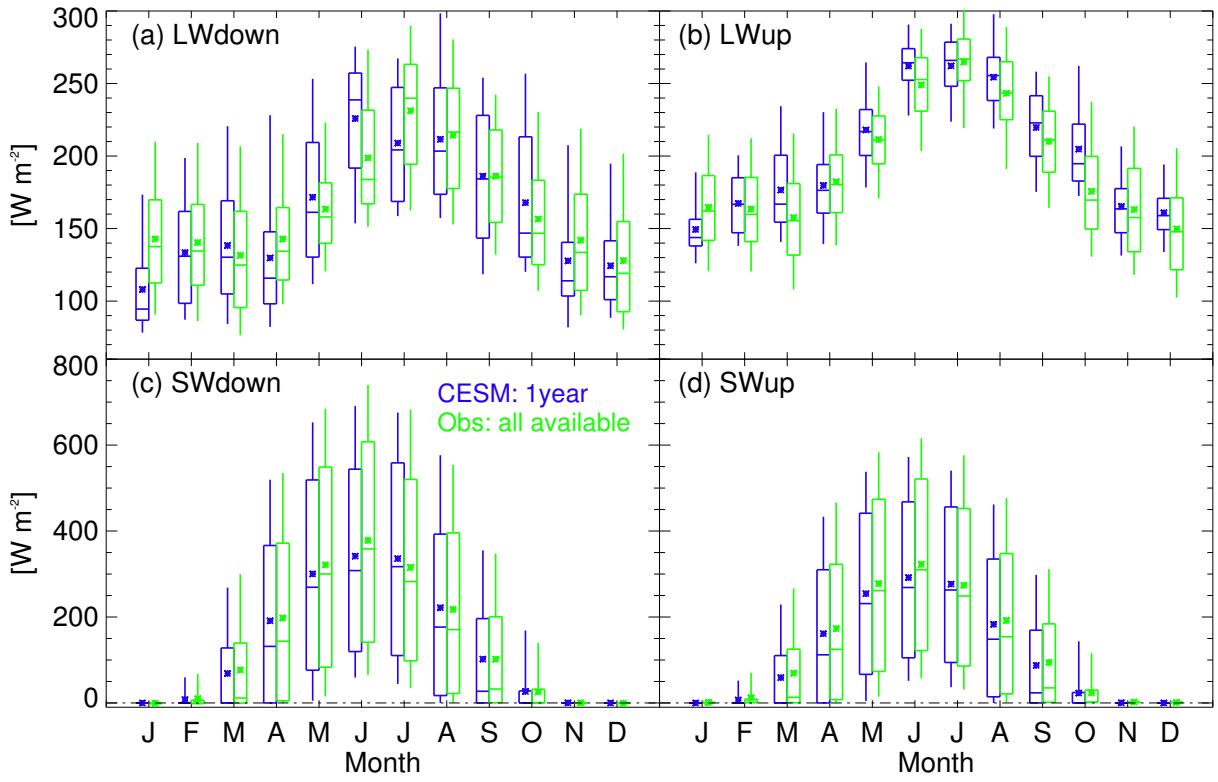

Figure 4.11: Monthly distributions of (a) LW↓, (b) LW↑, (c) SW↓, and (d) SW↑. Green (observed) distributions are from January 2011 – June 2014, when available. Blue (CESM) distributions are from the 1-year dataset.

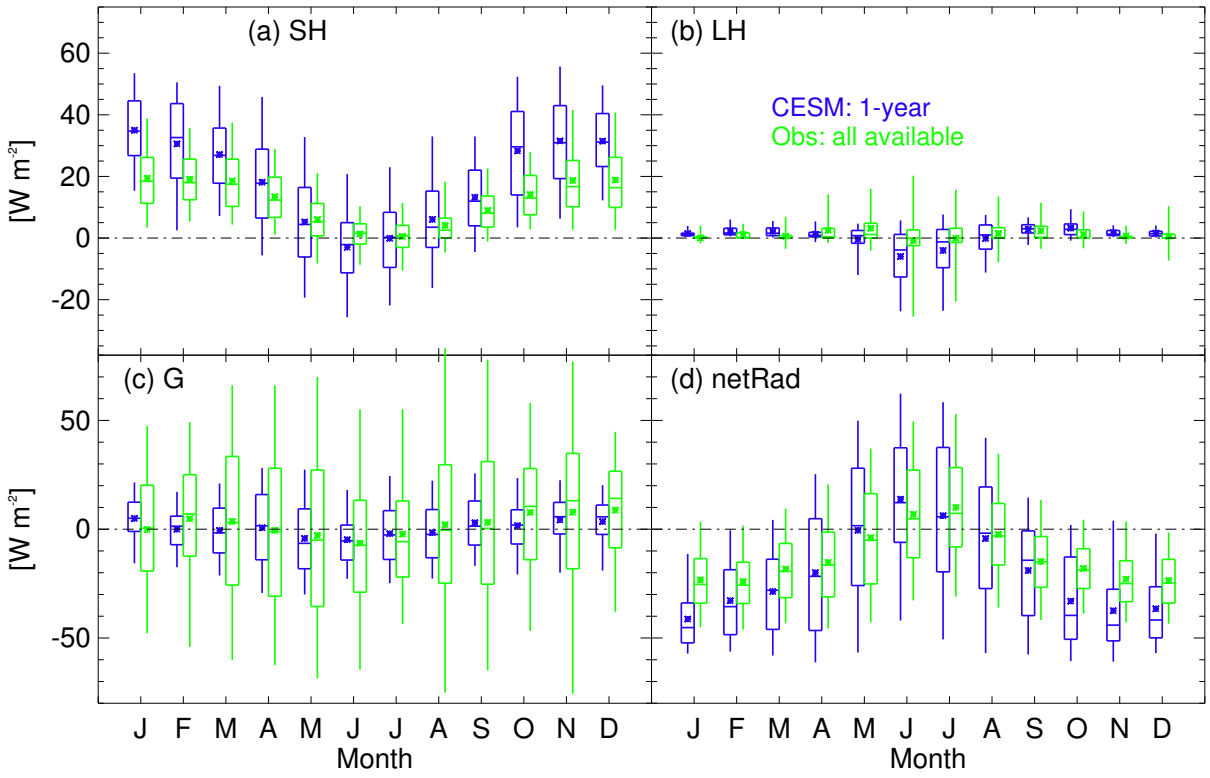

Figure 4.12: Monthly distributions of (a) SH, (b) LH, (c) G, and (d) net radiation. Green (observed) distributions are from January 2011 – June 2014, when available. Blue (CESM) distributions are from the 1-year dataset.

in a given month and those that do occur are have a greater optical thickness. LWP biases correspond to biases in the downwelling radiation. For example, the over(under)estimation of LWP in June(July) by CESM correlates to a surplus(deficit) of LW↓ and a deficit(surplus) of SW↓.

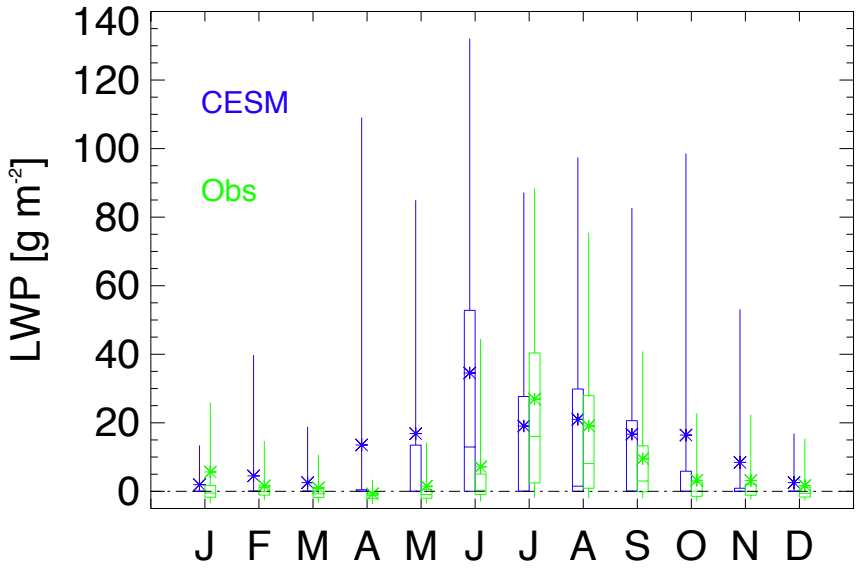

Figure 4.13: Monthly distributions of liquid water path. Green (observed) distributions are from January 2011 – June 2014, when available. Blue (CESM) distributions are from the 1-year dataset.

As a result of a more realistic representation of mixed-phase clouds, compared to ERA-I or CFSv2, the CESM forcing terms are generally more realistic (Figure 4.14a). Annually the CESM forcing bias is -0.4 $W\,m^{-2}$, yet from June–August (summer) the bias is postive (7.5 $W\,m^{-2}$) and from December–February (winter) it is negative (-12.9 $W\,m^{-2}$). On average the albedo is 0.03 lower in CESM compared to observations, indicating about a 3-4% surplus of the amount of SW radiation absorbed by the surface. The June CESM albedo values are greater than the observed values, likely due to the large amount of modeled LWP (Figure 4.13), which acts to decrease the overall angle of incidence of the sun, thus increase surface albedo.

CESM differences in individual SEB components are, in part, due to inter-annual variability of the atmospheric properties, but consideration of the responses to radiative forcing isolate how

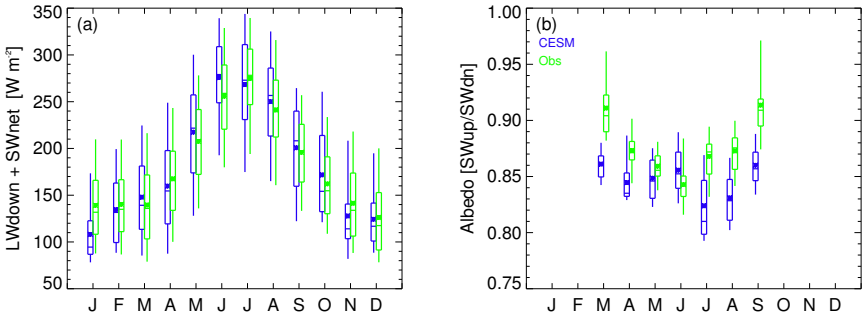

Figure 4.14: Monthly distributions of (a) LW↓ + net SW and (b) surface albedo. Green (observed) distributions are from January 2011 – June 2014, when available. Blue (CESM) distributions are from the 1-year dataset.

well CESM captures the processes-based relationships, which are independent of the year-to-year variability of the forcing terms. The ground heat flux response in CESM has an annual bias of effectively 0%, although the summer difference of -9% offsets the winter difference of 11% (Figure 4.15). Over the annual cycle the CESM SH and LH responses are greater than the observed responses by 15 and 2 %, respectively. The CESM SH responses are greater than the observed responses in every month, in contrast to the biases of the monthly LH responses, which are negative from October – March. The CESM LW↑ response is 23% lower than the observed response indicating that surface temperature variably, due to changes in radiative forcing, is underestimated in CESM. The primary factor responsible for deficits of the LW↑ response is the over active response of the SH flux. Generally, CESM best represents the radiative forcing, yet the response analysis demonstrates an incorrect partitioning of that energy in the system.

4.4 Discussion and Summary

Observationally-based estimates of all SEB components provide a comprehensive perspective to evaluate surface temperature biases in ERA-I, CFSv2 and CESM. All the energy flux at the surface must be accounted for, thus misrepresentation of any SEB component will lead to a warm or cold bias in modeled surface temperature. LW↑, which is proportional to surface temperature to the fourth power, is used as a proxy for surface temperature comparisons because this circumvents

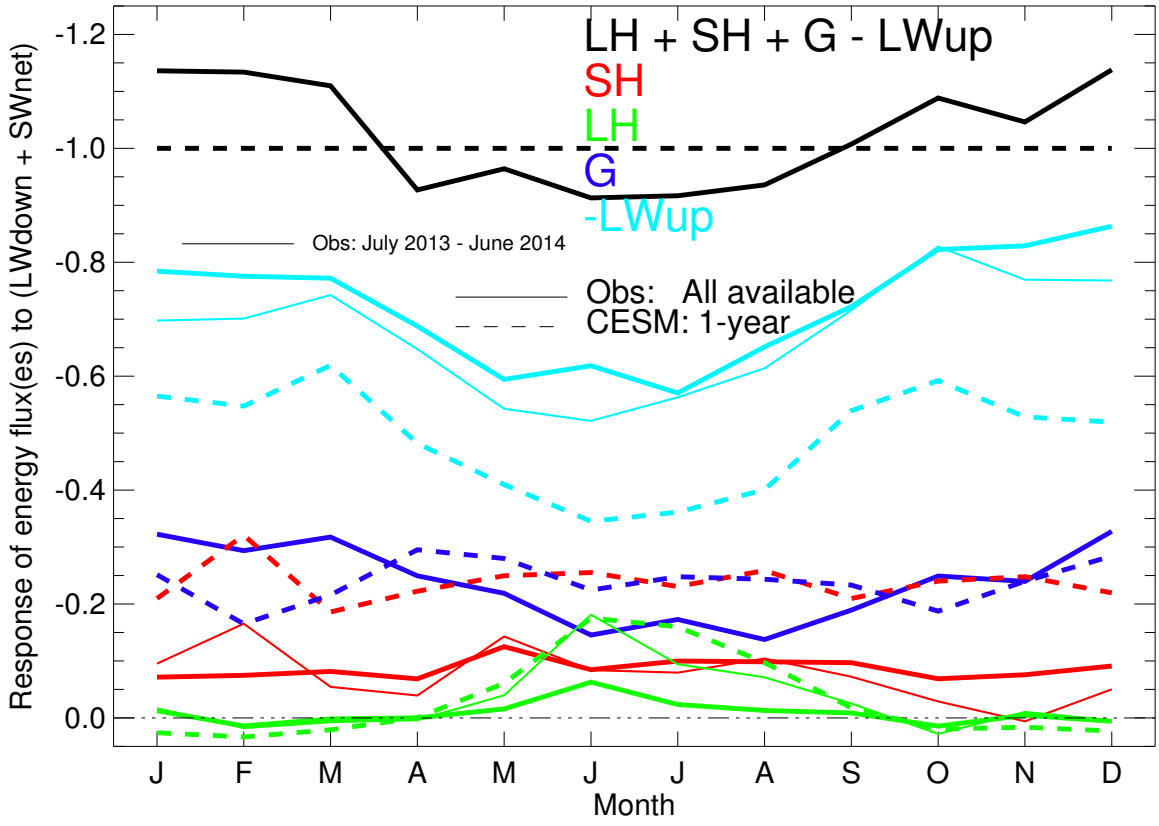

Figure 4.15: Annual cycle of monthly linear regression of responses to the forcing terms. The thin solid lines are for observational data spanning July 2013 – June 2014 during which all SEB estimates are available and the thick solid lines are representative of all available data for the given subset. The thick dashed lines are the CESM data from the 1-year dataset.

implicit assumptions involved in estimating surface temperature from LW derived observations. Temperature at a reference height of 2 m (T_{2m}) is highly correlated with surface temperature (Shuman et al., 2014) and provides a metric for how well the near-surface atmosphere is represented. Table 4.1 compares ERA-I, CFSv2, and CESM biases of 2 m temperature, radiative components, SH, LH, G, and forcing terms. To highlight how the biases differ throughout the annual cycle, seasonal averages of monthly mean biases are calculated for two radiatively distinct periods; summer (June–August) and winter (December–February).

Table 4.1: Seasonally averaged monthly mean biases for 1-year period spanning July 2013 – June 2014 and (extended data periods). T_{2m} biases in units of degrees Celsius and the SEB component biases in units of $W\,m^{-2}$.

	ERA-I		CFSv2		CESM	
	summer	winter	summer	winter	summer	winter
T_{2m}	1.9°(1.9°)	1.7°(3.5°)	-0.6°(-1.2°)	4.0°(4.4°)	(1.7°)	(0.6°)
LW↓	-6.8(-10.0)	-17.2(-10.2)	-16.4(-24.2)	-13.1(-8.7)	(0.72)	(-15.1)
LW↑	7.9(7.8)	1.8(8.9)	-2.4(-5.9)	14.0(15.3)	(7.2)	(-0.05)
SW↓	18.0(9.2)	N/A	15.8(13.8)	N/A	(-4.0)	N/A
SW↑	-13.2(-13.2)	N/A	2.5(6.0)	N/A	(-12.4)	N/A
SH	-1.1(-0.9)	17.2(13.7)	8.4(8.5)	27.2(22.0)	(-1.0)	(13.2)
LH	-2.5(-3.1)	2.1(2.1)	-4.3(-4.8)	1.9(1.4)	(-3.6)	(1.2)
G	-3.7(-3.9)	0.3(-0.4)	1.2(1.2)	-3.8(-3.7)	(-0.6)	(-1.7)
Forcing	17.7(10.9)	-15.6(-6.9)	-7.1(-17.2)	-12.2(-6.4)	(7.5)	(-12.9)

The largest temperature biases are for the CFSv2 winter, indicating a 4°C and 14 $W\,m^{-2}$ warm bias (Table 4.1) of T_{2m} and LW↑, respectively. In fact, all modeled periods shown in Table 4.1 indicate a warmer than observed T_{2m}, except summer CFSv2 values. The weak to strong warm biases in most model periods, and weak ($\approx$1°C) cold bias in CFSv2 summer, are in contrast to the large underestimation of LW↓ in all model periods (excepting CESM summer). For all three models the winter LW↓ deficit is offset by a surplus of SH flux warming the surface, providing an explanation for why a lack of LW↓ coincides with warmer than observed surface temperatures.

During summer CFSv2 maintains a positive SH bias, in contrast to ERA-I and CESM which have a -1 $W\,m^{-2}$ bias, indicating ERA-I's summer LW↓ deficit is compensated by other factors.

CESM does a reasonable job of representing summer downwelling radiation. In summer CFSv2 and ERA-I have a deficit in LW↓ and an associated surplus of SW↓ (Table 4.1) most likely due to lack of modeled clouds that emit downwelling radiation and reflect insolation. The SW↓ bias should be offset in part by a corresponding SW↑ bias, unless the surface albedo is inaccurate. Indeed, ERA-I surface albedo is 9 % lower than observed values, indicating that the excess SW absorbed by the surface compensates for under-representation of radiative warming due to clouds. The lower than observed CESM albedo is balanced by the positive summer LW↑ bias.

Commonality of the LH flux seasonal biases across the 3 models indicates more summer sublimation (-3 to -4 $W\,m^{-2}$) and more winter deposition (1 to 2 $W\,m^{-2}$) in each model. The amplified seasonal cycle of LH exchange acts to lessen seasonal changes of surface temperatures, although the magnitude of LH differences is limited by the relatively dry conditions at Summit. The seasonal biases of G are different in each model; ERA-I is negative in summer and near zero in winter, CFSv2 is slightly positive in summer and negative in winter, and CESM is slightly negative during both seasons and, as such, no clear relationship between monthly mean surface temperature biases and G biases are found.

It might be expected that increases(decreases) in forcing terms would lead to appropriate warm(cold) biases in surface temperatures. Yet, a strong correlation between biases in forcing terms (LW↓ + net SW) and surface temperature is not evident. SH can provide significant compensation to offset deficiencies in radiative forcing. Despite small monthly biases of LH and G, the response of these fluxes to changes in radiative forcing generally serves to weaken the diurnal cycle of the surface temperature. Diurnal variability of surface temperature is an important consideration, especially in summer when daily maximum temperatures are important for determining if the melting point is reached, although 6-hour or 3-hour temporal resolution data could miss short warming events.

Table 4.2 summarizes the differences in modeled and observed responses to changes in the forcing terms during summer and winter. In all models there is an underestimation of the LW↑

response throughout the annual cycle. The LW↑ difference is larger in the summer for ERA-I and CFSv2 compared to winter and CFSv2 LW↑ response is only 5% lower than observed in winter. ERA-I LW↑ response is 26% too low in the summer, which coincides with a positive bias in the forcing terms (Table 4.1). The magnitude of the CESM LW↑ response is consistently lower than observed.

Table 4.2: Differences in response (modeled response - observed response) to changes in forcing (LW↓ + net SW). Note a negative value suggests that the model provides more compensation for a change in forcing. The primary numbers are for a 1-year period (July 2013 – June 2014) and the numbers in parenthesis are differences between the extended time periods, when available.

	ERA-I		CFSv2		CESM	
Response	summer	winter	summer	winter	summer	winter
-LW↑	0.26(0.27)	0.14(0.14)	0.12(0.12)	0.05(0.09)	(0.24)	(0.26)
G	-0.28	-0.41	0.16	0.29	-0.09	0.11
SH	-0.04(-0.01)	0.41(0.27)	-0.21(-0.17)	-0.13(-0.13)	(-0.15)	(-0.17)
LH	0.01(-0.06)	0.04(0.06)	-0.08(-0.16)	-0.03(-0.02)	(-0.11)	(0.03)

The G, SH, and LH responses modulate how effectively surface temperature (i.e., LW↑) responds to the radiative influence of the forcing terms. ERA-I has a larger than observed response of G throughout the annual cycle, reducing the LW↑ response. In contrast, CFSv2's G response is less than observed and CESM's G response is greater than observed in summer (-9%) and less than observed in winter (11%). During summer the ERA-I SH response is within 4% of observations, while in winter the positive SH response to changes in the forcing terms leads to 41% less compensation than observed. Thus, the difference in the ERA-I winter SH response offsets the difference in the G response. Both CFSv2 and CESM over-estimate the SH response throughout the annual cycle, effectively limiting the surface temperature responses to changes in radiative forcing. The differences in the LH responses are comparatively small for the one year data set, where the biggest difference is in the summer CFSv2 (8% more responsive). The differences of the LH responses are larger when comparing the extended data sets, suggesting that if the observed

LH responses in 2012 are more typical than the summer consisting of July – August 2013 and June 2014, then summer LH response plays a larger role in limiting modeled surface temperature variability.

Generally, the representation of the ground heat flux response is important because it provides the most compensation to changes in radiative forcing. CESM, a coupled climate model, provides the most realistic G response because it has the most advanced representation of snow properties and thus, more dynamic surface and subsurface interactions. The CESM model run used in this study (a candidate for CESM2) uses a vertically resolved land surface model to represent snow compaction of the ice sheet firn and allow for changes in snow density based on temperature and wind speed (Jan Lenaertz 2017, personal communication). In contrast, ERA-I has only one snow layer with a constant density, resulting in strong coupling between the atmosphere and the GIS due snow pack being too thermally active (Dutra et al., 2015). CFSv2 is similar to ERA-I in that it uses a simple snow layer model but in the case of CFSv2 the result is a small response of G. In the CFSv2 Noah land surface model the ground heat flux is estimated from the temperature gradient from the surface to a depth below the snowpack, which at Summit is $\approx$1.3 m below the surface, resulting in very little heat conduction through this thick layer.

Representation of surface albedo is important because it directly effects the amount of radiative forcing at the surface by determining the amount of shortwave radiation absorbed by the surface. In ERA-I it is set to a globally representative value for snow of about 0.8. CFSv2 surface albedo is about 0.84 with some dependence on solar zenith angle in March and September. CESM has the most seasonal and monthly variability indicating an ability to respond to changes in solar zenith angle and cloud presence. Accurate representation of surface albedo in combination with representative downwelling radiation yields the most realistic modeled radiative forcing.

SH and LH are directly linked to boundary-layer stability and the associated small-scale turbulent features. Model implementation of scaling parameterizations of eddy diffusivity for stable boundary-layers vary widely across models (Holtslag et al., 2013). In addition to differences of surface layer parameterizations, discrepancies of modeled turbulent heat flux values could be the

result of differences in low-level wind speed, vertical resolution of the models, and assumptions for roughness length values (Cassano et al., 2001).

4.5 Conclusion

A comprehensive set of observations at Summit Station is used to evaluate a trio of modeling approaches. A reanalysis, an operational forecast model, and a global climate model all produce an annual mean warm bias of surface temperature. Monthly statistics and seasonal biases of each SEB component help discern the major contributors to discrepancies of modeled surface temperatures. Model evaluation utilizing process-based relationships focuses on evaluating how realistically SH, LH, and G modulate changes in radiative forcing. This approach separates the evaluation of radiative forcing, mainly driven by variability in clouds and/or insolation, from evaluation of the surface energy exchange via ice sheet/atmosphere coupling.

Realistic representation of surface temperatures at Summit Station would provide confidence in modeled temperatures across the central GIS, which would in turn give confidence in the model's ability to represent GIS melt extent. Ideally, modeled surface temperature biases would be low due to accurate representation of downwelling radiation, surface albedo, and realistic responses of the SEB terms to radiative forcing. Offsetting biases of various SEB components often combine to produce surface temperatures that compare decently with observations on monthly or annual time scales. The physical coupling of the GIS and the atmosphere is manifested in the ground heat flux response, which is an important modulating factor of the surface temperature response to radiative forcing. For ice sheet modeling it is advantageous to have a multi-layer representation of snowpack, preferably with environmentally dependent snow properties. It is likely that an improved accounting of the ground heat flux variability would also improve the representation of SH, LH and their associated responses to radiative forcing via a more realistic representation of stability within the boundary layer (i.e., colder surface temperatures could weaken turbulent mixing.)

Accurately representing the observed physical processes is import for models of all types, even though they are forced and/or constrained in different ways. For example, it is imperative to under-

stand the limitations associated with a reanalysis product before utilizing it force another model or study a climate process. In Greenland, for example, a summer warm(cold) surface temperature bias would lead to an over(under)-estimation of past surface melt extent, an albedo that was too low would lessen a summer warming trend due to an increase in cloud cover, and near-surface stability that was too weak would enhance the exchange of water vapor at the surface. Climate models are also dependent on accurate representation of physical processes so that feedback mechanisms might be reasonably represented for a changing Arctic. One consequence of warmer atmospheric temperatures in the future is that once surface temperatures reach the melting point the surface temperature no longer responds to changes to radiative forcing. When surface temperatures are limited to 0°C the modulating response of LH, SH, and G are altered and ultimately control the degree to which changes in radiative forcing impact melt.

Chapter 5

Conclusion

Over the past decade surface melt processes account for at least half of the amalgamated Greenland Ice Sheet (GIS) mass loss (van den Broeke et al., 2009), which contributes approximately 0.63 – 0.74 $mm\,yr^{-1}$ to global sea level rise (Enderlin et al., 2014; McMillan et al., 2016). The annual GIS surface temperatures are increasing in recent decades (McGrath et al., 2013), suggesting that variations of surface energy fluxes are consequential in determining melt extent, especially during episodes of meridional flow from the south resulting in warm air advection over central Greenland. Comprehensive measurements at Summit, Greenland provide the process-based understanding necessary to evaluate the key drivers and regulators of central GIS surface temperature and surface energy budget variability. In this dissertation a complete annual perspective of ice sheet/atmosphere interactions is presented to examine the forcing and responses of the surface energy budget and evaluate modeled surface temperatures often occurring in a stable boundary layer.

5.1 Cloud Radiative Forcing

Low-level stability, affected by both thermodynamic and dynamic processes, influences the degree to which the overlying atmosphere interacts with the surface. Radiational cooling to space is typical at the surface in central Greenland because solar heating is minimized due to a high shortwave albedo and thermal emission is maximized due to the high emissivity of the snow surface. On average, from September 2013 – March 2014 the surface at Summit was colder than the

atmosphere aloft (500 m) and snow below (-1 m) resulting in the surface being the coldest point in the near-surface (-2 to 20 m) temperature profile for 46% of the year. In addition, Miller et al. (2013) show that temperatures often increase with height above the GIS surface (72% occurrence during 2011) inhibiting vertical mixing in the boundary layer. Bulk Richardson number estimates reveal that in the absence of high winds ($> 8\ m\ s^{-1}$) to facilitate mechanical mixing of the boundary layer, instability rarely occurs without a combination of insolation and liquid-bearing clouds.

Liquid-bearing clouds affect the radiation balance at the surface by increasing the downwelling longwave radiation (LW) and decreasing the downwelling shortwave radiation (SW) compared to an equivalent clear-sky scene. The radiative impact of clouds on the surface, or cloud radiative forcing (CRF), is found to be dependent on liquid water path (LWP), solar zenith angle (SZA), and vertically integrated ice cloud thickness. For LWP greater than 30 $g\,m^{-2}$ a cloud is opaque in the infrared resulting in a mean longwave CRF value of 85 $W\,m^{-2}$ at Summit. The ability of liquid-bearing clouds to reduce the net shortwave radiation is limited by the high surface albedo, confined SZA, and the rarity of LWP values greater than 100 $g\,m^{-2}$ such that the magnitude of maximum shortwave cooling is approximately 65 $W\,m^{-2}$. Similar to liquid-bearing clouds, LW CRF warming by ice-clouds dominates the SW cooling effect, though CRF for ice-only clouds is found to have a linear dependance on vertically integrated cloud thickness. Thus, it is found that total CRF is positive for all months and 98.5% of all 3-hour averaged data indicates that clouds act to radiatively warm the surface.

From January 2011 – October 2013 clouds radiatively warmed the surface by an annual average of 33 $W\,m^{-2}$, although the magnitude of CRF varied with solar presence, cloud occurrence, and cloud phase. There was no clear annual cycle of cloud occurrence (86% on average) nor integrated cloud thickness (2.5 km on average), indicating that variability of liquid-bearing cloud presence and insolation is what largely drives the annual cycle of CRF. The fractional occurrence of liquid-bearing clouds is less than 10% from February – April and more than 60% during July and August and corresponds to the annual cycle of longwave CRF. The annual cycle of surface-based inversion occurrence and intensity are at a minimum in July and August, indicating that

the combination of solar heating and positive CRF increase surface temperatures, diminish the near-surface temperature gradient, and decrease boundary layer stability.

5.2 Responses of the surface energy budget

Clouds and/or insolation are the key drivers of the radiative balance at the surface, which in turn affects the physical exchange of energy between the subsurface, surface, and overlying atmosphere. The surface energy budget (SEB) provides a framework to account for all surface energy fluxes that ultimately impact the surface temperature. At Summit the SEB includes radiative, turbulent sensible heat (SH), turbulent latent heat (LH), and ground heat (G) fluxes. All components of the SEB were estimated for 75% of an annual cycle, spanning July 2013 – June 2014, achieving closure to within 1 $W\,m^{-2}$ annually with less than ± 8 $W\,m^{-2}$ for monthly residuals. Monthly diurnal cycles and case studies using 30-minute averaged SEB components indicate that the net radiative flux at the surface is anti-correlated with sensible, latent, and conductive heat fluxes suggesting there is a forcer-responder relationship.

Process-based relationships are developed in order to quantify the impact of downwelling radiation on surface temperature and characterize the modulating effects of the turbulent and ground heat fluxes. Over the annual cycle the response terms (SH + LH + G - upwelling LW) completely account for changes in the forcing terms (downwelling LW + net SW), indicating that the SEB is predominantly radiatively driven. The highly emissive GIS surface efficiently absorbs most downwelling longwave radiation and about 13% of the downwelling shortwave radiation. Over time the surface temperature increases in response to positive radiative forcing, the temperature gradient between the surface and subsurface adjusts, and the resultant change in the ground heat flux opposes the surface warming. Annually the ground heat response to radiative forcing is about 16%, with the greatest response in the winter due to denser snowpack and colder subsurface temperatures. The sensible heat flux response (9-11%) does not have an annual cycle due to offsetting increases(decreases) of near-surface temperature gradients and suppressed(enhanced) turbulent heat exchange during stable(unstable) winter(summer) conditions. The latent heat flux response is

negligible, except during summer when the amount of available moisture is greatest and unstable conditions are more frequent. The upwelling longwave response, a proxy for surface temperature response, to changes in radiative forcing is weaker in the summer (50-60%) compared to winter (65-85%), indicating that clouds have a larger impact on surface temperature variability in winter compared to summer.

The total impact of clouds on the surface energy budget is estimated by combining statistically derived response relationships with the instantaneous radiative effect of the clouds in the context of a given atmospheric profile (a.k.a, CRF). The effect of moving from a clear-sky to cloudy scene, or vice versa, is to change the radiative flux at the surface and over time induce a change in surface temperature, the linchpin that determines ice sheet/atmosphere physical interactions. It is estimated that the annual CRF value of 32.9 $W\,m^{-2}$ is apportioned such that 7.2 $W\,m^{-2}$ are allocated for increasing subsurface temperatures and 3.0 and 0.2 $W\,m^{-2}$ are allocated to directly heat the atmosphere via the turbulent sensible and latent heat fluxes, respectively. The resultant annual mean response of 23.4 $W\,m^{-2}$ allocated to the upwelling longwave component suggests that clouds warm the surface by 7.8°C annually (during January 2011 – October 2013) with minimum cloud warming of the surface from April – June and maximum warming from October – February.

5.3 Model evaluation

Ground-based observations are useful for validating modeling tools that can be utilized to represent much greater spatial and temporal extents. Hence, SEB observations are used to evaluate various modeling perspectives, including a reanalysis product (ERA-I), an operational model (CFSv2), and a climate model (CESM). It might be expected that deficiencies of modeled occurrence of liquid-bearing clouds would produce an annual surface temperature bias of as much as -7.8°C. To the contrary, ERA-I has significant deficiencies in downwelling longwave radiation due to a deficiency in liquid water path, yet ERA-I has an annual warm bias in surface temperature. In summer the ERA-I warm bias is due to a surface albedo that is 6-9% lower than observed and in winter a positive bias in the SH leads to warmer surface temperatures. Downwelling longwave

radiation is also under-represented in CRFv2 and the surface albedo is approximately 2-3% lower than observed, resulting in the radiative forcing being too low throughout most of the annual cycle. A positive bias of SH in CFSv2 annually and during CESM winter offsets deficiencies in radiative forcing. CESM summer best represents liquid-bearing clouds, downwelling longwave radiation, SH and surface albedo, resulting in a relatively small positive bias in the forcing terms and surface temperature.

The distillation of fundamental ice sheet/atmosphere interactions into process-based relationships are useful in deciphering possible areas for model improvement, independent from known challenges in representing mixed-phase clouds. In ERA-I, strong coupling between the atmosphere and the snowpack reduces the surface temperature variability, limiting the representation of extremely cold surface temperatures observed in winter. In summer, stronger than observed forcing due to a low surface albedo is limited by the overactive ground heat flux response, resulting in a warm bias of modeled surface temperatures. CFSv2 has very little ground heat flux response, suggesting that the surface should be able to respond drastically to radiative forcing. Yet the CFSv2 SH response over-compensates for changes in radiative forcing, limiting the surface temperature response. CESM also overestimates the SH response, but has a relatively accurate ground heat flux response.

Evaluating models with this unique process-based approach provides a pathway to isolate an improper representation of a physical interaction from issues associated with determining how much radiation is transferred to the surface via atmospheric processes. Simply evaluating the monthly mean values of ground heat flux could be misleading because even though the observed monthly values of ground heat flux are small the ground heat flux response is an important consideration for capturing surface temperature variability. Modeling the subsurface with a multi-layer snow scheme allows for the most accurate estimate of the ground heat flux response of the three models that were evaluated. In addition, summertime SH variability might be larger(smaller) than observed due to too much(little) radiative forcing, rather than modeled SH responses being physically unrealistic. Further studies are needed to determine the reasons for discrepancies of the SH or LH response,

as they could be related to the representation of the boundary layer stability parameters or other environmental conditions.

5.4 Implications for current and future research

The overlapping nature of various field campaigns provides a comprehensive observational record at Summit, Greenland. Capitalizing on this synergy, this dissertation achieves the following objectives,

(1) Quantify the impact of clouds on surface radiation.

(2) Discern how the coupled ice sheet/atmosphere system adjusts to changes in radiative forcing via estimates of the full surface energy budget.

(3) Provide a framework to evaluate modeled surface temperatures utilizing observed SEB components and process-based relationships.

Scientific understanding gleaned from results contained in this dissertation have broad value in advancing science related to the GIS. Moreover, substantive observations present a solid foundation upon which to collaborate with other related studies to expand scientific understanding.

Quality ground-based observations provide a fixed location with which to validate cloud properties as represented by models and space-borne instruments that have greater spatial capabilities. The observations detailed in this dissertation have been used to identify deficiencies of cloud properties above Summit, Greenland in the last publicly released version of CESM. Kay et al. (2016a) provide scale-aware and definition-aware CESM comparisons to Cloud-Aerosol Lidar and Infrared Pathfinder Satellite Observation (CALIPSO) satellite observations, indicating that there is a deficit of liquid-bearing clouds above the GIS. Comparing liquid water paths in CESM to ground-based observations, it was found that even when liquid-bearing clouds occur, the amount of liquid present is so small that the radiational effect on the surface is negligible, resulting in a cold bias in summer daily maximum surface temperature of 2-3°C. McIlhattan et al. (2017) report that compared to

Summit observations the CESM downwelling LW bias is -24 $W\,m^{-2}$ and a CloudSat/CALIPSO satellite product reproduces the annual cycle of observed downwelling LW with an annual average bias of only -3 $W\,m^{-2}$. In addition, the CloudSat/CALIPSO observations represent the frequency of occurrence of liquid-bearing clouds to within 3%. Thus, Summit observations validate the ability of space-borne products to report and represent factors that determine downwelling longwave radiation, providing confidence in Greenland-wide results.

Van Tricht et al. (2016) utilize a satellite-climate model hybrid approach to estimate the impact of clouds in the surface mass balance. At Summit there is agreement with ground-based observations, reporting only a slightly lower (-3 $W\,m^{-2}$) annual CRF and they are able to capture the seasonal cycle of CRF. Expanding their results to the entire GIS, it is estimated that ice-only and liquid-bearing clouds contribute equally to decreasing the GIS surface mass balance (152 ± 20 $Gt/year$) by enhancing sublimation, increasing surface melt and limiting the amount of refreezing that would otherwise occur under clear-sky conditions.

The detailed Summit observations may also be used to investigate specific large-scale events. For example, Solomon et al. (2017) utilize regional model simulations to investigate the July 2012 GIS melt event, which resulted in surface melt at Summit station for the first time since 1889. Ground-based observations of cloud properties and SEB fluxes validated the ability of the state-of-the-art model to represent cloud microphysics and the associated impacts on the SEB. Subsequently, a sensitivity study investigates the state of the system without the radiative interaction of clouds, illuminating the importance of representing the SEB responses to clouds when modeling melt processes. When investigating SEB feedbacks in specific case studies, such as by Solomon et al. (2017), direct observations are invaluable for providing confidence in the model output.

The results of this dissertation are primed to evaluate the next publicly available version of the Community Earth System Model (CESM2) after its upcoming release. It is anticipated that the improved ability to represent cloud and snow properties in central Greenland will enhance the ability to project future changes to the GIS surface mass balance under various representative greenhouse gas concentration pathway scenarios by more realistically representing cloud radiative forcing and

ground heat flux response. The expected ability of CESM2 to represent forcing terms and surface temperature response to radiative forcing would place credence in the use of this powerful tool for controlled experiments in investigating the fate of the GIS.

Changes within the Arctic climate system pose challenges to the modeling community, requiring realistic representation of feedback processes, that include the effects of changes to atmospheric heat transport, surface albedo, and cloud cover. Modeled surface temperatures that capture the mean state of the system, but have offsetting biases of individual SEB components, will not be able to forecast/predict extreme events or adjustments in the system on various time scales. The observational community must not only strive to provide quality measurements useful for validation but must also convey the essence of land/ice/ocean/atmosphere interactions to support the development of more representative parameterizations in models. In turn, models can be used to expose sensitivities of the climate system to an under-observed, and consequently poorly constrained process, and contextualize short observational records within the variability in the climate system (Kay et al., 2016b). Building off of past observational achievements and model insights this body of work provides a straight-forward and quantitive approach to reciprocally advance our understanding of the Greenland Ice Sheet.

Bibliography

M. R. Albert and W. R. McGilvary. Thermal effects due to air flow and vapor transport in dry snow. J. Glaciology, 38(129):273–281, 1992.

M. R. Albert and E. F. Shultz. Snow and firn properties and air-snow transport processes at Summit, Greenland. Atmospheric Environment, 36:2789–2797, 2002.

B. Albrecht and S. K. Cox. Procedures for improving pyrgeometer performance. J. Appl. Meteorol., 16:188–197, 1977.

R. B. Alley. The two-mile time machine. Princeton University Press, 2000.

E. L. Andreas, R. E. Jordan, and A. P. Makshtas. Parameterizing turbulent exchange over sea ice: the ice station Weddell results. Boundary-Layer Meteorol., 114:439–460, 2005.

A. Bailey, D. Noone, M. Berkelhammer, H. C. Steen-Larsen, and P. Sato. The stability and calibration of water vapor isotope ratio measurements during long-term deployments. Atmos. Meas. Tech., 8:4521–4538, 2015. doi: 10.5194/amt-8-4521-2015.

R. Bennartz, M. D. Shupe, D. D. Turner, V. P. Walden, K. Steffen, C. J. Cox, M. S. Kulie, N. B. Miller, and C. Pettersen. July 2012 Greenland melt extent enhanced by low-level liquid clouds. Nature, 496:83–86, 2013. doi: 10.1038/nature12002.

M. Berkelhammer, D. C. Noone, H. C. Steen-Larsen, A. Bailey, C. J. Cox, M. S. O'Neill, D. Schneider, K. Steffen, and J. W. C. White. Surface-atmosphere decoupling limits accumulation at Summit, Greenland. Sci. Adv., 2(4):1–9, 2016. doi: 10.1126/sciadv.1501704.

R. C. Boeke and P. C. Taylor. Evaluation of the Arctic surface radiation budget in CMIP5 models. J. Geophys. Res. Atmos., 121:8525–8548, 2016. doi: 10.1002/2016JD025099.

C. Saskia Bourgeois. The radiative properties of snow at Summit, Greenland. PhD thesis, Swiss Federal Institute of Technology (ETH), 2006.

J. E. Box. Greenland ice sheet mass balance reconstruction. Part II: Surface mass balance (1840-2010). J. Climate, 26:6974–6989, 2013. doi: 10.1175/JCLI-D-12-00518.1.

J. E. Box and K. Steffen. Sublimation on the Greenland ice sheet from automated weather station observations. J. Geophys. Res., 106(D24):33965–33981, 2001.

J. E. Box, X. Fettweis, J. C. Stroeve, M. Tedesco, D. K. Hall, and K. Steffen. Greenland ice sheet albedo feedback: Thermodynamics and atmospheric drivers. The Cryosphere, 6:821–839, 2012. doi: 10.5194/tc-6-821-2012.

R. S. Bradley and F. T. Keimig. Climatology of surface-based inversions in the North American Arctic. J. Geophys. Res., 97(D14):15699–15712, 1992.

J. R. Campbell, D. L. Hlavka, E. J. Welton, C. J. Flynn, D. D. Turner, J. D. Spinhirne, V. S. Scott III, and I. H. Hwang. Full-time, eye-safe cloud and aerosol lidar observation at atmospheric radiation measurement program sites: Instruments and data processing. J. Atmos. Oceanic Technol., 19:431–442, 2002.

J. J. Cassano, T. R. Parish, and J. C. King. Evaluation of turbulent surface flux parameterizations for the stable surface layer over Halley, Antarctica. Mon. Wea. Rev., 129:26–46, 2001. doi: 10.1175/1520-0493(2001)129⟨0026:EOTSFP⟩2.0.CO;2.

G. Cesana, J. E. Kay, H. Chepfer, J. M. English, and G. de Boer. Ubiquitous low-level liquid-containing Arctic clouds: New observations and climate model constraints from CALIPSO-GOCCP. Geophys. Res. Lett., 39(L20804), 2012. doi: 10.1029/2012GL053385.

C. Charalampidis, D. van As, J. E. Box, M. R. van den Broeke, W. T. Colgan, S. H. Doyle, A. L. Hubbard, M. MacFerrin, H. Machguth, and C. J. P. P. Smeets. Changing surface-atmosphere energy exchange and refreezing capacity of the lower accumulation area, West Greenland. The Cryosphere, 9:2163–2181, 2015. doi: 10.5194/tc-9-2163-2015.

M. W. Christensen, A. Behrangi, T. S. L'Ecuyer, N. B. Wood, M. D. Lebsock, and G. L. Stephens. Arctic observation and reanalysis integrated system: A new data product for validation and climate study. Bull. Amer. Meteor. Soc., 97(6):907–915, 2016. doi: 10.1175/BAMS-D-14-00273.1.

S.A. Clough, M.W. Shephard, E.J. Mlawer, J.S. Delamere, M.J. Iacono, K. Cady-Pereira, S. Boukabara, and P.D. Brown. Atmospheric radiative transfer modeling: A summary of the AER codes. J. Quant. Spectrosc. Radiat. Transfer, 91:233–244, 2005.

L. Cohen, D. Helmig, W. D. Neff, A. A. Grachev, and C. W. Fairall. Boundary-layer dynamics and its influence on atmospheric chemistry at Summit, Greenland. Atmospheric Environment, 41:5044–5060, 2007.

J. C. Comiso and D. K. Hall. Climate trends in the Arctic as observed from space. WIREs Clim. Change, 5:389–409, 2014. doi: 10.1002/wcc.277.

C. J. Cox, V. P. Walden, G.P. Compo, P.M. Rowe, M. D. Shupe, and K. Steffen. Downwelling longwave flux over Summit, Greenland, 2010-2012: Analysis of surface-based observations and evaluation of ERA-Interim using wavelets. J. Geophys. Res. Atmos., 119:12317–12337, 2014. doi: 10.1002/2014JD021975.

C. J. Cox, V. P. Walden, P. M. Rowe, and M. D. Shupe. Humidity trends imply increased sensitivity to clouds in a warming Arctic. Nature Communications, 6(10117):1–8, 2015. doi: 10.1038/ncomms10117.

S. Crewell and U. Löhnert. Accuracy of cloud liquid water path from ground-based microwave radiometry 2. Sensor accuracy and synergy. Radio Sci., 38(3):8042, 2003.

N. J. Cullen. Characteristics of the atmospheric boundary layer at Summit, Greenland. PhD thesis, University of Colorado, 2003.

N. J. Cullen and K. Steffen. Unstable near-surface boundary conditions in summer on top of the Greenland ice sheet. Geophys. Res. Lett., 28:4491–4493, 2001.

N. J. Cullen, K. Steffen, and P. D. Blanken. Nonstationarity of turbulent heat fluxes at Summit, Greenland. Boundary-Layer Meteorol., 122:439–455, 2007.

N. J. Cullen, T. Mölg, J. Conway, and K. Steffen. Assessing the role of sublimation in the dry snow zone of the Greenland ice sheet in a warming world. J. Geophys. Res. Atmos., 119:6563–6577, 2014. doi: 10.1002/2014JD021557.

J. A. Curry and E. E. Ebert. Annual cycle of radiation fluxes over the Arctic Ocean: Sensitivity to cloud optical properties. J. Climate, 5:1267–1280, 1992.

J. A. Curry and G. F. Herman. Infrared radiative properties of summertime Arctic stratus clouds. J. Climate Appl. Meteor., 24:525–538, 1985.

J. A. Curry, F. G. Meyer, L. F. Radke, C. A. Brock, and E. E. Ebert. Occurrence and characteristics of lower tropospheric ice crystals in the Arctic. Int. J. Climatol., 10:749–764, 1990.

W. Dansgaard, S. J. Johnsen, H. B. Clausen HB, D. Dahljensen, NS N. S. Gundestrup, C. U. Hammer, C. S. Hvidberg, J. P. Steffensen, A. E. Sveinbjörnsdottir, J. Jouzel, and G. Bond. Evidence for general instability of past climate from a 250-kyr ice-core record. Nature, 364: 218–220, 1993. doi: 10.1038/364218a0.

G. de Boer, E. W. Eloranta, and M. D. Shupe. Arctic mixed-phase stratiform cloud properties from multiple years of surface-based measurements at two high-latitude locations. J. Atmos. Sci., 66: 2874–2887, 2009. doi: 10.1175/2009JAS3029.1.

G. de Boer, W. D. Collins, S. Menon, and C. N. Long. Using surface remote sensors to derive radiative characteristics of mixed-phase clouds: an example from M-PACE. Atmos. Chem. Phys., 11:11,937–11,949, 2011. doi: 10.5194/acp-11-11937-2011.

D. P. Dee, S. M. Uppala, A. J. Simmons, P. Berrisford, P. Poli, S. Kobayashi, U. Andrae, M. A. Balmaseda, G. Balsamo, P. Bauer, P. Bechtold, A. C. M. Beljaars, L. van de Berg, J. Bidlot, N. Bormann, C. Delsol, R. Dragani, M. Fuentes, A. J. Geer, L. Haimberger, S. B. Healy, H. Hersbach, E. V. Hólm, L. Isaksen, P. Kallberg, M. Köhler, M. Matricardia, A. P. McNally, B. M. Monge-Sanz, J.-J. Morcrette, B.-K. Park, C. Peubey, P. de Rosnay, C. Tavolato, J.-N. Thépaut, and F. Vitart. The ERA-Interim reanalysis: configuration and performance of the data assimilation system. Q. J. R. Meteor. Soc., 137:553–597, 2011. doi: 10.1002/qj.828.

E. J. Dlugokencky, P.M. Lang, K.A. Masarie, A.M. Crotwell, and M.J. Crotwell. Atmospheric carbon dioxide dry air mole fractions from the NOAA ESRL Carbon Cycle Cooperative Global Air Sampling Network, 1968-2013, Version: 2014-06-27, 2014. [Path: ftp://aftp.cmdl.noaa.gov/data/trace_gases/co2/flask/surface/].

X. Dong, B. Xi, K. Crosby, C. N. Long, R. S. Stone, and M. D. Shupe. A 10 year climatology of Arctic cloud fraction and radiative forcing at Barrow, Alaska. J. Geophys. Res., 115(D17212), 2010. doi: 10.1029/2009JD013489.

C. Drüe and G. Heinemann. Characteristics of intermittent turbulence in the upper stable boundary layer over Greenland. Boundary-Layer Meteorol., 124:361–381, 2007. doi: 10.1007/s10546-007-9175-8.

M. Dumont, E. Brun, G. Picard, M. Michou, Q. Libois, J-R. Petit, M. Geyer, S. Morin, and B. Josse. Contribution of light-absorbing impurities in snow to Greenland's darkening since 2009. Nature Geoscience, 7:509–512, 2014. doi: 10.1038/NGEO2180.

E. Dutra, I. Sandu, G. Balsamo, A. Beljaars, H. Freville, E. Vignon, and E. Brun. Understanding the ECMWF winter surface temperature biases over Antarctica. ECMWF Technical Memoranda No. 762, European Centre for Medium-Range Weather Forecasts, 2015.

E. M. Enderlin, I. M. Howat, S. Jeong, M. Noh, J. H. van Angelen, and M. van den Broeke. An improved mass budget for the Greenland Ice Sheet. Geophys. Res. Lett., 41:866–872, 2014. doi: 10.1002/2013GL059010.

C. W. Fairall, E. F. Bradley, D. P. Rogers, J. B. Edson, and G. S. Young. Bulk parameterization of air-sea fluxes for Tropical Ocean-Global Atmosphere Coupled-Ocean Atmosphere Response Experiment. J. Geophys. Res., 101:3747–3764, 1996.

X. Fettweis, B. Franco, M. Tedesco, J. H. van Angelen, J. T. M. Lenaerts, M. R. van den Broeke, and H. Gallée. Estimating the Greenland ice sheet surface mass balance contribution to future sea level rise using the regional atmospheric climate model MAR. The Cryosphere, 7:469–489, 2013a. doi: 10.5194/tc-7-469-2013.

X. Fettweis, E. Hanna, C. Lang, A. Belleflamme, M. Erpicum, and H. Gall. Brief communication "Important role of the mid-tropospheric atmospheric circulation in the recent surface melt increase over the Greenland ice sheet". The Cryosphere, 7:241–248, 2013b. doi: 10.5194/tc-7-241-2013.

M. F. Fitzpatrick and S. G. Warren. Transmission of solar radiation by clouds over snow and ice surfaces. Part II: Cloud optical depth and shortwave radiative forcing from pyranometer measurements in the Southern Ocean. J. Climate, 18:4637–4648, 2005.

T. Foken. The energy balance closure problem: An overview. Ecological Applications, 140(6): 1351–1367, 2008.

J. A. Francis and S. J. Vavrus. Evidence linking Arctic amplification to extreme weather in mid-latitudes. Geophys. Res. Lett., 39:1–6, 2012. doi: 10.1029/2012GL051000.

J. G. Fyke, M. Vizcaíno, and W. H. Lipscomb. The pattern of anthropogenic signal emergence in Greenland Ice Sheet surface mass balance. Geophys. Res. Lett., 41:6002–6008, 2014. doi: 10.1002/2014GL060735.

A. Gettelman and H. Morrison. Advanced two-moment bulk microphysics for global models. Part I: Off-line tests and comparison with other schemes. J. Climate, 28:1268–1287, 2015. doi: 10.1175/JCLI-D-14-00102.1.

A. A. Grachev, C. W. Fairall, P.O.G. Persson, E. J. Andreas, and P. S. Guest. Stable boundary-layer scaling regimes: The SHEBA data. Boundary-Layer Meteor., 116:201–235, 2005. doi: 10.1007/s10546-004-2729-0.

A. A. Grachev, E. L. Andreas, C. W. Fairall, P. S. Guest, and P. O. G. Persson. The critical Richardson number and limits of applicability of local similarity theory in the stable boundary layer. Boundary-Layer Meterorol., 147:51–82, 2013. doi: 10.1007/s10546-012-9771-0.

Jonathan M. Gregory, Philippe Huybrechts, and S. C. B. Raper. Climatology: Threatened loss of the Greenland ice-sheet. Nature, 428:616–616, 2004. doi: 10.1038/428616a.

T. C. Grenfell, D. K. Perovich, and J. A. Ogren. Spectral albedos of an alpine snowpack. Cold Reg. Sci. Technol., 4:121–127, 1981.

J. Gröbner, I. Reda, S. Wacker, S. Nyeki, K. Behrens, and J. Gorman. A new absolute reference for atmospheric longwave irradiance measurements with traceability to SI units. J. Geophys. Res. Atmos., 119:7083–7090, 2014. doi: 10.1002/2014JD021630.

D. K. Hall, J. C. Comiso, N. E. DiGirolamo, C. A. Shuman, J. E. Box, and L. S. Koenig. Variability in the surface temperature and melt extent of the Greenland ice sheet from MODIS. Geophys. Res. Lett., 40:2114–2120, 2013. doi: 10.1002/grl.50240.

Y. Han and E. R. Westwater. Analysis and improvement of tipping calibration for ground-based microwave radiometers. IEEE Trans. Geosci. Remote Sens., 38(3):1260–1276, 2000.

E. Hanna, P. Huybrechts, K. Steffen, J. Cappelen, R. Huff, C. Shuman, T. Irvine-Fynn, S. Wise, and M. Griffiths. Increased runoff from melt from the Greenland ice sheet: A response to global warming. J. Climate, 21:331–341, 2008. doi: 10.1175/2007JCLI1964.1.

E. Hanna, X. Fettweis, S. H. Mernild, J. Cappelen, M. H. Ribergaard, C. A. Shuman, K. Steffen, L. Wood, and Thomas L. Mote. Atmospheric and oceanic climate forcing of the exceptional Greenland ice sheet surface melt in summer 2012. Int. J. Climatol., 34:1022–1037, 2014. doi: 10.1002/joc.3743.

J. Hansen, D. Johnson, A. Lacis, S. Lebedeff, P. Lee, D. Rind, and G. Russell. Climate impact of increasing atmospheric carbon dioxide. Science, 213:957–966, 1981. doi: 10.1126/science.213.4511.957.

M. E. Hauer, J. M. Evans, and D. R. Mishra. Millions projected to be at risk from sea-level rise in the continental United States. Nature Climate Change, 6:691–695, 2016. doi: 10.1038/nclimate2961.

D. Helmig, L. D. Cohen, F. Bocquet, S. Oltmans, A. Grachev, and W. Neff. Spring and summertime diurnal surface ozone fluxes over the polar snow at Summit, Greenland. Geophys. Res. Lett., 36: L08809, 2009. doi: 10.1029/2008GL036549.

A. Henderson-Sellers and K. McGuffie. Basis for integration of conventional observations of cloud into global nephanalyses. J. Atmos. Chem., 11:1–25, 1990.

S. W. Hoch. Radiative flux divergence in the surface boundary layer. PhD thesis, Swiss Federal Institute of Technology (ETH), 2005.

S. W. Hoch, P. Calanca, R. Philipona, and A. Ohmura. Year-round observation of longwave radiative flux divergence in Greenland. J. Appl. Meteor. Climatol., 46:1469–1479, 2007. doi: 10.1175/JAM2542.1.

M. M. Holland and C. M. Bitz. Polar amplification of climate change in coupled models. Clim. Dynam., 21:221–232, 2003.

A. A. M. Holtslag, G. Svensson, P. Baas, S. Basu, B. Beare, A. C. M. Beljaars, F. C. Bosveld, J. Cuxart, J. Lindvall, G. J. Steeneveld, M. Tjernström, and B. J. H. van de Wiel. Stable atmospheric boundary layers and diurnal cycles: Challenges for weather and climate models. Bull. Amer. Meteor. Soc., 94(11):1691–1706, 2013. doi: 10.1175/BAMS-D-11-00187.1.

S. R. Hudson and R. E. Brandt. A look at the surface-based temperature inversion on the Antarctic plateau. J. Climate, 18:1673–1696, 2005.

J. Hurrell, M. M. Holland, and Coauthors. The community earth system model: a framework for collaborative research. Bull. Amer. Meteor. Soc., 94:1339–1360, 2013. doi: 10.1175/BAMS-D-12-00121.1.

J. M. Intrieri, C. W. Fairall, M. D. Shupe, P. O. G. Persson, E. L. Andreas, P. S. Guest, and R. E. Moritz. An annual cycle of Arctic surface cloud forcing at SHEBA. J. Geophys. Res., 107(C10), 2002. doi: 10.1029/2000JC000439.

IPCC. Climate Change 2013: The Physical Science Basis. Contribution of Working Group I to the Fifth Assessment Report of the Intergovernmental Panel on Climate Change. Cambridge University Press, Cambridge, United Kingdom and New York, NY, USA, 2013. ISBN ISBN 978-1-107-66182-0. doi: 10.1017/CBO9781107415324. URL `www.climatechange2013.org`.

R. Jordan. A one-dimensional temperature model for a snow cover: Technical documentation for SNTHERM.89. Special Rep. 91-16, U.S. Army Cold Reg. Res. and Eng. Lab., Hanover, N.H., 1991.

S. Kato, T. P. Ackerman, E. E. Clothiaux, J. H. Mather, G. G. Mace, M. L. Wesely, F. Murcray, and J. Michalsksy. Uncertainties in modeled and measured clear-sky surface shortwave irradiances. J. Geophys. Res., 102(D22):25,881–25,898, 1997.

J. E. Kay and T. L'Ecuyer. Observational constraints on Arctic Ocean clouds and radiative fluxes during the early 21st century. J. Geophys. Res., 118:1–18, 2013. doi: 10.1002/jgrd.50489.

J. E. Kay, L. Bourdages, N. B. Miller, A. Morrison, V. Yettella, H. Chepfer, and B. Eaton. Evaluating and improving cloud phase in the Community Atmosphere Model version 5 using spaceborne lidar observations. J. Geophys. Res. Atmos., 121:1–15, 2016a. doi: 10.1002/2015JD024699.

J. E. Kay, T. L'Ecuyer, H. Chepfer, N. Loeb, A. Morrison, and G. Cesana. Recent advances in Arctic cloud and climate research. Curr. Clim. Change Rep., 2:159–169, 2016b. doi: 10.1007/s40641-016-0051-9.

T. Konzelmann, R. S. W. van de Wal, W. Greuell, R. Bintanja, E. A. C. Henneken, and A. Abe-Ouchi. Parameterization of the global and longwave incoming radiation for the Greenland ice sheet. Global and Planetary Change, 9:143–164, 1994.

P. Kuipers Munneke, M. R. van den Broeke, C. H. Reijmer, M. M. Helsen, W. Boot, M. Schneebeli, and K. Steffen. The role of radiation penetration in the energy budget of the snowpack at Summit, Greenland. The Cryosphere, 3:155–165, 2009.

J. Liu, Z. Chen, J. Francis, M. Song, T. Mote, and Y. Hu. Has Arctic sea ice loss contributed to increased surface melting of the Greenland Ice Sheet? J. Climate, 29:3373–3386, 2016. doi: 10.1175/JCLI-D-15-0391.1.

Y. Liu, J. R. Key, and X. Wang. The influence of changes in cloud cover on recent surface temperature trends in the Arctic. J. Climate, 21:705–715, 2008.

Y. Liu, M. D. Shupe, Z. Wang, and G. Mace. Cloud vertical distribution from combined surface and space radar/lidar observations at two arctic atmospheric observations. Atmospheric Chemistry and Physics Discussions, 2017:1–28, 2017. doi: 10.5194/acp-2016-1132.

C. N. Long and T. P. Ackerman. Identification of clear skies from broadband pyranometer measurements and calculation of downwelling shortwave cloud effects. J. Geophys. Res., 105(D12): 15,609–15,626, 2000.

C. N. Long and D. D. Turner. A method for continuous estimation of clear-sky downwelling longwave radiative flux developed using ARM surface measurements. J. Geophys. Res., 113 (D18206), 2008. doi: 10.1029/2008JD009936.

R. A. McClatchey, R. W. Fenn, J. E. A. Selby, F. E. Volz, and J. S. Garing. Optical properties of the atmosphere. Rep. AFCRL-72-0497, Hanscom Air Force Base, Bedford, Mass., 1972.

D. McGrath, D. W. Colgan, N. Bayou, A. Muto, and K. Steffen. Recent warming at Summit, Greenland: Global context and implications. Geophys. Res. Lett., 40:2091–2096, 2013. doi: 10.1002/grl.50546.

E. A. McIlhattan, T. L'Ecuyer, and N. B. Miller. Observational evidence linking Arctic supercooled liquid cloud biases in CESM to snowfall processes. J. Climate, 2017.

M. McMillan, A. Leeson, A. Shepherd, K. Briggs, T. W. K. Armitage, A. Hogg, P. Kuipers Munneke, M. van den Broeke, B. Noël, W. J. van de Berg, S. Ligtenberg, M. Horwath, A. Groh, A. Muir, and L. Gilbert. A high-resolution record of Greenland mass balance. Geophys. Res. Lett., 43: 7002–7010, 2016. doi: 10.1002/2016GL069666.

S. H. Mernild, T. L. Mote, and G. E. Liston. Greenland ice sheet surface melt extent and trends: 1960-2010. Journal of Glaciology, 57:621–628, 2011.

N. B. Miller. Microwave radiometer observations of surface based inversions above the Greenland ice sheet. Master's thesis, University of Wisconsin – Madison, 2012.

N. B. Miller, D. D. Turner, R. Bennartz, M. D. Shupe, M. S. Kulie, M.P. Cadeddu, and V. P. Walden. Surface-based inversions above central Greenland. J. Geophys. Res. Atmos., 118:495–506, 2013. doi: 10.1029/2012JD018867.

N. B. Miller, M. D. Shupe, C. J. Cox, V. P. Walden, D. D. Turner, and K. Steffen. Cloud radiative forcing at Summit, Greenland. J. Climate, 28:6267–6280, 2015. doi: 10.1175/JCLI-D-15-0076.1.

N. B. Miller, M. D. Shupe, C. J. Cox, D. Noone, P. O. G. Persson, and K. Steffen. Surface energy budget responses to radiative forcing at summit, greenland. The Cryosphere, 11(1):497–516, 2017. doi: 10.5194/tc-11-497-2017.

L. M. Miloshevich, H. Vömel, D. N. Whiteman, and T. Leblanc. Accuracy assessment and correction of Vaisala RS92 radiosonde water vapor measurements. J. Geophys. Res., 114(D11305), 2009.

E. J. Mlawer, V. H. Payne, J.-L. Moncet, J. S. Delamere, M. J. Alvarado, and D. C. Tobin. Development and recent evaluation of the MT_CKD model of continuum absorption. Phil. Trans. R. Soc. A, 370:2520–2556, 2012.

K. P. Moran, B. E. Martner, M. J. Post, R. A. Kropfli, D. C. Welsh, and K. B. Widenerr. An unattended cloud-profiling radar for use in climate research. Bull. Amer. Meteor. Soc., 79:443–455, 1998.

H. Morrison and J. O. Pinto. Intercomparison of bulk cloud microphysics schemes in mesoscale simulations of springtime Arctic mixed-phase stratiform clouds. Monthly Weather Rev., 134: 1880–1900, 2006.

W. Neff, G. P. Compo, F. M. Ralph, and M. D. Shupe. Continental heat anomalies and the extreme melting of the Greenland ice surface in 2012 and 1889. J. Geophys. Res. Atmos., 119:6520–6536, 2014. doi: 10.1002/2014JD021470.

S. V. Nghiem, D. K. Hall, T. L. Mote, M. Tedesco, M. R. Albert, K. Keegan, C. A. Shuman, N. E. DiGirolamo, and G. Neumann. The extreme melt across the Greenland ice sheet in 2012. Geophys. Res. Lett., 39, 2012. doi: 10.1029/2012GL053611.

T. R. Oke. Boundary Layer Climates. University Press, Cambridge, 2nd edition, 1987.

J. E. Overland, J. A. Francis, E. Hanna, and M. Wang. The recent shift in early summer Arctic atmospheric circulation. Geophys. Res. Lett., 39:1–6, 2012. doi: 10.1029/2012GL053268.

P. O. G. Persson. Onset and end of the summer melt season over sea ice: thermal structure and surface energy perspective from SHEBA. Clim. Dyn., 39:1349–1371, 2012. doi: 10.1007/s00382-011-1196-9.

P. O. G. Persson, D. Ruffieux, and C. W. Fairall. Recalculations of pack ice and lead surface energy budgets during the Arctic Leads Experiment (LEADEX) 1992. J. Geophys. Res., 102: 25085–25089, 1997.

P. O. G. Persson, C. W. Fairall, E. L. Andreas, P. S. Guest, and D. K. Perovich. Measurements near the Atmospheric Surface Flux Group tower at SHEBA: Near-surface conditions and surface energy budget. J. Geophys. Res., 107(C10):8045, 2002. doi: 10.1029/2000JC000705.

C. Pettersen, R. Bennartz, M. S. Kulie, A. J. Merrelli, M. D. Shupe, and D. D. Turner. Microwave signatures of ice hydrometeors from ground-based observations above Summit, Greenland. Atmos. Chem. Phys., 16:4743–4756, 2016. doi: 10.5194/acp-16-4743-2016.

G. W. Petty. A first course in atmospheric radiation. Sundog Publishing, 2006.

W. H. Press, S. A. Teukolsky, W. T. Vetterling, and B. P. Flannery. Numerical Recipes in C: The Art of Scientific Computing. University Press, Cambridge, 2nd edition, 1992.

S. Rahmstorf, J. E. Box, G. Feulner, M. E. Mann A. Robinson, S. Rutherford, and E. J. Schaffernicht. Exceptional twentieth-century slowdown in atlantic ocean overturning circulation. Nature Climate Change, 5:475–480, 2015. doi: 10.1038/nclimate2554.

V. Ramanathan, R. D. Cess, E. F. Harrison, P. Minnis, B. R. Barkstrom, E. Ahmad, and D. Hartmann. Cloud-radiative forcing and climate: Results from the Earth Radiation Budget Experiment. Science, 243:57–63, 1989.

E. Rignot, I. Velicogna, M.R. van den Broeke, A. Monaghan, and J. Lenaerts. Acceleration of the contribution of the greenland and antarctic ice sheets to sea level rise. Geophys. Res. Lett., 38: L05503–L05508, 2011. doi: 10.1029/2011GL046583.

T. Rose, S. Crewell, U. Löhnert, and C. Simmer. A network suitable microwave radiometer for operational monitoring of the cloudy atmosphere. Atmos. Res., 75:183–200, 2005.

D. Ruffieux, P. O. G. Persson, C. W. Fairall, and Daniel E. Wolfe. Ice pack and lead surface energy budgets during LEADEX 1992. J. Geophys. Res., 100:4593–4612, 1995.

S. Saha, S. Moorthi, X. Wu, J. Wang, S. Nadiga, P. Tripp, D. Behringer, Y. Hou, H. Chuang, M. Iredell, M. Ek, J. Meng, R. Yang, M. P. Mendez, H. van den Dool, Q. Zhang, W. Wang, M. Chen, and E. Becker. The NCEP climate forecast system reanalysis. Bull. Amer. Meteor. Soc., 91:1015–1057, 2010.

S. Saha, S. Moorthi, X. Wu, J. Wang, S. Nadiga, P. Tripp, D. Behringer, Y. Hou, H. Chuang, M. Iredell, M. Ek, J. Meng, R. Yang, M. P. Mendez, H. van den Dool, Q. Zhang, W. Wang, M. Chen, and E. Becker. The NCEP Climate Forecast System Version 2. J. Climate, 27:2185–2208, 2014. doi: 10.1175/JCLI-D-12-00823.1.

D. Schröder, D. L. Feltham, D. Flocco, and Michel Tsamados. September Arctic sea-ice minimum predicted by spring melt-pond fraction. Nature Climate Change, 4:353–357, 2014. doi: 10.1038/nclimate2203.

J. Sedlar, M. Tjernström, M. Mauritsen, M. D. Shupe, I. M. Brooks, P. O. G. Persson, C. E. Birch, C. Leck, A. Sirevaag, and M. Nicolaus. A transitioning Arctic surface energy budget: The impacts of solar zenith angle, surface albedo and cloud radiative forcing. Climate Dyn., 37:1643–1660, 2011. doi: 10.1007/s00382-010-0937-5.

M. C. Serreze and R. G. Barry. Processes and impacts of Arctic amplification: A research synthesis. Global and Planetary Change, 77:85–96, 2011. doi: 10.1016/j.gloplacha.2011.03.004.

M. C. Serreze and R. G. Barry. The Arctic climate system. University Press, Cambridge, 2nd edition, 2014.

M. C. Serreze, J. E. Walsh, F. S.Chapin III, T. Osterkamp, M. Dyurgerov, V. Romanovsky, W. C. Oechel, J. Morison, T. Zhang, and R.G. Barry. Observational evidence of recent change in the northern high-latitude environment. Climatic Change, 46:159–207, 2000. doi: 10.1023/A:1005504031923.

C. A. Shuman, D. K. Hall, N. E. DiGirolamo, T. K. Mefford, and M. J. Schnaubelt. A dozen years of temperature observations at the Summit: Central Greenland automatic weather stations 1987-99. J. Appl. Meteor., 40:741–752, 2001.

C. A. Shuman, D. K. Hall, N. E. DiGirolamo, T. K. Mefford, and M. J. Schnaubelt. Comparison of near-surface air temperatures and MODIS ice-surface temperatures at Summit, Greenland (2008-13). J. Appl. Meteor. Climatol., 53:2172–2180, 2014. doi: 10.1175/JAMC-D-14-0023.1.

M. D. Shupe and J. M. Intrieri. Cloud radiative forcing of the Arctic surface: The influence of cloud properties, surface albedo, and solar zenith angle. J. Climate, 17:616–628, 2004.

M. D. Shupe, J. S. Daniel, G. de Boer, E. W. Eloranta, P. Kollias, C. N. Long, E. P. Luke, D. D. Turner, and J. Verlinde. A focus on mixed-phase clouds. Bull. Amer. Meteor. Soc., 89:1549–1562, 2008.

M. D. Shupe, V. P. Walden, E. Eloranta, T. Uttal, J. R. Campbell, S. M. Starkweather, and M. Shiobara. Clouds at Arctic atmospheric observatories. Part I: Occurrence and macrophysical properties. J. Appl. Meteor. Climatol., 50:626–644, 2011. doi: 10.1175/2010JAMC2467.1.

M. D. Shupe, P. O. G. Persson, I. M. Brooks, M. Tjernström, J. Sedlar, T. Mauritsen, S. Sjogren, and C. Leck. Cloud and boundary layer interactions over the Arctic sea ice in late summer. Atmos. Chem. Phys., 13:9379–9400, 2013a. doi: 10.5194/acp-13-9379-2013.

M. D. Shupe, D. D. Turner, V. P. Walden, R. Bennartz, M. P. Cadeddu, B. Castellani, C. J. Cox, D. R. Hudak, M. S. Kulie, N. B. Miller, R. R. Neely III, W. D. Neff, and P. M. Rowe. High and dry: New observations of tropospheric and cloud properties above the Greenland ice sheet. Bull. Amer. Meteor. Soc., 94(C10):169–186, 2013b. doi: 10.1175/BAMS-D-11-00249.1.

L. C. Smith, W. Chu V, K. Yang, C. J. Gleason, L. H. Pitcher, A. K. Rennermalm, C. J. Legleiter, A. E. Behar, B. T. Overstreet, S. E. Moustafa, Marco Tedesco, Richard R. Forster, A. L. LeWinter, D. C. Finnegan, Y. Sheng, and J. Balogh. Efficient meltwater drainage through supraglacial streams and rivers on the southwest Greenland ice sheet. PNAS, 112(4):1001–1006, 2014.

A. Solomon, M. D. Shupe, and N. B. Miller. Cloud-atmospheric boundary layer-surface interactions on the Greenland ice sheet during the July 2012 extreme melt event. J. Climate, 2017. doi: 10.1175/JCLI-D-16-0071.1.

K. Stamnes, R. G. Ellingson, J. A. Curry, J. E. Walsh, and B. D. Zak. Review of science issues, deployment strategy, and status for the ARM North Slope of Alaska–Adjacent Arctic Ocean climate research site. J. Climate, 12:46–63, 1999. doi: 10.1175/1520-0442-12.1.46.

K. Steffen and J. Box. Surface climatology of the Greenland ice sheet: Greenland climate network 1995-1999. J. Geophys. Res., 106(D24):33951–33964, 2001.

K. Steffen and T. DeMaria. Surface energy fluxes of Arctic winter sea ice in Barrow Strait. J. Appl. Meteor., 35:2067–2079, 1996.

H. A. M. Sterk, G. J. Steeneveld, and A. A. M. Holtslag. The role of snow-surface coupling, radiation, and turbulent mixing in modeling a stable boundary layer over Arctic sea ice. J. Geophys. Res. Atmos., 118:1199–1217, 2013. doi: 10.1002/jgrd.50158.

C. J. Stubenrauch, W. B. Rossow, S. Kinne, S. Ackerman, G. Cesana, H. Chepfer, L. Di Girolamo, B. Getzewich, A. Guignard, A. Heidinger, B. C. Maddux, W. P. Menzel, P. Minnis, C. Pearl, S. Platnick, C. Poulsen, J. Riedi, S. Sun-mack, A. Walther, D. Winker, S. Zeng, and G. Zhao. Assessment of global cloud datasets from satellites: Project and database initiated by the GEWEX radiation panel. Bull. Amer. Meteor. Soc., 94:1031–1049, 2013. doi: 10.1175/BAMS-D-12-00117.1.

M. Sturm, J. Holmgren, M. König, and K. Morris. The thermal conductivity of seasonal snow. J. Glaciology, 43:26–41, 1997.

W. Su, E. Dutton, T. P. Charlock, and W. Wiscombe. Performance of commercial radiometers in very low temperature and pressure environments typical of polar regions and of the stratosphere: A laboratory study. J. Atmos. Oceanic Technol., 25:558–569, 2008. doi: 10.1175/2007JTECHA1005.1.

H. U. Sverdrup. Scientific work of the Maud Expedition, 1922-1925. The Scientific Monthly, 22(5): 400–410, 1926.

M. Tedesco and X. Fettweis. 21st century projections of surface mass balance changes for major drainage systems of the Greenland ice sheet. Environ. Res. Lett., 7(4):1–11, 2012. doi: 10.1088/1748-9326/7/4/045405.

D. D. Turner and E. J. Mlawer. The radiative heating in underexplored bands campaigns. Bull. Amer. Meteor. Soc., 91:911–923, 2010.

D. D. Turner, B. M. Lesht, S. A. Clough, J. C. Liljegren, H. E. Revercomb, and D. C. Tobin. Dry bias and variability in Vaisala RS80-H radiosondes: The ARM experience. J. Atmos. Oceanic Technol., 20:117–132, 2003.

D. D. Turner, S. A. Clough, J. C. Liljegren, E. E. Clothiaux, K. E. Cady-Pereira, and K. L. Gaustad. Retrieving liquid water path and precipitable water vapor from the atmospheric radiation measurement (ARM) microwave radiometers. IEEE Trans. Geosci. Remote Sens., 45(11):3680–3690, 2007a.

D. D. Turner, A. M. Vogelmann, R. T. Austin, J. C. Barnard, K. Cady-Pereira, J. C. Chiu, S. A. Clough C. Flynn, M. M. Khaiye, J. Liljegren, K. Johnson, B. Lin, C. Long, A. Marshak, S. Y. Matrosov, S. A. McFarlane, M. Miller, Q. Min, P. Minnis, W. O'Hirok, Z. Wang, and W. Wiscombe. Thin liquid water clouds - Their importance and our challenge. Bull. Amer. Meteor. Soc., 88(2):177–190, 2007b. doi: 10.1175/BAMS-88-2-177.

D. D. Turner, S. Kneifel, and M. P. Cadeddu. An improved liquid water absorption model at microwave frequencies for supercooled liquid water clouds. J. Atmos. Oceanic Technol., 33: 33–44, 2016. doi: 10.1175/JTECH-D-15-0074.1.

T. Uttal, J. A. Curry, and Coauthors. Surface heat budget of the arctic ocean. Bull. Amer. Meteor. Soc., 83:255–275, 2002. doi: 10.1175/1520-0477(2002)083⟨0255:SHBOTA⟩2.3.CO;2.

R. S. W. van de Wal and J. Oerlemans. An energy balance model for the Greenland ice sheet. Global and Planetary Change, 9:115–131, 1994.

R. S. W. van de Wal, W. Greuell, M. R. van den Broeke, C. H. Reijmer, and J. Oerlemans. Surface mass-balance observations and automatic weather station data along a transect near Kangerlussuaq, west Greenland. Annals of Glaciology, 42:311–316, 2005.

M. van den Broeke, D. van As, C. Reijmer, and R. van de Wal. Assessing and improving the quality of unattended radiation observations in Antarctica. J. Atmos. Oceanic Technol., 21:1417–1431, 2004.

M. van den Broeke, P. Smeets, J. Ettema, and P. Kuipers Munneke. Surface radiation balance in the ablation zone of the west Greenland ice sheet. J. Geophys. Res., 113:1–14, 2008. doi: 10.1029/2007JD009283.

M. van den Broeke, J. Bamber, J. Ettema, E. Rignot, E. Schrama, W. J. van de Berg, E. van Meijgaard, I. Velicogna, and B. Wouters. Partitioning recent Greenland mass loss. Science, 326: 984–986, 2009.

M. R. van den Broeke, C. J. P. P. Smeets, and R. S. W. van de Wal. The seasonal cycle and interannual variability of surface energy balance and melt in the ablation zone of the west Greenland ice sheet. The Cryosphere, 5:377–390, 2011. doi: 10.5194/tc-5-377-2011.

K. Van Tricht, S. Lhermitte, J.T.M. Lenaerts, I.V. Gorodetskaya, T.S. L'Ecuyer, B. Noël, M.R. van den Broeke, D.D. Turner, and N.P.M. van Lipzig. Clouds enhance Greenland ice sheet meltwater runoff. Nat. Commun., 7(10266):1–9, 2016. doi: 10.1038/ncomms10266.

M. Vizcaíno, W. H. Lipscomb, W. J. Sacks, and M. van den Broeke. Greenland surface mass balance as simulated by the Community Earth System Model. Part II: Twenty-first-century changes. J. Climate, 27:215–226, 2014. doi: 10.1175/JCLI-D-12-00588.1.

L. Vuilleumier, M. Hauser, C. Félix, F. Vignola, P. Blanc, A. Kazantzidis, and B. Calpini. Accuracy of ground surface broadband shortwave radiation monitoring. J. Geophys. Res. Atmos., 119(24): 13838–13860, 2014. doi: 10.1002/2014JD022335.

J. E. Walsh and W. L. Chapman. Arctic cloud radiation temperature associations in observational data and atmospheric reanalyses. J. Climate, 11:3030–3045, 1998.

S. G. Warren. Optical properties of snow. Rev. Geophys. and Space Phys., 20(1):67–89, 1982.

P. Wright, M. Bergin, J. Dibb, B. Lefer, F. Domine, T. Carman, C. Carmagnola, M. Dumont, Z. Courville, C. Schaaf, and Z. Wang. Comparing MODIS daily snow albedo to spectral albedo field measurements in Central Greenland. Remote Sensing of Environment, 140:118–129, 2014. doi: 10.1016/j.rse.2013.08.044.

Y. Zhang, D. J. Seidel, J. Golaz, C. Deser, and R. A. Tomas. Climatological characteristics of Arctic and Antarctic surface-based inversions. J. Climate, 24:5167–5186, 2011.

H. J. Zwally, W. Abdalati, T. Herring, K. Larson, J. Saba, and K. Steffen. Surface melt-induced acceleration of Greenland ice-sheet flow. Science, 297:218–222, 2002.